Mid-IR SiGe photonics circuit for sensing application

Natnicha Koompai

THESE DE DOCTORAT

NNT 2024UPAST027

Mid-IR SiGe photonics circuit for sensing application

Circuits intégrés photoniques SiGe pour des applications capteurs dans l'infrarouge moyen

Thèse de doctorat de l'université Paris-Saclay

École doctorale n°575 : electrical, optical, bio : physics and engineering (EOBE)
Spécialité de doctorat : Electronique, Photonique et Micro-Nanotechnologies
Graduate School : Sciences de l'ingénierie et des systèmes. Référent : Faculté des sciences d'Orsay

Thèse préparée dans l'unité de recherche **Centre de Nanosciences et de Nanotechnologies** (université Paris-Saclay, CNRS), sous la direction de **Delphine MARRIS-MORINI**, Professeur, et le co-encadrement d'**Adel BOUSSEKSOU**, Maître de conférences

Thèse soutenue à Paris-Saclay, le 15 Mars 2024, par

Natnicha KOOMPAI

Composition du Jury

Membres du jury avec voix délibérative

Jean-Emmanuel BROQUIN Professeur, Grenoble INP-UGA	Président
Christophe COUTEAU Professeur, Université Technologique de Troyes	Rapporteur & Examinateur
Joel CHARRIER Professeur, Université de Rennes	Rapporteur & Examinateur
Jean-Baptiste RODRIGUEZ Chargé de recherche, Université de Montpellier	Examinateur

université PARIS-SACLAY

DOCTORAL SCHOOL
Electrical, Optical, Bio: Physics and Engineering (EOBE)

Titre : Circuits intégrés photoniques SiGe pour des applications capteurs dans l'infrarouge moyen

Mots clés : Photonique silicium, Circuits intégrés photoniques, Moyen-infrarouge, SiGe

Résumé : Le développement de circuits intégrés photoniques fonctionnant dans le moyen infrarouge voit un développement considérable en raison de leurs applications pour l'identification de substances chimiques et biologiques. Les systèmes actuels commerciaux fonctionnant dans le moyen infrarouge reposent sur des équipements volumineux et coûteux. Beaucoup de travaux sont consacrés à la réduction de la taille de ces systèmes à des dimensions de l'ordre de celles d'un circuit intégré. L'utilisation de la photonique sur silicium pour la réalisation de circuits intégrés dans le moyen infrarouge offre de grands avantages en termes de compacité, de hautes performances et de coût.

Un point clé pour le développement d'une application réelle est de pouvoir coupler la source de lumière infrarouge moyen avec les circuits photoniques de manière compacte. Dans ce contexte, l'objectif principal de cette thèse s'est concentré sur deux défis différents : (i) progrès vers l'intégration de QCL avec des circuits photoniques SiGe (ii) contribution au développement de dispositifs photoniques SiGe par le développement de résonateurs à fort facteur de qualité, fonctionnant autour d'une longueur d'onde de 8 µm. Ces travaux ont ouvert la voie au développement futur de circuits photoniques intégrés sur puce dans le moyen infrarouge.

Title : Mid-IR SiGe photonics circuit for sensing application

Keywords : Si photonics, Integrated Photonics Circuits, Mid-infrared, SiGe

Abstract : There is currently a growing interest in the development of mid-infrared photonics integrated circuits driven by their unique features and potential to identify chemical and biological substances. Commercially available mid-infrared systems currently rely on bulky and expensive equipment. Substantial efforts are devoted to downsizing mid-infrared systems to chip-scale dimensions. The use of silicon photonics for the demonstration of mid-IR integrated circuits offers great advantages in terms of compactness, high performance, and cost-effective sensing systems.

A key point for development of real application is to be able to couple the mid-infrared light source with the photonics circuits in a compact way. In this context, the main objective of this thesis has been focused on two different challenges: (i) progress towards the integration of QCL with SiGe photonics circuits in the mid-IR range (ii) contribution to the development of SiGe photonics devices by the development of high-quality factor resonators operating around 8 µm wavelength. This work has opened the route for future development of on-chip integrated photonics circuit in the mid-IR.

ACKNOWLEDGMENTS

This PhD journey is not only a result of diligent work and research but also, equally important, the invaluable support from many people. With the following words, I would like to thank each and every one of you, my supervisor and co-supervisor, my colleagues, friends, and family for your help, advice, and patience.

First and foremost, I extend my deepest gratitude to my supervisor, Delphine Marris-Morini, whose consistent support, guidance, and encouragement have been the foundation of this research. Her mentorship and insightful feedback have been invaluable in shaping the trajectory of this work. Throughout my Ph.D. thesis, Delphine has given me personal support; she is always being very kind. Thank you for her understanding, especially during the period I had a difficult time. I can only say thank you, Delphine, for giving me the chance to work on this thesis with you. This period has been a wonderful time of my life.

I would also like to express my deepest gratitude to my co-supervisor, Adel Bousseksou, for all his guidance and support. Thank you for all the valuable help, especially in the mid-infrared DFB setups and the butt-coupling experiments. I deeply appreciate the insightful advice and remarkable scientific guidance he has provided to me throughout this journey.

My grateful thanks are also extended to Laurent Vivien, Eric Cassan, Carlos Alonso Ramos, and Daniele Melati for their comments, supervision, and useful critiques of this research work. Additionally, I extend my appreciation to the nanotechnology specialists who have significantly contributed to my work in the cleanroom for device fabrication. Although Xavier Le Roux is no longer with us, I am deeply grateful for his guidance, alongside Laurence Ferlazzo, Jean-Rene Coudevylle, David Bouville, Etienne Herth, and Samson Edmond, who have generously shared their expertise and provided invaluable advice throughout the process.

In addition, I would like to thank Prof. Christophe Couteau, Prof. Joel Charrier, Prof. Jean-Emmanuel Broquin, and Dr. Jean-Baptiste Rodriguez for reviewing my thesis and being members of my thesis committee. I enjoyed and appreciated all of your helpful discussions, knowledge, and suggestions.

I am deeply grateful to Papichaya Chaisakul, my supervisor during my master's degree in Thailand. Beyond being my mentor, you have been a cherished friend. Your invaluable advice has greatly influenced my academic journey. Thank you, Aj.Pop, for your unwavering support; I owe much of my success to you.

I wish to extend my heartfelt gratitude to all Ph.D. students and Postdoctorals within the MINAPHOT group. I extend my deepest thanks to Miguel Montesinos Ballesteros, who served as my first mentor. Your patience, enthusiasm, and guidance on cleanroom fabrication and experimental setup have been invaluable to me. I am genuinely delighted and deeply appreciative to share the office with Thi Hao Nhi Nguyen and Victor Turpard. Our time together has been truly memorable, and I am thankful for the scientific and personal support you have provided throughout my Ph.D. My gratitude also extends to Lucas Deniel, Annabelle Bricout, Hamza Dely, Jonathan Peltier, Yijun Yang, Zijun Xiao, David Medina, Mikhaïl Dyatlov, David Gonzalez-Andrade, Zindine Mokeddem, Warren Kut-king-kan, and many others. Together, we have shared invaluable learning experiences, moments of joy, and unforgettable memories. With such enthusiastic and humorous companions, my time at C2N has been truly enriching. I consider myself fortunate to be a member of this MINIAPHOT group. I extend my gratitude to Luca Lucia, a Ph.D. student under my co-supervisor, for his invaluable assistance during the measurement sessions and for the support and insightful discussions we shared together. I am also very grateful to my nice colleagues from L-NESS from Politecnico de Milano and IES lab from Université de Montpellier for the successful collaboration we have together.

I also want to thank all my friends, with special appreciation for Kanokon Upitak, my lifelong friend from Thailand. Throughout our journey, we have shared countless memories, both joyful and challenging. Today, I am proud to say that I have achieved my goals, and I owe a debt of gratitude to you for always standing by my side. I also want to express my thanks to Pawaphat Jaturaphagorn, whose insightful discussions and encouragement have been invaluable. And to Nessrine Jebari and Sarra Riahi, your constant support and uplifting presence will always be in my heart. I am deeply grateful for Amin Hamdi, who is not just my boyfriend but also my partner and the source of my moral support. Your endless kindness and support you have extended to me have been truly remarkable and unforgettable.

Finally, I would like to express my gratitude to my parents and my family for their unwavering love and support. Their belief in me has been my greatest strength. Thank you for everything.

Palaiseau, France

March 2024

Natnicha Koompai

SYNTHESE EN FRANÇAIS

Le développement de circuits intégrés photoniques fonctionnant dans le moyen infrarouge (MIR) voit un développement considérable en raison de leurs applications pour l'identification de substances chimiques et biologiques. Cependant, les systèmes optiques moyen infrarouge disponibles dans le commerce reposent sur des équipements encombrants et coûteux. Beaucoup de travaux portent désormais sur la réduction de la taille et à l'intégration des circuits photoniques. Les circuits intégrés photoniques sur silicium ont connu un développement remarquable. L'utilisation de la technologie du silicium pour les circuits intégrés photoniques dans la gamme du MIR ouvre de nouvelles opportunités pour permettre la création de systèmes de détection compacts, à hautes performances et faible coût. Parmi les matériaux utilisés dans les circuits intégrés photoniques sur silicium, le germanium (Ge) représente un bon candidat pour la détection spectroscopique à large bande dans la région MIR en raison de sa grande fenêtre de transparence (jusqu'à 15 µm de longueur d'onde) et de sa forte non-linéarité du troisième ordre. Il a été montré précédemment que les guides Silicium Germanium (SiGe) à gradient d'indice offrent de bonnes performances pour le développement de circuits intégrés photoniques fonctionnant dans une large bande spectrale. Les travaux présentés ici dans cette thèse s'appuieront sur la plateforme SiGe à gradient d'indice.

Actuellement, un point clé pour le développement d'applications réelles basées sur les circuits photoniques dans le MIR est le couplage des circuits photoniques avec une source de lumière dans l'infrarouge moyen de manière compacte. En effet, l'intégration monolithique d'un laser à cascade quantique (QCL) à base de matériaux InAs/AlSb sur des circuits photoniques SiGe est actuellement étudiée dans le cadre du projet ANR Light UP. Un couplage contra directionnel assisté par réseau a été prévu pour coupler la lumière entre le laser et le guide d'onde SiGe. Tout au long de ma thèse, j'ai ainsi poursuivi deux objectifs principaux : (i) progresser vers l'intégration du QCL avec les circuits photoniques SiGe dans le MIR (ii) contribuer au développement de dispositifs photoniques SiGe par le développement de résonateurs à fort facteur de qualité, fonctionnant autour de 8 µm de longueur d'onde.

Développements vers une source QCL intégrée de manière monolithique sur circuit photonique SiGe

Dans le cadre du projet ANR Light UP project, l'intégration monolithique de QCL InAs/AlSb

est étudiée. De faibles pertes optiques et un gain optique important avec de bonnes performances du dispositif doivent être préservés après la combinaison des dispositifs actifs et passifs. La conception conjointe des couches épitaxiées formant le guide SiGe à gradient d'indice et l'empilement du laser III-V est visible sur la figure 1 (a.), ainsi que les empilements de matériaux utilisés dans la croissance épitaxiale sur la figure 1 (b.). Afin de développer directement les dispositifs QCL sur le circuit photonique SiGe, deux points principaux doivent être testés : (i) les contacts électriques et (ii) la réalisation de la cavité optique, plus précisément, le coupleur entre le matériau à grain III- V et le guide d'onde passif SiGe.

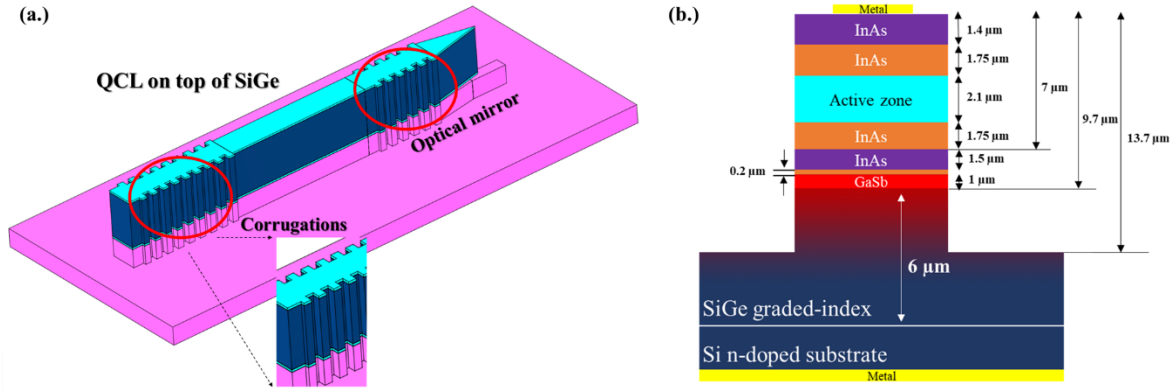

Fig.1. (a.) Vue schématique du dispositif final illustrant le QCL (couleur bleue) au-dessus de la plateforme SiGe (couleur rose) avec 2 miroirs optiques constitués de corrugations latérales des guides d'onde (b.) Vue en coupe de la structure avec le QCL épitaxié sur le guide d'onde SiGe

En raison de la complexité du processus de fabrication pour réaliser les dispositifs finaux, le contact électrique est ensuite étudié via le contact arrière en tant que contact inférieur du QCL. En ce sens, il est important de vérifier à la fois les propriétés optiques et les propriétés électriques du matériau SiGe.

Premièrement, les propriétés optiques d'une couche de SiGe légèrement dopée de 6 µm sur un substrat de Si hautement dopé ont été étudiées. J'ai d'abord fabriqué des guides d'ondes en spirale avec différentes longueurs de propagation. En utilisant la méthode cut-back, de faibles pertes optiques ont pu être mesurées, pour les polarisations TE et TM, de 5 à 8 µm de longueur d'onde, comme le montre la figure 2. Cette mesure confirme que cette plateforme est compatible avec l'intégration du QCL en polarisation TM.

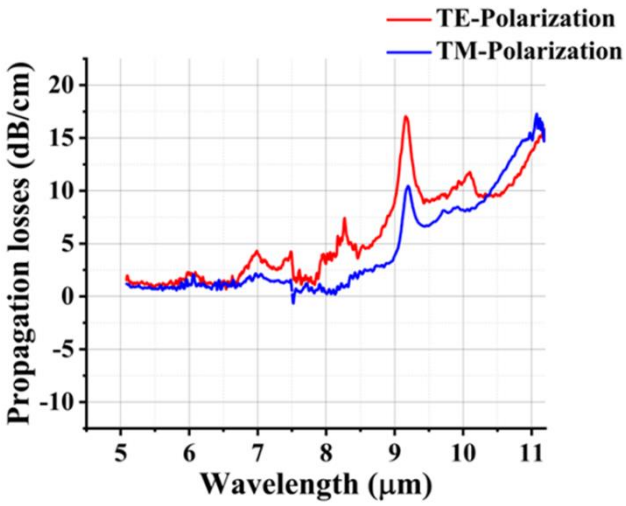

Fig.2. Pertes de propagation mesurées expérimentalement de 5,1 à 11,2 μm sur la plateforme SiGe pour les polarisations TE et TM.

Ensuite, des diodes mesa carrées ont été fabriquées. La caractéristique I-V en polarisation directe a été mesurée expérimentalement. La dérivée de la tension par rapport au courant injecté a été calculée pour estimer la résistance, comme le montre la Fig.3. J'ai obtenu une résistance d'environ 3 Ω à partir de la mesure IV. De plus, le comportement Schottky du contact a été découvert, avec une barrière Schottky de 0,58 eV. Ces résultats ouvrent la voie aux premiers modulateurs intégrés qui ont ensuite été démontrés dans le groupe.

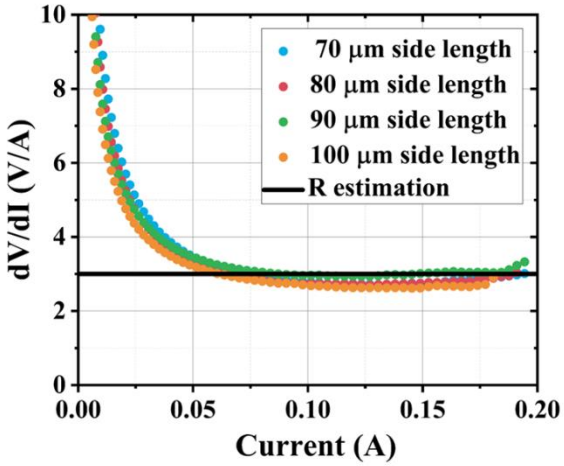

Fig.3. Mesure de la dérivée de la tension par rapport à l'intensité du courant dans différentes diodes. Une ligne horizontale indique une résistance de 3 Ω.

Ensuite, le processus de gravure du matériau III-V a été examiné. Le test initial visait à affiner les paramètres du masque et de la lithographie, en utilisant du matériau massif InAs. Des techniques standard de salle blanche ont été utilisées, notamment le nettoyage au solvant, le dépôt de résine, la lithographie par faisceau électronique, le développement et la gravure sèche (gravure ICP). Le dépôt ALD a été utilisé pour créer une couche de SiO_2 d'environ 5 nm afin d'améliorer l'adhésion entre le masque et le matériau. La résine HSQ a été utilisée. Sur la figure 4 on peut voir le profil d'InAs après la gravure initiale. On peut observer que l'isotropie et la rugosité de la surface devraient être améliorées après le premier test.

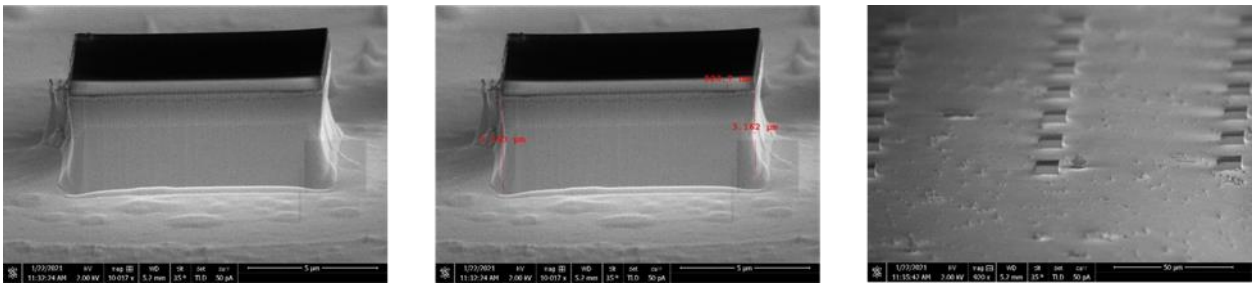

Fig.4. Vue au microscope électronique de couches d'InAs après gravure ICP-etching (HBr et O_2).

Les tests se sont poursuivis en utilisant des échantillons QCL avec le même processus optimisé sur la base des tests antérieurs avec InAs. Initialement, le QCL a été traité sans la couche ALD pour simplifier le processus de fabrication. Après la gravure ICP, trois défis clés sont apparus : l'adhésion de la résine, la révélation de plans de gravure et des erreurs d'alignement de lithographie. Pour répondre au problème d'adhésion de la résine, le dépôt d'ALD a été réintroduit pour améliorer l'adhésion. Pour les erreurs de lithographie, les efforts se sont concentrés sur la modification des paramètres lors de la lithographie par faisceau électronique. Cependant, il a été observé que cette erreur n'affectait pas le profil du guide d'onde après le processus de gravure. Cette question est donc actuellement considérée comme une préoccupation secondaire. La principale préoccupation est maintenant la révélation de plans cristallographiques qui se produit pendant le processus de gravure, comme illustré sur la figure 5.

Cependant, le processus de croissance des QCL sur SiGe graduel, géré par nos partenaires de l'Université de Montpellier et de Politecnico Di Milano, s'est avéré plus difficile que prévu. Cet aspect du projet a donc été suspendu pour le moment.

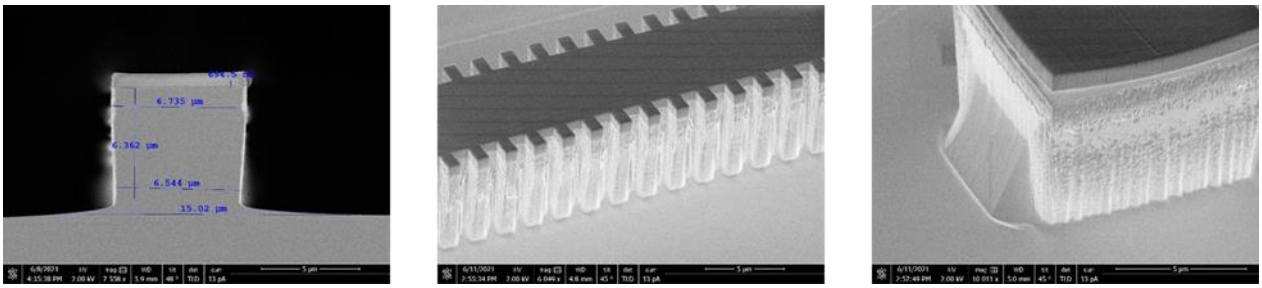

Fig.5. L'observation du QCL sous microscope électronique à balayage montre les images de profil du guide d'ondes vertical ainsi que la révélation de plans dans une direction cristallographique.

Couplage bout à bout d'un laser à cascade quantique (QCL) et d'un guide d'onde SiGe sur deux circuits photoniques distincts

En raison des difficultés rencontrées lors de la croissance directe des lasers à cascade quantique (QCL) sur substrat SiGe, une autre approche a été proposée, visant à explorer le couplage de lumière entre deux circuits photoniques distincts. Il a ainsi été démontré que cette méthode est une solution pour le couplage compact de circuits photoniques QCL vers SiGe. Pour démontrer expérimentalement l'avantage de cette approche, j'ai construit et réalisé une expérience pour le couplage bout à bout. Le couplage direct entre un QCL fonctionnant à 7.4 µm de longueur d'onde et un guide SiGe a été réalisé avec succès, comme le montre la figure 6. La distance entre le QCL et le SiGe a été estimée autour de 12 µm.

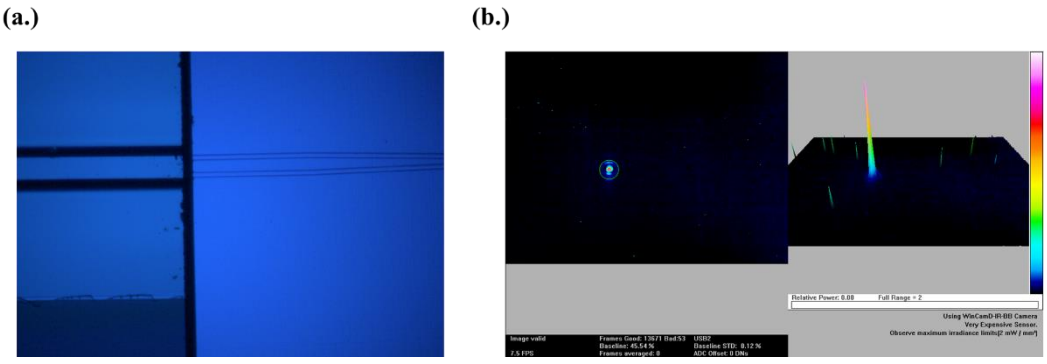

Fig.6. (a.) L'image vue de dessus du microscope optique montre l'alignement d'un composant actif (QCL) et de la puce passive (SiGe). (b.) Observation du faisceau optique en sortie du guide SiGe après le couplage bout à bout.

De plus, j'ai évalué les pertes de couplage de la puce QCL vers le guide SiGe. J'ai mesuré expérimentalement la puissance à la sortie du laser et à la sortie du circuit photonique SiGe, comme le montre la Fig.7. Après calcul, j'ai rapporté dans ce manuscrit une valeur des pertes de couplage de la puce QCL vers SiGe d'environ 10 dB en considérant des pertes de propagation du guide d'onde de 1,5 dB/cm, et des pertes due à la facette de sortie du circuit photonique SiGe de 5 dB. Cette première démonstration de couplage bout à bout ouvre la voie à de futures avancées dans les circuits photoniques intégrés MIR utilisant des systèmes compacts.

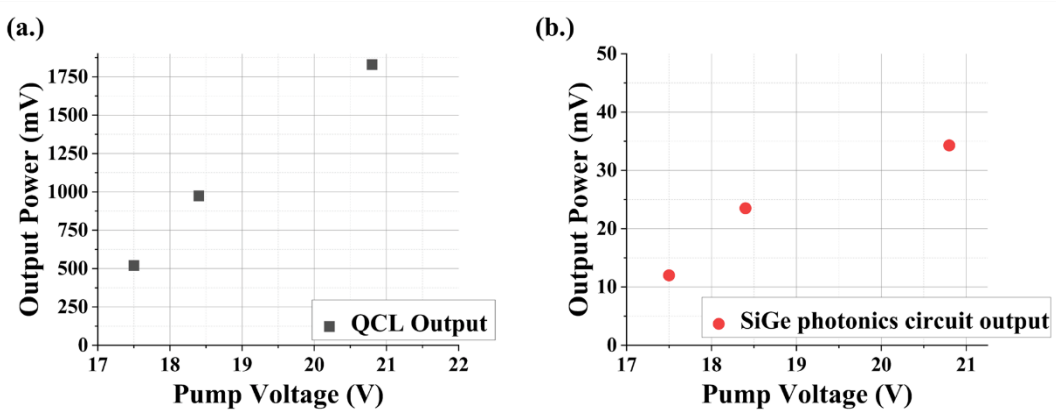

Fig.7. Puissance de sortie en fonction de la tension appliquée sur le QCLL pour différentes configurations : (a.) mesurée en sortie du QCL et (b.) en sortie du circuit photonique SiGe.

Résonateurs optiques à large bande passante dans le LWIR

Outre la démonstration de l'intégration entre la source photonique MIR et les circuits photoniques SiGe, j'ai également été impliqué dans le développement des éléments de base passifs de la plateforme photonique MIR. Cette section présentera les travaux effectués pour le développement de résonateurs intégrés à haut facteur de qualité (facteur Q) dans la gamme de l'infrarouge LWIR (Long Wave Infra Red) basés sur la plate-forme SiGe à gradient d'indice. À cet égard, diverses configurations ont été fabriquées et testées. Les premiers travaux ont été réalisés en utilisant un échantillon de résonateurs préexistant. Les spectres de transmission quasi-TM normalisés des résonateurs à partir des lasers QCL fonctionnant en continu et pulsés sont présentés sur la figure 8. Un facteur Q d'environ 3 700 est obtenu à une longueur d'onde d'environ 8 µm pour tous les résonateurs. Cette première expérience a permis de mettre en évidence les limitations provenant de chacun des lasers utilisés pour la caractérisation des résonateurs.

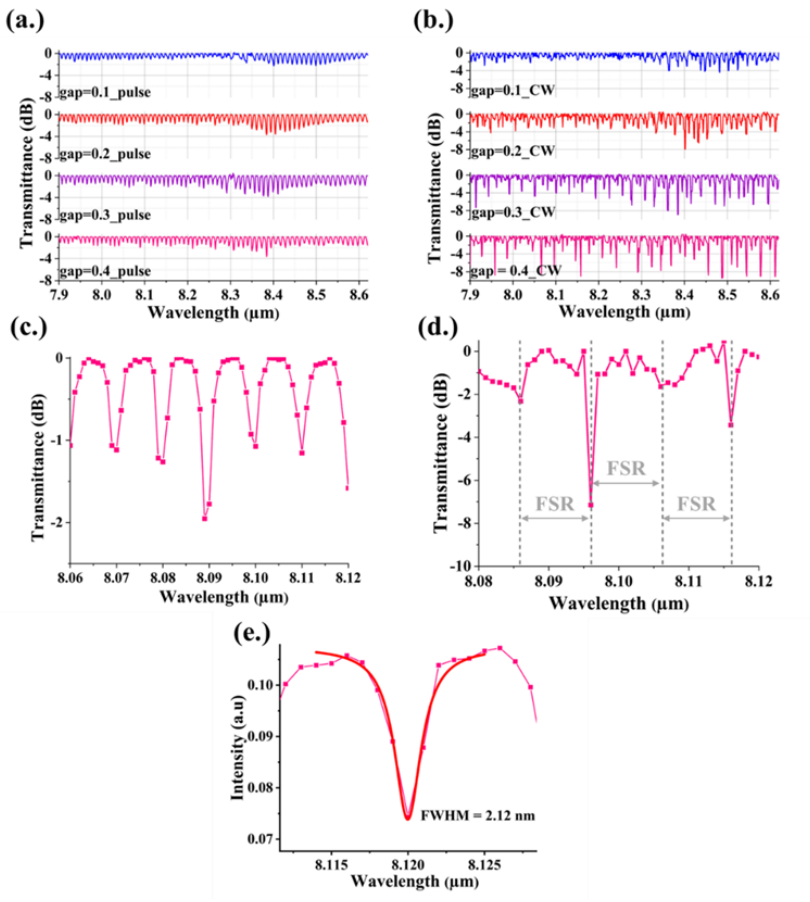

Fig.8. Mesure des spectres de transmission des résonateurs en polarisation TM lorsque le rayon est de 250 µm, la longueur de couplage de 60 µm avec différentes valeurs de la distance entre le guide et le résonateur, avec (a.) un laser QCL en régime pulsé ; (b.) un QCL fonctionnant en continu. La comparaison des vues zoomées montre la limitation venant de chaque laser : (c.) en régime pulsé ; (d.) en régime continu. (e.) Zoom sur un pic de résonance unique mesuré avec le QCL en régime pulsé, la ligne rouge continue représente l'ajustement lorentzien pour extraire le FWHM. Un facteur Q de 3700 a été obtenu.

Ensuite, l'échantillon a été testé avec un laser DFB-QCL qui permet d'ajuster la longueur d'onde émise en ajustant la température (ou le courant) du laser. Grâce à une fine résolution lors de l'expérience, la résonance Fabry-Pérot provenant de la facette a été observée pour la première fois. Sur la base de cette configuration expérimentale, un facteur Q de 5 900 à une longueur d'onde de 8,5 µm a été extrait, ce qui vérifie que les résultats initiaux étaient limités par les lasers utilisés. Cependant, cette configuration empêche la mesure dans une large gamme spectrale.

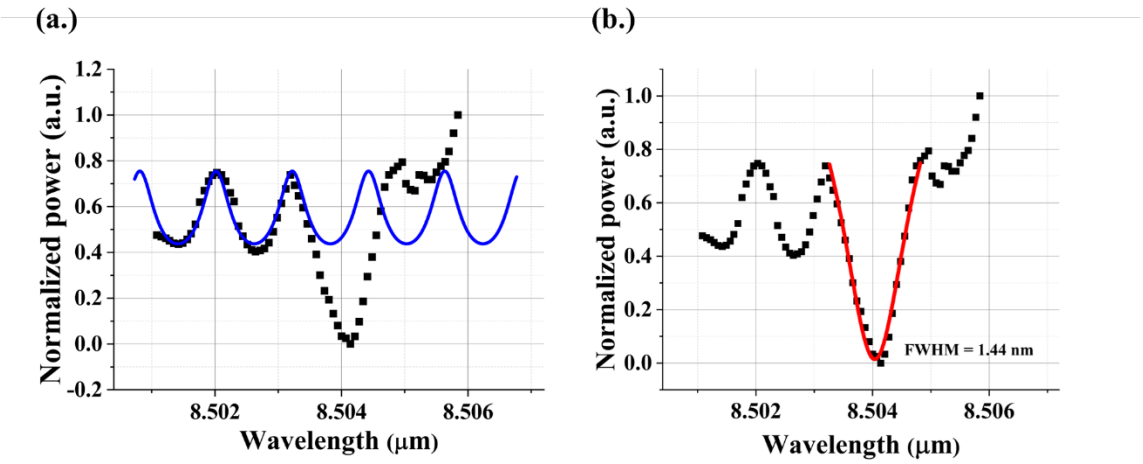

Fig.9. (a.) Spectres de transmission expérimentaux du résonateur en polarisation TM en utilisant le laser DFB. La courbe bleue indique le modèle Fabry-Pérot simulé. (b.) Vue agrandie d'une seule résonance du graphique de gauche, montrant l'ajustement lorentzien avec la courbe rouge.

Enfin, j'ai développé une nouvelle conception pour le résonateur en implémentant un chauffage thermique dans le résonateur pour surmonter les limitations obtenues lors des mesures avec les lasers à large bande spectrale. En ce sens, je pourrai contrôler la température par injection de courant, conduisant à contrôler la phase de la lumière se propageant dans le résonateur. Cette méthode permet un balayage précis des résonances, permettant ainsi des mesures à haute résolution, en utilisant un laser à longueur d'onde fixe. Dans un premier temps, la conception du résonateur et la mise en œuvre du chauffage ont été discutées. Ensuite, j'ai évalué expérimentalement la variation de phase à l'intérieur du résonateur. Les déplacements de résonance ($\Delta\lambda$) en fonction de la puissance électrique dissipée dans la chaufferette ont été mesurés, comme indiqué sur la figure 10. Un décalage de résonance de 17,5 nm/W peut être déduit de la pente de la courbe, comme le montre l'ajustement linéaire en couleur rouge. Cette valeur sera utilisée pour convertir la puissance électrique dissipée en décalage de longueur d'onde.

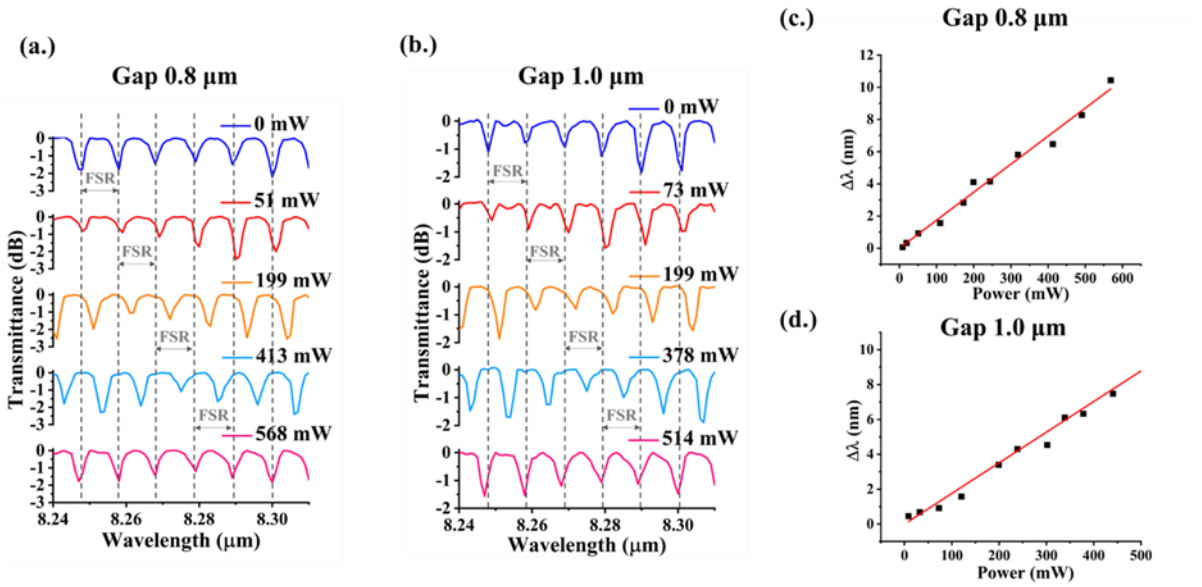

Fig.10. Spectres de transmission optique en fonction de la longueur d'onde lorsque différentes valeurs du courant sont appliquées sur le radiateur. Les mesures sont effectuées sur des résonateurs avec un rayon de 250 µm, une longueur de couplage de 45 µm et pour différentes valeurs de la distance entre le guide et le résonateur (a.) 0,8 µm et (b.) 1,0 µm ; les lignes grises précisent le FSR du résonateur. Les déplacements de résonance en fonction de la puissance dissipée sont rapportés en (c.) et (d.) pour des distances de 0,8 µm et 1,0 µm respectivement. La ligne rouge continue indique l'ajustement linéaire, qui est utilisé pour estimer les performances du chauffage thermique.

Grâce à la très bonne résolution permise par la variation de température dans le résonateur, les franges Fabry-Pérot provenant de la facette et les résonances du résonateur peuvent être observées à partir de la mesure. Comme illustré sur la figure 11, j'ai ainsi démontré un résonateur intégré fonctionnant sur une large bande spectrale dans le LWIR. Le facteur Q le plus élevé de $1{,}01 \times 10^5$ a été obtenu à une longueur d'onde de 7,45 µm, en utilisant un résonateur avec un rayon de 350 µm, une longueur de couplage de 10 µm et une distance résonateur-guide d'onde de 1 µm. La démonstration réussie de ce résonateur intégré représente une avancée notable dans la création de générateurs en peigne basés sur des microrésonateurs dans la gamme spectrale LWIR.

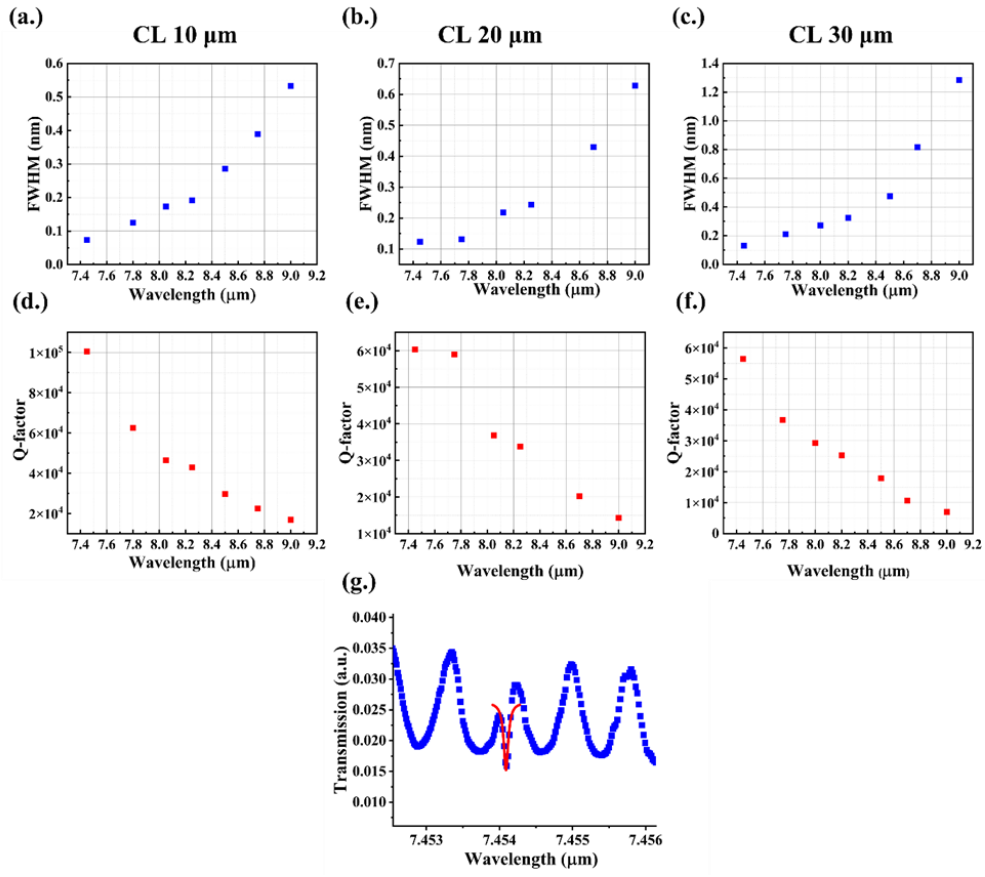

Fig.11. Largeur à mi-hauteur (FWHM) des résonances mesurées en fonction de la longueur d'onde pour un résonateur de rayon 350 µm et avec différentes longueurs de couplage (la distance guide-résonateur est fixée à 1 µm) : (a.) CL = 10 µm, (b.) CL = 20 µm, et (c.) CL = 30 µm, respectivement. Le facteur Q du résonateur, qui est calculé à partir de son FWHM pour (d.) CL = 10 µm, (e.) CL = 20 µm et (f.) CL = 30 µm, respectivement. (g.) Exemple de transmission d'un résonateur intégré avec un rayon de 350 µm, une longueur de couplage de 10 µm et une distance guide-résonateur de 1 µm en fonction de la longueur d'onde à λ = 7,45 µm, montrant le facteur Q le plus élevé de $1{,}01\times10^5$.

Conclusions

En conclusion, cette thèse a démontré avec succès le développement des briques de base pour la réalisation future d'une source QCL intégrée de manière monolithique au-dessus d'une plate-forme SiGe, le couplage bout à bout entre deux puces distinctes, et l'amélioration des performances des résonateurs intégrés tant qu'élément constitutif indispensable d'une plateforme d'optique intégrée. Par conséquent, ces travaux ouvrent des opportunités prometteuses pour des capteurs MIR entièrement intégrés basés sur la photonique Si.

TABLE OF CONTENTS

1 INTRODUCTION

Over the past two decades, there has been a growing interest in the mid-infrared (mid-IR) spectral range among scientists and researchers in photonics. This interest is driven by the unique features and potential of using mid-IR photonics in many sensing applications related to food safety, indoor air quality sensing, medical diagnosis, astronomy, and security. While commercial sensing systems are available, they mostly operate in a free-space configuration, leading to size and cost issues. The development of compact integrated photonics circuits in the mid-IR is thus expected to drive a revolution, making possible the development of compact sensing accessible in everyday life. To address this challenge, various integrated photonics platforms are currently under study, along with the whole set of building blocks that have been investigated in order to provide compact and widespread mid-IR devices. Silicon photonics integrated circuits have exhibited a truly remarkable development of mid-IR photonics by enabling high-volume fabrication technology. Significant progress work on silicon integration has been made over the past few years. Silicon photonic circuits have emerged as a compelling solution to address several technical challenges in photonic interconnects, data communication, telecommunication, specialized signal processing, switched networks, lab-on-a-chip, chemical, and biological sensing systems.

As a key point for the development of real applications in mid-IR photonic circuits, it is necessary to couple the photonics circuits with a mid-IR light source in a compact way. A SiGe photonics platform has been demonstrated with a promising performance for operating in the long-wave infrared range. Many building blocks based SiGe graded-index have been underdeveloped in our research group in collaboration with L-NESS, Politecnico di Milano, Italy. In addition, the monolithic integration of InAs/AlSb – based Quantum Cascade Laser (QCL) on SiGe photonics circuits is currently being investigated in the framework of the ANR Light UP project.

In this context, my Ph.D work was devoted to: (i) progress towards the integration of QCL with SiGe photonics circuits in the mid-IR range (ii) contributing to the development of SiGe photonics devices, by the development of high Q resonator operating around 8 µm wavelength. In the first section of this chapter, I will briefly introduce the mid-IR spectral range and its unique features that have motivated the development of applications in biological and

molecular sensing. In the second section, I will provide a state of the art of mid-IR integrated platform with active and passive devices. Then, the third section will describe the groundbreaking concept of integrated Si photonics with QCL-based III/V material, together with the design for the monolithic integration. In the end, the outline of this manuscript will be presented.

1.1 Motivation of Mid-Infrared Photonics Integration for Sensing Applications

The mid-infrared (mid-IR) region covers a wavelength range of approximately 2 to 20 μm. It can be separated into different subranges depending on the infrared radiation emitted by objects at a certain temperature. A commonly used sub-division scheme for mid-IR is: Short-wave infrared (SWIR) defined from 1.4 – 3 μm; Middle-wave infrared (MWIR) between 3 – 8 μm; and Long-wave infrared (LWIR) from 8 – 15 μm [1]. Typically, the MWIR and LWIR are more interesting in the sensing scheme due to their molecular absorption in this spectra range. In fact, this molecular vibrational signature can also be detected in the near-IR ($\lambda < 2$ μm). However, it is not caused by the fundamental vibration modes but by vibrational overtones. Therefore, the absorption coefficient in the mid-IR is significantly greater by several orders of magnitude than in the near-IR.

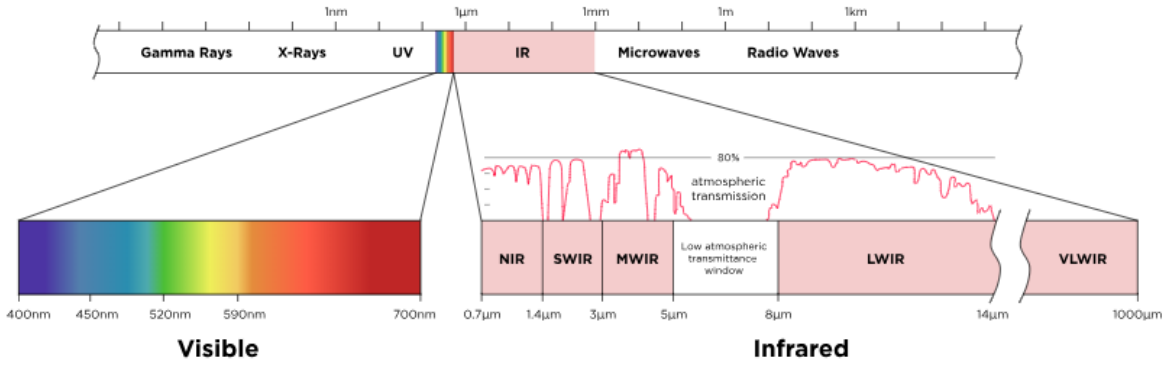

Fig.1.1. Electromagnetic spectrum showing the infrared wavelength intervals. Image adapted from [2].

As known, the mid-IR contains the most important spectral signatures of organic and inorganic gases [3] also called “the molecular fingerprint region”, spanning from 3 to 13 μm wavelength.

Each molecule has its fundamental vibrational and rotational resonance, which absorbs the light at a specific wavelength and produces unique absorption spectra [4], reported in Fig.1.2(a.). This molecular "fingerprinting" greatly impacts spectroscopy as it can identify a target molecule in a sample. In addition, the atmospheric transmission window (3 – 5 μm, and 8 – 12 μm wavelength) appears in this spectral range.

Therefore, there is increasing attention on mid-infrared integrated photonics in both industrial and academia thanks to the potential high-impact applications such as environmental monitoring [5-7], medical diagnostics for public health [8], and industrial production [9, 10]. As can be seen in Fig.1.2(b.), the mid-IR is highly relevant for sensing and monitoring applications in any context. For example, carbon monoxide (CO) has a strong absorption at 4.6 μm wavelength [11], so, it is possible to detect very low concentrations of CO in the environment as a pollution sensor. Recently, the James Web Space Telescope has taken advantages from the mid-IR spectral range [12] to create a camera and a spectrograph that sees light in the mid-infrared region in order to observe the redshifted light of distant galaxies, newly forming stars, and visible comets as well as the objects in the Kuiper Belt.

(a.)

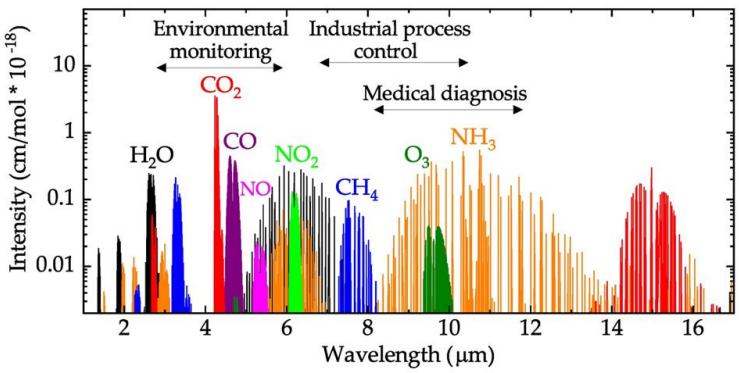

(b.)

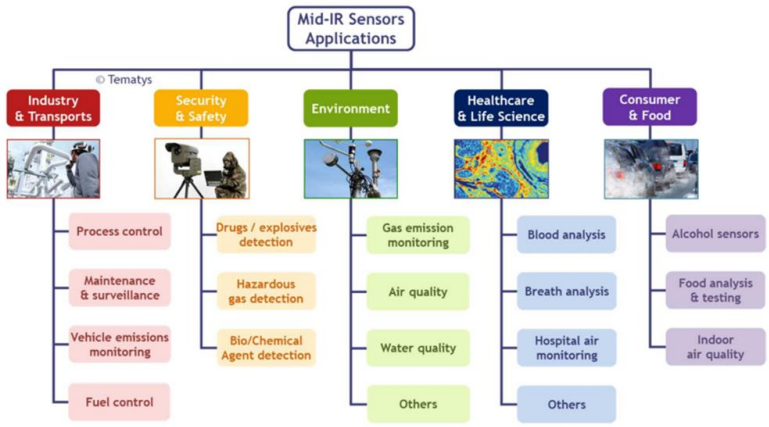

Fig.1.2. (a.) Mid-infrared absorption spectra of some important trace gases with their relative intensities from HITRAN data, image taken from [13]. (b.) Main mid-infrared sensing application, image taken from [14].

However, several existing applications for mid-IR spectroscopy are still based on free-space optics, while integrating photonics will promise numerous advantages. Connecting the mid-IR light source and the photonic circuits is a main point for developing mid-IR photonics applications. Therefore, there is a growing need for compact mid-infrared devices.

1.2 MID-IR PLATFORMS AND MATERIALS FOR ACTIVE AND PASSIVE DEVICES

Nowadays, research interest is based on miniaturized optical devices by integrating all devices in one chip, leading to portable and cost-effective systems [15]. In this section, I will provide a state-of-the-art mid-IR platform and material suitable for the demonstration of systems-on-chip.

1.2.1 Si-based Waveguide Platforms for Mid-IR

For the development of mid-IR photonics, a common requirement is to use a waveguide platform that allows light propagation with low loss in this spectral range. The transparent window of various materials with optical loss below 1 dB/cm can be seen in Fig.1.3.

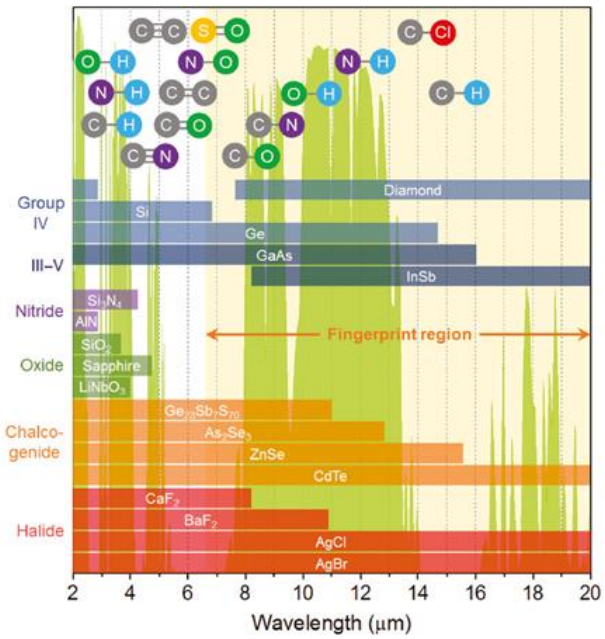

Fig.1.3. Different materials for photonics circuits operating in the mid-IR spectral regime: the

bars represent optical transparency windows of various materials, where material attenuation is lower than 1 dB/cm, the top panel shows where various chemical bonds primarily absorb light, and the background displays the infrared atmospheric transmission spectrum. Image taken from [16].

The silicon-based (Si-based) photonics has come up as a major photonics platform for creating efficient and cost-effective devices in the mid-IR domain. Si-based technology can provide substantial benefits as this platform exploits the existing complementary metal-oxide semiconductor (CMOS) technology by enabling low-cost and reliable large-scale fabrication [17]. Silicon transparency is not only in the NIR but also up to ~8 μm wavelength, and it is potentially a viable material for mid-IR applications [18].

Silicon-on-insulator (SOI) is the dominant waveguide platform in silicon photonics, especially for NIR applications. A compact device with a small footprint can be achieved due to the large refractive index contrast between silicon (n∼3.5) and silicon dioxide (SiO_2, n∼1.5). Although the transparency of Si waveguide core extends to 8 μm wavelength, the strong silica absorption is the main limitation for the use of conventional silicon-on-insulator (SOI) waveguides at a longer wavelength (beyond 3.6 μm) [19]. Several methods have then been reported to extend the operation of SOI platform to a larger wavelength. For example, S.A. Miller *et al.* reported a low loss below 1 dB/cm for wavelengths up to 6 μm by modifying the SOI waveguide design to reduce the light absorption of the mode overlaps partially in the silica layer [20]. However, this strategy is not compatible with the use of this SOI platform at a longer wavelength due to the expansion of the mode. Another approach is to use the suspended Si waveguides by under-etching the buried oxide (BOX) layer with the sub-wavelength grating (SWG) technology. A propagation loss of 3.1±0.3 dB/cm is achieved at the operating wavelength of 7.67 μm [21]. Nevertheless, this platform requires more sophisticated fabrication procedures, which makes it more complex and increases production costs. Therefore, alternative Si-based platforms have been evaluated to operate in the mid- and long-wave infrared.

Silicon-on-silicon nitride (Si_3N_4) and silicon-on-sapphire (SOS) are other platforms that have been investigated for mid-IR photonics. Several demonstrations have shown that these materials perform well in MWIR. To name a few works: a low propagation loss of 5.2 ± 0.6 dB/cm and 5.1 ± 0.6 dB/cm for the transverse-electric (TE) and transverse-magnetic (TM) modes has been reported for silicon-on-nitride waveguides at $\lambda = 3.39$ μm [22]. Also, the

demonstration of a CO_2 gas sensor based on a sub-wavelength silicon strip waveguide on a Si_3N_4 layer has been reported in 2018 [23]. This work has shown the possibility of sensing CO_2 concentrations down to 5000 ppm at a working wavelength of 4.23 μm. For silicon-on-sapphire, several research works have shown low propagation loss [24, 25], a high Q-factor for integrated ring resonators [26, 27], as well as supercontinuum generation with the upright T design [28]. Still, silicon nitride and sapphire also exhibit a transparency limit at around 4.5 and 5 μm wavelengths, respectively. It can be seen that the studies in existing literature have typically reported on wavelengths under 8 μm, while there is a significant demand for devices working in the long-wave infrared (LWIR). The development of Si-based platforms operating in the LWIR is very challenging because most of the commonly used materials, including Si, present an intrinsic material absorption in this regime.

Apart from the Si-based material, chalcogenide has been shown to be a promising platform due to its wide transparency window. Chalcogenide glasses microresonators monolithically integrated on silicon have been demonstrated for the first time by H. Lin *et al.*[29]. The intrinsic Q-factor of 2×10^5 at 5.2 μm wavelength has been reported. Nevertheless, while chalcogenide glass presents unique properties ideal for mid-IR applications, it faces limitations due to its chemical instability and lack of compatibility with CMOS technology. Meanwhile, III-V based platforms, like GaAs/AlGaAs, are also interesting. They have shown the wide transparent window covering from 1.6 to 16 μm wavelength. Also, using III-V materials can be benefiting from an integration with QCL laser source [16, 30]. Some worked has been reported by using GaAs platforms, including a Mach-Zehnder interferometer (MZI) integrated for sensing application within 5.8 - 6.3 μm wavelength range [31].

Interestingly, germanium (Ge) stands as an excellent candidate for extending the operation wavelength to operate in the LWIR. As seen before in Fig.1.3., Ge has a large transparent window up to 15 μm wavelength which allows an extension of the maximum operating wavelength beyond 8 μm (beyond Si absorption limit). In addition, Ge presents a strong third-order nonlinear ($\chi^{(3)}$) optical effect [32], which makes Ge a good material for the development of active devices. Moreover, Ge is already largely developed in silicon photonics, and it is compatible with the standard complementary metal-oxide semiconductor (CMOS) technology in terms of low-cost and high-performance fabrication processes [16]. Several Ge-based platforms have been studied to extend the operation wavelength to the MWIR and LWIR applications, including germanium on silicon (GOS), germanium on SOI (GOSOI), germanium

on insulator (GOI), germanium on silicon nitride (GOSN), and SiGe alloys. In the following, I will present the different research works on Ge-based technology.

Within the Ge-on-Si (GOS) platform, Ge acts as the core, where light is guided and confined, while Si functions as the cladding material. The first experimental demonstration of GOS photonics in the mid-IR was done by Y.-C. Chang *et al.* in 2012 [33]. In this work, the Ge strip waveguide on a Si substrate was fabricated with a 2 μm-thick monocrystalline germanium layer on a Si substrate. The lowest propagation loss achieved is 2.5 dB/cm at 5.8 μm wavelength, extracted by means of the Fabry–Perot resonance technique for transverse-magnetic (TM) polarization mode. They also reported the bending loss of 0.12 dB for a 90° bend with a radius of 115 μm. A low propagation loss for rib GOS waveguide of 0.6 dB/cm at 3.8 μm wavelength has been recorded by M. Nedeljkovic *et al.* from the University of Southampton [34]. Two years later, the same research group also demonstrated transmission measurements of GOS waveguides for longer wavelength in the mid-IR with a minimum propagation loss of 2.5 dB/cm at 7.575 μm wavelength; however, the platform became very lossy for longer wavelength (>15 dB/cm) [35]. In 2018, K. Gallacher *et al.* presented a study on propagation losses by using the GOS rib waveguide within the long-wave infrared, spanning from 7.5 to 11 μm [36]. Using the Fabry-Perot resonance method, they measured a propagation loss below 5 dB/cm for both TE and TM polarizations with a value as low as 1 dB/cm for wavelength larger than 10 μm for the TE polarization. Afterward, the demonstration of molecular fingerprint sensing with low loss waveguide was done by the same group based on this platform [37]. Recently, a ring resonator and thermo-optic tunability in GOS waveguides have been investigated for long-wave infrared photonic integrated circuits [38]. The ring resonances have been observed by the thermal-optics effect with the extracted Q-factors between 2×10^3 and 1×10^4. They also reported a propagation loss from 6 to 17 dB/cm in the wavelengths from 7 μm to beyond 11 μm. However, the GOS platforms have their intrinsic drawbacks. For example, the Si bottom cladding is expected to limit the device operation wavelength due to intrinsic Si absorption, or a defective Ge/Si interface from the lattice mismatch can affect the device's performance.

Another approach that has been demonstrated for MWIR is the germanium-on-SOI (GOSOI). This platform can benefit from thermal and electrical isolation due to the underlying SiO_2 buffer. This additional SiO_2 layer allows more efficient integrated thermo-optic phase shifters as reported in Ref. [39]. Also, a chip-scale Vernier tunable racetrack resonator filter on the Ge-

on-SOI waveguide platform has been demonstrated by S. Radosavljevic *et al.* [40]. A Q-factor of ~20000, operating at 5 μm wavelength range has been reported.

Ge-on-insulator (GOI) [41] and Ge-on-silicon nitride (GOSN) [42] have also been explored as potential platforms for mid-IR integrated photonics. GOI and GOSN offer a greater refractive index contrast between Ge (n = 4) and SiO_2 (n = 1.4) or SiN_x (n = 1.9), allowing effective light confinement in the core material. However, the limitations of these platforms are imposed by the optical transparency window of SiO_2 and SiN.

In addition, suspended Ge platforms have been considered as an ultimate way to benefit from the wide transparency of Ge, potentially from 2 – 15 μm without any limitation from cladding absorption. Several works have been done for the demonstration of resonators around 2 μm wavelength based on air-cladding Ge membranes. For instance, the photonic crystal cavity offers a moderate Q factor of 200 [43], a nanocavity with a Q-factor of around 18,000 [44], or another loaded Q-factor of ~57,000 has been achieved around 2 μm wavelength, using an air-cladding Ge micro-ring resonator [45]. This platform has also been developed for the LWIR. A first demonstration of low propagation loss based on suspended Ge waveguides was reported by A. Osman *et al.* in 2018 with a low propagation loss of 2.6 ± 0.3 dB/cm at 7.67 μm wavelength [46]. Later on, A. Sánchez-Postigo *et al.* proposed the use of suspended Ge waveguides with a subwavelength metamaterial lateral cladding [47]. In this way, the device can provide optical confinement while allowing structural suspension. A propagation loss of 5.3 ± 1.0 dB/cm at 7.7 μm wavelength has been indicated. However, processing the cladding removal is making the fabrication more complicated.

Apart from pure Ge-based waveguides, the use of SiGe alloys has been proposed. This platform benefits from having a low dislocation density (TDD), especially with a SiGe-graded layer. Using SiGe alloys allows a high versatility for engineering waveguide properties. The refractive index profile and dispersion properties of the waveguide can be optimized by controlling the concentration of Ge during the epitaxy growth process. Some promising results of low propagation losses of SiGe/Si waveguides compared to SOI in the mid-IR have been reported in the literature. For example, the work done by C. Grillet *et al.* presented a low-loss $Si_{0.6}Ge_{0.4}$/Si ridge waveguide, in which the loss was reported in the range between 1.5 dB/cm at 3.25 μm wavelength down to 0.5 dB/cm at 4.75 μm wavelength [48]. Additionally, the nonlinear optical response of this platform was also demonstrated in 2015 [49]. Graded SiGe/Si

waveguides were first investigated for the mid-IR application in 2014. In this case, the core of the waveguide was graded with a Ge concentration from 0 to 40%. The SiGe/Si stacks indicated a loss as low as 1 dB/cm at 4.5 µm and 2 dB/cm at 7.4 µm [50]. Based on this platform, passive function, i.e., arrayed waveguide gratings (AWG) operating at 4.5 µm [51] and 7.6 µm [52] have also been investigated. Recently, R. Armand *et al.* have illustrated the silicon–germanium ring resonator with a loaded Q-factor of 236,000 at 4.18 µm wavelength [53]. To date, this result has shown the highest Q-factor attained on this material platform and among the highest achieved within this wavelength range on a generally CMOS-compatible platform.

Besides implementing high Si concentration in the alloy, Ge-rich graded-index SiGe platforms have been investigated as an alternative approach for mid-IR integrated photonics. Thanks to the refractive index gradient, the optical mode will be guided through Ge-rich layers and far from Si substrate. Therefore, this platform is expected to enable a broader operational wavelength range, reaching up to 15 µm (full transparency window of Ge). Low-loss Ge-rich $Si_{0.2}Ge_{0.8}$ waveguides on SiGe-graded substrates for MIR-integrated photonics was demonstrated in 2017 by our group in collaboration between C2N (Paris-Saclay University) and L-NESS (Politecnico di Milano) [54]. Propagation losses of around 1.5 dB/cm and 2 dB/cm for quasi-TE and quasi-TM polarizations at 4.6 µm wavelength have been reported. Later than that, three different platforms based on the Ge-rich graded-index SiGe layers on Si substrate were proposed [55]. By fine-tuning the vertical refractive index variation in compact graded $Si_{1-x}Ge_x$ buffer, broadband low propagation loss around 2-3 dB/cm over a wavelength span from 5.5 µm to 8.5 µm for both TE and TM-polarization is obtained. Subsequently, passive photonic devices have been developed as a set of building blocks operating in the mid-IR up to 8.5 µm wavelength that can be further combined to form mid-IR photonic integrated circuits in the future. To name a few, dual-polarization Mach-Zehnder interferometers (MZI) [56], Bragg grating Fabry-Perot cavity [57], racetrack resonators with Q-factor of 3200 [58], integrated Fourier-transform spectrometer (FTS) [59], or a theoretical polarization rotator [60] have already been investigated. Moreover, the first active devices based on non-linear optics [61] and electro-optic [62] effects have been demonstrated as well.

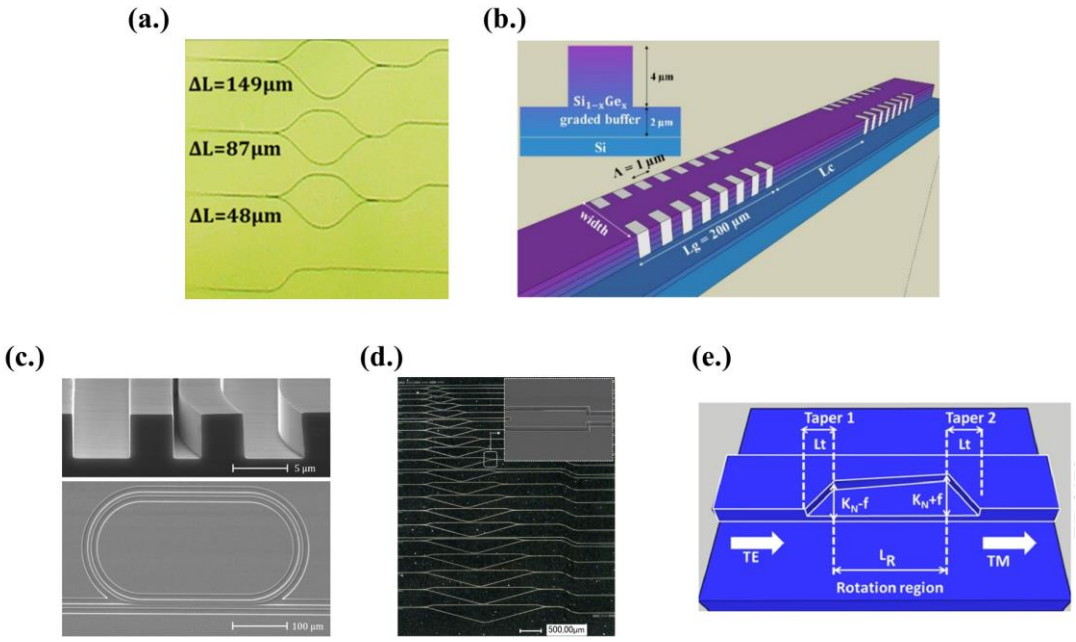

Fig.1.4. An illustration of passive optical devices-based SiGe graded-index platform operating in the mid-IR (a.) dual-polarization MZI [56], (b.) Fabry-Perot resonant cavity [57], (c.) racetrack resonators [58], (d.) integrated Fourier-transform spectrometer (FTS) [59], and (e.) a theoretical polarization rotator [60].

One focus of this Ph.D. work includes advancing high-Q resonators for LWIR operation. The work performed here will take advantage of the Ge-rich graded-index SiGe platform on the Si substrate to operate in the LWIR for the development of photonic-integrated devices.

1.2.2 Mid-IR Light Source

Besides the photonic circuit itself, a light source with high-performance capabilities is required. This has been a major area of research receiving a lot of attention because it is crucial for the integrated photonics industry. There are various ongoing research efforts using different methods to address an efficient light source. More details can be found elsewhere [63].

Although there has been a large development for group IV materials (silicon and germanium) for passive devices, they are not suitable for active devices due to their indirect bandgap properties. As known, the indirect bandgap material prevented efficient light emission. Several approaches are being explored to create effective silicon light-emitting devices that align with Si/Ge-based integrated circuit technology. Some progress has been made based on weak one- and two-phonon assisted sub-bandgap light-emission processes [64]. Recently, researchers

have moved their interest to GeSn alloy [65-69] thanks to its ability to achieve a direct bandgap structure. Nevertheless, the performance of this platform still requires improvement. Meanwhile, the III-V component has been shown to have a significant impact on developing optical sources due to their direct bandgap structure.

The III-V semiconductor materials are compounds of binary semiconductors from group III and group V from the periodic table such as GaAs, InSb, GaP, InAs, and their alloys. The III-V semiconductors have emerged as an ideal model for providing mature technology with light-emitting devices due to their direct bandgap structure. In this sense, the lowest of the conduction bands (CB) is in the same wavevector as the highest valence band (VB), leading to an efficient electron-hole pair radiative recombination. An example of the direct bandgap structure can be seen in Fig.1.5. In this case, the band plotted of InAs around the fundamental band gap (Γ-valley) is shown.

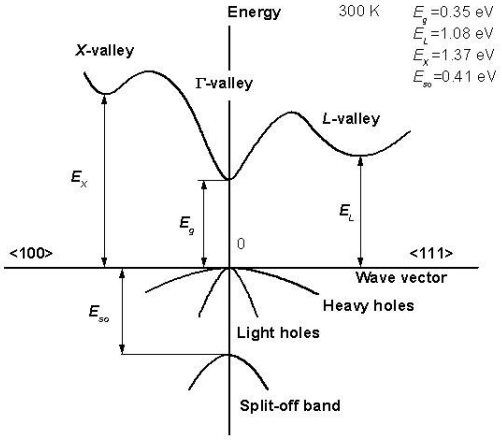

Fig.1.5. Band structure of InAs around the fundamental band gap (Γ-valley). The structure shows the direct bandgap behavior with approximately 0.35 eV. Image taken from [70].

Not only the direct bandgap behavior, which ensures excellent optical and electrical properties, III-V lasers are also able to provide a wide spectrum operation from the deep UV [71] to the far-infrared for the development of light sources. In fact, an emission in far-infrared of III-V material is due to the intersubband transition (ISB) in the conduction band. Interestingly, the quantum cascade lasers (QCLs) based intersubband lasers were finally demonstrated in 1994 [72]. Light emitted by QCLs originates from a radiative transition within a confined state of the electron in the conduction band. This differs from typical diode lasers, where the radiative

transition occurs across the material's bandgap, involving both electrons and holes. A key advantage of the QCL is that the energy of the lasing transition is insistent on the confinement energy of the electrons in the quantum wells, rather than the intrinsic bandgap energy of the material. Thanks to the band-structure engineered system, the frequency of the emitted light can be tuned by changing quantum well depth and thickness. The schematic view of the QCLS based intersubband transition can be seen in Fig.1.6. The energy transitions happen between quantized levels within the conduction band.

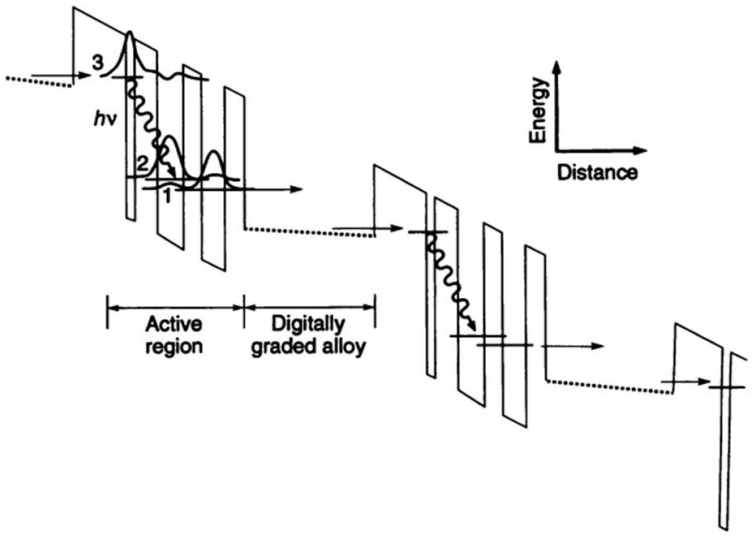

Fig.1.6. Schematic conduction band diagram of the quantum cascade laser relying on intersubband transitions. The laser transition has been shown in wavy arrow. Image taken from [72].

Several couples of III-V semiconductors have been demonstrated the QCL operated in the mid-IR, for example, InGaAs/AlInAs on InP substrates, GaAs/AlGasAs on GaAs substrate and InAs/AlSb on InAs substrate [73].

The InAs/AlSb material was successfully demonstrated for the development of quantum cascade lasers in a wideband spectrum. It shows both the shortest and the largest wavelength QCLs [74]. The low threshold InAs/AlSb QCLs operated near room temperature with the emitting near 15 μm for CW operation, and near 20 μm for pulse operation has been reported by A. N. Baranov *et al.* [74] and also emission at short wavelength of 2.6 μm [75].

Another advantage of the InAs/AlSb material system is the possibility of growing the QCL

active region directly on the Si platform. Interestingly, the first InAs/AlSb QCL directly grown on a Si substrate and working at 11 µm wavelength has been done recently by H. Nguyen-Van *et al.* from IES, University of Montpellier [76]. Therefore, the III-V laser-based InAs/AlSb QCL has been chosen to be an active device for the monolithic integration, which will be described later in this manuscript.

1.3 MID-IR PHOTONICS CIRCUITS COUPLED WITH THE LIGHT SOURCE

To go for practical applications, the light source has to be integrated in a compact way with the photonic circuits. Different approaches have been studied in the literature that will be detailed hereafter. The monolithic integration of QCL on a SiGe-based photonics platform has been addressed under the framework of the ANR Light-UP project (C2N/Paris-Saclay Univ., IES/Univ. de Montpellier, and L-NESS/Politecnico Di Milano) in which I have been fully involved during these 3 years. The challenge of this project is to combine high-performance active sources and versatile waveguide platforms by direct growth QCL devices on the Ge-based photonic integrated circuits. In this section, I will first discuss the different methods for light source integration. Then, I will provide the context of monolithic QCL integration with the SiGe platform, showing the preliminary design and simulation results for such coupling strategy that was performed before the start of my PhD.

1.3.1 Integration Approach

There have been several demonstrations of light-emitting devices integrated on Si/Ge-based photonic platforms in recent years. In this section, two main integration approaches will be discussed.

1.3.1.1 Heterogeneous Integration

Heterogeneous integration is one approach for photonic integration, where III-V epitaxial layers or devices are grown on their native substrates [77, 78], and then transferred onto a Si substrate. In general, there are three different approaches for heterogeneous integration, including die-to-wafer or wafer-to-wafer bonding, flip-chip integration, and micro-transfer printing, as seen in Fig.1.7.

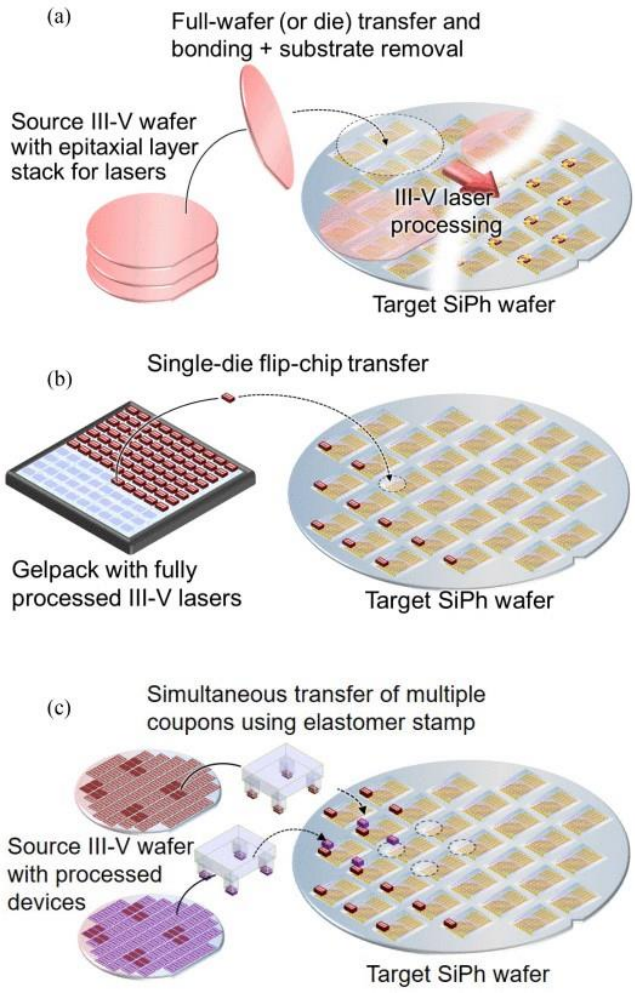

Fig.1.7. Illustration of the III-V-on-Si heterogeneous integration with different techniques (a.) wafer-to-wafer bonding, (b.) flip-chip, and (c.) micro-transfer printing. Image taken from [79].

Die-to-wafer bonding and wafer-to-wafer bonding are techniques that bypass some problems faced in growing materials directly (hetero-epitaxial growth) on a silicon photonic wafer. Instead, these methods involve growing the materials on their original substrate first [80, 81]. After that, they are connected or bonded to the Si photonic wafer, usually after the Si front-end processes are done. However, this method still requires removing the original substrate and creating patterns on the devices after bonding, which can make its final development more challenging. Flip-chip integration is another method largely adopted in industry. This process offers easy integration of the prefabricated III-V devices on Si by using a solder bump. The downside of this approach is the requirement of accurate alignment and the limited integration density [82, 83]. In 2004, the group of J. A. Rogers from the University of Illinois demonstrated a novel integration technique, so-called micro-transfer-printing (μTP) [84, 85]. This method

enables the manipulation of micrometer-sized thin film devices and the transfer of these thin films to a target substrate with high alignment accuracy. By using this approach, different devices can be fully integrated on a common substrate. This heterogeneous integration has already succeeded in producing very exciting results in the near-infrared region. For example, a work reported by Y. Halioua *et al.* has experimentally demonstrated lasing operation with a low threshold of an InP-based photonic crystal (PhC) wire cavity laser bonded to a silicon wafer [86]. Another aspect that should be considered when bonding the III–V materials to Si waveguide circuits is how to achieve efficient optical coupling between the III–V layers and the Si waveguides. The evanescent coupling has shown the most promising results. This occurs when the laser and waveguide are positioned in close proximity, allowing electromagnetic field of the laser penetrates into the waveguide via the evanescent field.

However, there is some evidence that the heterogeneous strategy of III–V semiconductor laser heterostructures on the Si PICs may not be ideal on a mid-to-long-term basis, particularly concerning integration density and economic perspective [87].

1.3.1.2 Monolithic Integration

While heterogeneous integrations have offered an opportunity to integrate numerous III-V lasers onto Si substrates, monolithic integration comes up as a promising solution for integrating III-V lasers on Si substrates with dense integration density. The monolithic integration is based on the direct epitaxial growth of III-V semiconductors on the Si platform. The challenges of this strategy mostly involve anti-phase domains (APDs), dislocations, and thermal cracks due to the difference in the physical properties between III-V materials and group IV materials [88]. The APDs are caused by the different polarities of III-V (polar material) and group IV (non-polar material). It can create a short circuit in the devices and degrade their electrical characteristics. Numerous research studies are dedicated to overcoming this challenge. GaAs and GaP-based lasers grown on CMOS-compatible (on-axis) Si substrates by using metal-organic vapor phase epitaxy (MOVPE) have been established as a possible way to grow III-V laser structures on those platforms [89, 90]. The lattice mismatch between III-V and IV materials can introduce a high density of threading dislocations (TDs), which affects the laser performance by creating a dangling bond and non-radiative recombination centers. It should be noted that TDs cannot be avoided; however, they can be reduced by growing defect filter layers (DFLs). Additionally, the mismatch of thermal expansion coefficients may induce

the formation of macroscopic cracks in the epi-materials during cooling down at high temperatures (>500 °C). However, the mismatch of thermal expansion can be avoided by using slow temperature ramps during cool down.

Interestingly, as mentioned earlier, the recent work done by our collaboration from IES [76] reported a direct growth of InAs/AlSb QCL on a Si substrate at a working wavelength of 11 µm. The laser has revealed high performances with the longest emission wavelength of any laser integrated on Si. In addition, the antimonide-based QCL also demonstrated compatibility with the device fabricated on their native InAs substrate. This opens the route for light coupling from the QCL to the group IV-material waveguide.

It is worth mentioning that the monolithic integration of III-V devices on a Si-based platform has paved the way for new functionality, low-cost, and dense integration in the next generation of photonic integrated circuits (PICs) [91].

1.3.2 Mid-IR QCL-based III-V Material Integrated on Ge-based Photonics Platform

1.3.2.1 Context and Objective

The ANR Light UP project addressed the monolithic integration of InAs/AlSb – based Quantum Cascade Lasers (QCLs) on SiGe photonics platform. The groundbreaking concept is to grow the III-V based-QCL material directly on the Ge-based photonics integrated circuits. III-V platform–based QCL is a good solution for a light source due to its power efficiency, spectral performance, and ability to operate at room temperature [92]. As mentioned above, InAs/AlSb has been shown to be a compatible material for developing QCL in broadband spectra. In this regard, InAs/AlSb QCL has been considered as an active material in this work.

The monolithic integration of III-V based-QCL onto Ge-based PICs offers a compelling solution for a high-capacity, wafer-level mid-IR photonics platform. This direct integration benefits from the absence of an intermediary layer between the QCL and Ge-based waveguide, leading to effective heat dissipation and optimal device performance. In fact, InAs/AlSb QCL is also the only material platform showing successful growth on a Si substrate operating at room temperature.

The mid-IR QCL integrated on SiGe platform provides a promising potential for the development of photonics integration aiming to enable electrically driven and fully packaged

mid-IR PICs. In the long term, this platform is expected to be used for various purposes, such as free space communication, environmental monitoring, sensing, and astronomy. We thus expected high performance, low cost, compactness, low weight, and low power consumption of photonic devices in the end.

Before the start of my PhD, the coupling of light from QCL to a SiGe-based platform was investigated numerically, and the results are reported below. Indeed, these results guided my research works, especially the need for deep-etched corrugated mirrors to support the contra-directional grating-assisted coupling, and the necessity to achieve electrical injection from back side contact. From this analysis, the two challenging points that I had to address have been identified to be (i) the electrical contacts and (ii) the realization of the optical cavity and more precisely the coupler between the III-V gain material and the SiGe passive waveguide.

1.3.2.2 Design and Simulation of light coupling from QCL to SiGe Photonic Circuits

The monolithic integration of the QCL source on SiGe photonics circuits needs to tackle the challenge of light coupling from QCL to SiGe photonics circuits. Indeed, because of the index mismatch between QCL and SiGe, the coupling of the light from the laser grown on top of the waveguide to the waveguide is not feasible by evanescent coupling, as what is usually done in the telecom wavelength range. To illustrate, the mode calculation of the hybrid structure consisting of the III-V QCL on top of SiGe waveguide has been evaluated first. The III-V stack has been adapted from previous work operating at 11 µm wavelength [76]. For the SiGe layer, a 6 µm-thick graded layer from pure Si to pure Ge is considered, as reported previously [55]. The description of the layer and optical properties (real and imaginary parts of the refractive index) used in the simulations are reported in Table 1.1.

	thickness(µm)	real part of the refractive index n	imaginary part of the refractive index k
InAs cladding	1.4	3.03	4e-3
InAs spacer	1.75	3.4	0
active region	2.1	3.36	0
InAs spacer	1.75	3.4	0
InAs cladding	1.5	3.03	4e-3
InAs buffer	0.2	3.4	0
GaSb buffer	1	3.8	2e-4
SiGe	6	graded from 3.47 to 4.01	0
Si	substrate	3.47 [*]	0

[*] : https://refractiveindex.info/?shelf=main&book=Si&page=Shkondin

Table 1.1: description of the layer stack of the QCL on top of the SiGe waveguide with their refractive index (real and imaginary parts) used in the numerical simulations.

The simulated structure is shown in Fig.1.8(a.), with the refractive index profile in the vertical direction in Fig.1.8(b.). The effective indexes of the modes propagating in the hybrid structure have been calculated. The evolution of the effective indexes with the waveguide width (W) is reported in Fig.1.8(c.) for the fundamental TM mode confined in the QCL region and the fundamental TE and TM modes confined in the SiGe waveguides. Examples of mode calculations at 7.4 µm wavelength (TE and TM mode in SiGe waveguide and TM mode in QCL active region) for W = 8 µm are reported in Fig.1.8(d.). From this calculation, it can be seen that phase matching cannot be obtained when varying the waveguide width, which is explained by the fact the refractive index of III-V material is always lower than the one of SiGe alloys and even of the Si substrate. Thus, evanescent coupling of the light from the laser region to the SiGe waveguide will not be possible.

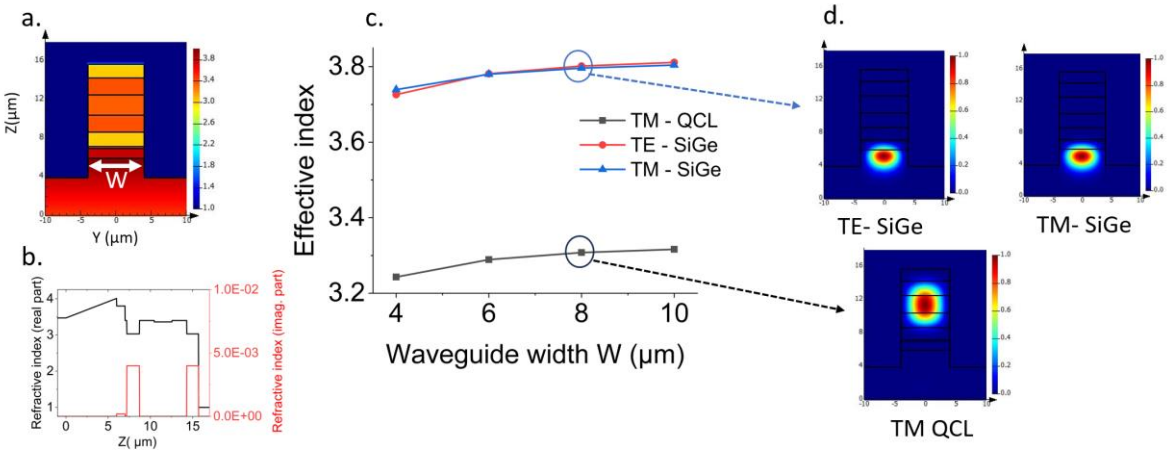

Fig.1.8. (a.) Visualization of the structure composed of QCL structure on top of SiGe waveguide, (b.) The real and imaginary part of the refractive index along the vertical axis (z-direction). (c.) effective index of the fundamental TM mode in QCL and fundamental TE and TM mode in SiGe waveguides as a function of the waveguide width, showing that mode matching cannot be obtained by tuning the waveguide width. (d.) examples of mode calculations at 7.4 µm wavelength (TE and TM mode in SiGe waveguide and TM mode in QCL active region).

Grating-assisted coupling between III-V and SiGe waveguides has thus been investigated. Indeed, from coupled mode theory, it is known that a periodic perturbation in the refractive index between two different waveguides can be used to achieve phase matching and to optimize the energy transfer between two different waveguides [93]. The phase-matching condition can then be written as

$$\beta_a \pm \beta_b = m \times \frac{2\pi}{\Lambda} \tag{1.1}$$

Where β_a and β_b are the propagation constants of the Bloch modes under interest in the uncoupled waveguides, Λ is the period of the corrugation, and m is the coupling order. The sign – (resp. +) corresponds to the co-directional/contra-directional coupling condition. Considering a waveguide width of 8 µm and the effective index of the guided modes reported in Fig.1.8(c.), the period of the grating can thus be calculated to obtain phase-matching conditions between the fundamental TM modes of QCL and SiGe waveguides. The following period can be deduced for coupling at 7.4 µm wavelength: for co-directional coupling Λ = 15·15 µm; 30·30 µm; 45·45 µm resp. form = 1, 2, 3 resp.; for contra-directional coupling: Λ =

1.04 µm; 2.08 µm; 3.12 µm resp. for m = 1, 2, 3 resp. Because of the large values of the calculated periods for the co-directional condition, such a device would suffer from radiation losses, this is why contra-directional coupling is investigated in the following. While the phase matching condition gives insights into the periodicity required to obtain contra-directional coupling as a function of the targeted wavelength, numerical simulations are required to estimate the coupling coefficients as a function of the specific corrugation design. As the corrugation needs to overlap with both the QCL and SiGe modes, the periodic structure is then obtained by periodic variation of the waveguide width W, as shown in Fig.1.9. Rectangular corrugations are considered in the following simulation, while smoother bent corrugations could be used in practice.

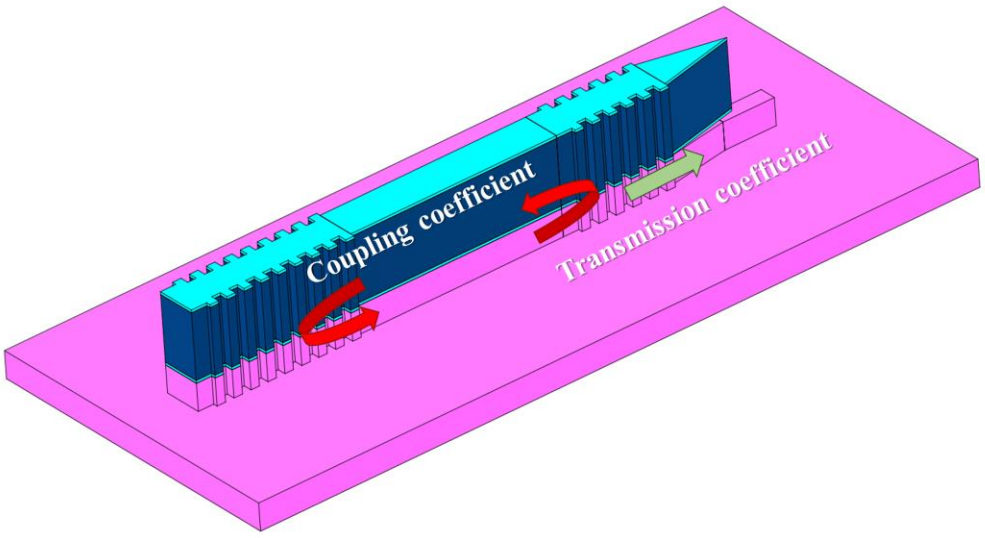

Fig.1.9. 3D schematic view of the coupler. The red arrow indicates the coupling from QCL to SiGe, and the green arrow indicates the transmission from SiGe to SiGe.

A waveguide width (W_{guide}) of 6.6 µm is considered, with a corrugation W_{corr} of 1.6 µm on each side of the waveguide, as shown in Fig.1.10(a.). EME solver from ANSYS/Lumerical is used to calculate the properties of such periodic structure. The length of the elementary segments, d_1, and d_2 have been determined to obtain coupling around 7.4 µm. A third-order grating is considered in order to obtain dimensions easily compatible with device fabrication. $d_1 = d_2 = 1.585$ µm is then used in the following.

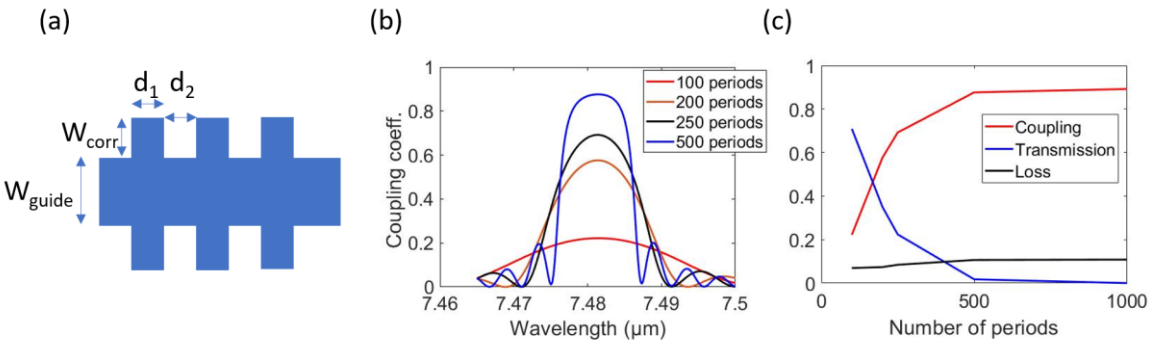

Fig.1.10. (a.) Top view of the grating-assisted coupler: the corrugation is obtained by periodic variation of the waveguide width. Simulation parameters can be seen in the schematics. In the following simulations: W_{guide} = 6.6 µm, W_{corr} = 1.6 µm, d_1 = d_2 =1.585 µm. (b.) Contra directional coupling coefficient between QCL and SiGe waveguide, as a function of the wavelength. (c.) Contra directional coupling, transmission, and loss coefficient as a function of the number of periods of the corrugation.

From this calculation, it can be seen that coupling from QCL to SiGe waveguide can be obtained. Coupling coefficients up to 89% are obtained for a couple with 1000 periods, corresponding to a 3.1 mm-long coupler, while smaller values are obtained for shorter couplers (70% of the power is coupled for 0.8 mm-long couplers). It is worth noting that the bandwidth of the coupler is limited to around 10 nm in this calculation. Finally, the central wavelength (7.48 µm in this case) can be adjusted by tuning the corrugation period.

From this modeling, we can see that deep-etched (more than 10 µm) corrugated waveguides with a period of around 1.585 µm are necessary to be developed, which forms the first challenge to overcome, while the second one is related to the electrical injection through the substrate and the SiGe waveguide.

1.4 Outline of the Thesis Manuscript

The following of manuscript is dedicated to my work, divided into 4 chapters, which are detailed hereafter.

Chapter 2. Developments toward a monolithically integrated QCL source on SiGe platform: This chapter will present the fabrication process development for the monolithic integration of a QCL source on SiGe-graded index material. Two main challenges aspects will

be discussed. I will start with the study of the electrical contact via bottom contact through the n-doped Si substrate. The optical and electrical properties of the 6-µm graded index on Si n-doped substrate are then studied. As the obtained results have paved the way for an integrated electro-optical modulator (EOM) operating in the mid-IR, a summary of this work is also discussed. Then, the fabrication process development that has been done for the monolithic integration of the source is reported. Unfortunately, the epitaxial growth of antimonide QCL on SiGe templates was more challenging than expected; thus, it was not possible for the moment to push this work up to the demonstration of a monolithically integrated QCL source.

Chapter 3. Butt-Coupling of Quantum Cascade Laser (QCL) to SiGe platform on two separate chips: Considering the challenges in terms of epitaxial growth for the monolithic integration of QCL source on SiGe template, an alternative approach has been proposed, based on the butt-coupling between QCL and SiGe photonics circuits. In this chapter, I will present the associated challenges, the experimental set-up that has been built to this end, and the first demonstration of light coupling between antimonide-based QCL and SiGe photonics circuits at 7.4 µm wavelength.

Chapter 4. Broadband Racetrack Resonator in the LWIR: Finally, in parallel with the work dedicated to the source coupling, I have also been involved in the development of SiGe photonics circuits in the mid-IR. More specifically, I have studied and developed racetrack resonators, which the objective to achieve the first high-quality factor resonator operating in the LWIR. In Chapter 4, I will discuss the state of the art of integrated resonators, but also the challenges related to the characterization of photonics devices with high resolution in the mid-IR Design, fabrication, and experimental demonstration of racetrack resonators are then reported, showing high Q factor resonator (1×10^5) operating at 7.45 µm wavelength.

Chapter 5. Conclusions and Perspectives: The general conclusions of this PhD manuscript will be reported. Moreover, the perspectives to go a step further from this PhD work will also be discussed.

2 DEVELOPMENTS TOWARD A MONOLITHICALLY INTEGRATED QCL SOURCE ON SIGE PLATFORM

This chapter is dedicated to the development of the fabrication process for the monolithic integration of a QCL source on SiGe-graded index photonics circuits. Within this chapter, two primary challenges aspects will be tackled: i) establishing electrical contacts for the QCL laser and ii) realizing the optical cavity, specifically the coupler between the III-V gain material with the SiGe passive waveguide. At the end, a comprehensive summary will be presented.

2.1 ELECTRICAL CONTACTS: BOTTOM CONTACT THROUGH SIGE WAVEGUIDES GROWN ON DOPED SI SUBSTRATE

The co-design of graded SiGe and III-V epilayers was defined and discussed in Chapter 1. The schematic view of the targeted device is depicted in Fig.2.1(a); the blue color defined the QCL on top of the SiGe platform (pink color). The details of the material layer stack can be seen in Fig.2.1(b). This epitaxial stack has been adapted from the III-V on Si operated at 10 µm wavelength [94] and re-design by changing the thickness to work at 7.4 µm. The same GaSb and InAs buffer intact has been kept, but the thickness of the active region has been modified proportionally to the new working wavelength. In the final device, the InAs doped layer will be served as a cladding top contact (purple color in Fig.2.1(b)).

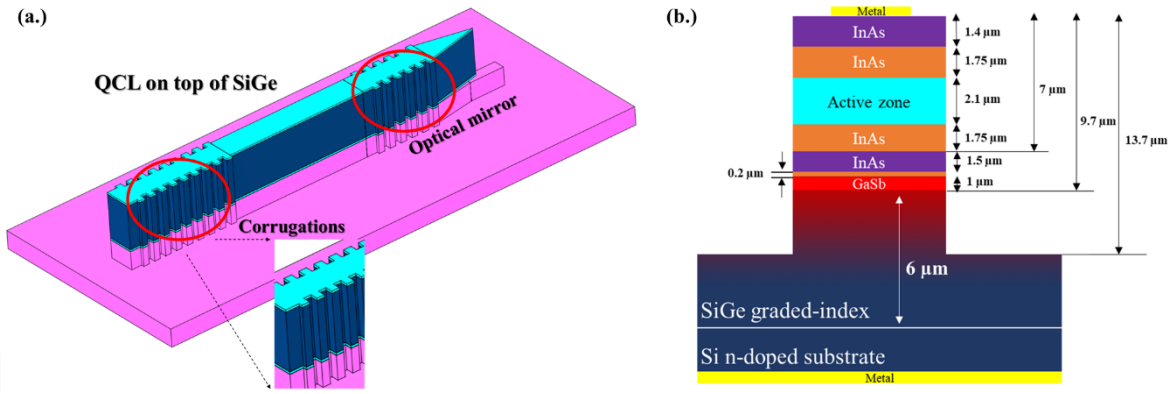

Fig.2.1. (a.) Schematic view of the final device illustrating the QCL (blue color) on top of the SiGe platform (purple color) with 2 optical mirrors made by corrugations (b.) Side view of the growing material.

Based on the different strategies in the literature to couple the light between different waveguides, the contra-directional grating-assisted coupling has been proposed as the only

suitable solution to couple the light from the active region to SiGe platform due to the phase matching between them. To do so, the cavity is made of 2 distributed Bragg reflectors, and then the cavity will be pumped by electrical injection. Typically, the metal contacts for Si and Si-Ge photonics are positioned directly on the top surface. In this case, the electrical injection is required to be done on the top of QCL material, the general SiGe top contact will be the caused to prevent the current flow from the QCL to the SiGe platform. Therefore, considering the complexity of the fabrication process to achieve the final devices, it was proposed to investigate the possibility of using a backside on silicon contact as the bottom contact of the QCL. In this regard, a highly doped silicon substrate can be used, on top of which a lightly doped graded SiGe layer can be grown, that will be used for the optical waveguide. The doping concentration of the graded SiGe layer will then come from a compromise between low access resistance from the bottom contact to the QCL, and low propagation losses of the optical waveguide. Hence, it is important to verify both the optical properties and the electrical properties of the SiGe material, i.e., the possibility of achieving simultaneously low propagation losses and low access resistance from a bottom-doped substrate to the QCL on top, to validate this approach for the monolithic integration.

In detail, low-loss waveguides have been obtained previously using graded SiGe waveguides, but non-intentionally doped layers were used. The presence of dopants results in an increase in the optical losses of the waveguide. As know, the free-carrier plasma effect relies on altering the electron and hole concentrations within crystalline material, thereby impacts both the material's absorption coefficient (Δα) and refractive index (Δn). In this regard, analytical calculations can be performed to estimate this effect. Since a significant portion of the optical mode travels through the Ge-rich region of epitaxial growth, we are able to use the model described in Ref. [95] to estimate the optical absorption due to the effect of the free-carrier electron absorption in Ge. As seen in Ref [95], they have proposed a convenient design tool for modeling device properties based on free-carrier absorption in Ge. In this context, the absorption coefficient (cm^{-1}) of Ge at different doping concentrations can be calculated by using this expression:

$$\Delta\alpha(\lambda) = \Delta\alpha_e(\lambda) + \Delta\alpha_h(\lambda) = a(\lambda)\Delta N_e^{b(\lambda)} + c(\lambda)\Delta N_h^{d(\lambda)} \quad (2.1)$$

where, $\Delta\alpha(\lambda)$ represents the absorption coefficient increase at a specific wavelength of interest, $a(\lambda), b(\lambda), c(\lambda), d(\lambda)$ is the wavelength-dependent coefficients that can be also found in Ref

[95], ΔN_e and ΔN_h stand for the increase electron and hole doping concentration, respectively. The optical losses for different values of the doping concentrations can then be calculated from the absorption coefficient. The results are reported in Table 2.1.

Wavelength (µm)	N-doping (cm^{-3})	Losses (cm^{-1})	Losses (dB/cm)
7.4	1.5×10^{15}	0.12	0.51
	5×10^{15}	0.41	1.76
	1×10^{16}	0.82	3.57

Table 2.1.: Calculation of losses due to free-carrier absorption considering different doping concentrations of lightly n-doped Ge at 7.4 µm wavelength.

From this calculation, it can be seen that moderate losses are obtained for a doping concentration of a few 10^{15} cm^{-3}, while it should be avoided to increase the doping concentration up to 10^{16} cm^{-3}.

Based on this first result, it is now necessary to evaluate the access resistance of the SiGe layer. To this end, test devices will be fabricated, based on the configuration shown in Fig.2.2(a), to experimentally assess the corresponding resistance. Before going to the experiment, the resistance of the SiGe layer can be evaluated theoretically, taking into account, firstly, the resistivity as a function of the impurities concentration for Si and Ge, taken from Ref [96] as seen in Fig.2.2(b).

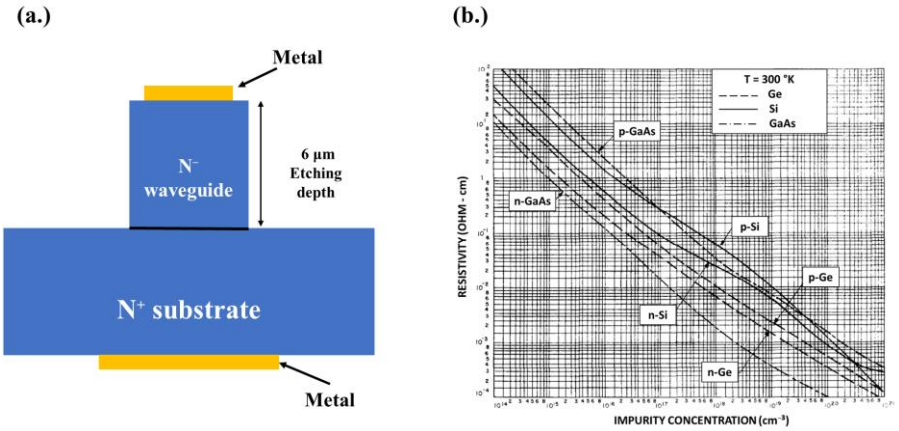

Fig.2.2. (a.) Schematic cut-view of the device for the bottom contact test (b.) The resistivity vs. impurities concentration for Si and Ge at 300 K. Image is adapted from [96].

From Fig.2.2(b.), the resistivity of Si and Ge at different doping concentrations can be extracted. The resistivity at each doping concentration can be found in Table 2.2. While there is no data on SiGe alloys, it can be estimated that SiGe resistivity should be in between the resistivity of Si and Ge.

N-doping (cm^{-3})	Resistivity for Si ($\Omega \cdot cm$)	Resistivity for Ge ($\Omega \cdot cm$)
1.5×10^{15}	3	1
5×10^{15}	1	0.4
1×10^{16}	0.62	0.2

Table 2.2.: Resistivity ρ for Si and Ge at different doping concentrations.

To calculate the access resistance of the SiGe layer, a 6-µm thick, 7-µm wide, and 4-mm long device has been considered which corresponds to estimated dimensions of the final device. Using the expression of the resistance in a wire $R = \rho \frac{L}{A}$, the access resistance can be calculated. Here, ρ is the resistivity as reported on the table above, L represents the thickness of the device, which is 6 µm, and A denotes the surface area derived from multiplying the width and length of the device. The resulting access resistance for various doping concentrations is then listed in Table 2.3.

N-doping (cm^{-3})	Access resistance for Si (Ω)	Access resistance for Ge (Ω)
1.5×10^{15}	6.4	2.1
5×10^{15}	2.1	0.8
1×10^{16}	1.3	0.4

Table 2.3.: Calculated access resistance for Si and Ge at each different doping concentration for a 4-mm long device and 7-µm wide.

It can be seen that with a doping concentration between 1.5×10^{15} and 10^{16} cm^{-3}, access resistance is estimated to be between 0.4 and 7 ohms for a 4 mm long device, which is low enough to be considered as a good contact for the QCL integrated on top of the SiGe waveguide. From this calculation, it can be concluded that a low N-doping of 2×10^{15} - 5×10^{15} cm^{-3} could be a good compromise between low losses and low access resistance. It is worth

mentioning that SIMS measurement on previous non-intentionally doped wafers gave a residual electron concentration estimated to 1.5×10^{15} cm^{-3}. This is why in the following, a non-intentionally doped layer will be considered, as the residual doping should be compatible with the targeted values. Next, the waveguide optical properties and the access resistance will be experimentally investigated. To this end, I have designed, fabricated, and characterized tests structures. As the first objective, the optical propagation losses of the waveguides will be discussed. The influence of the doped substrate on propagation losses will be investigated. Then, the electrical characterization, including the design, fabrication, and measurement, will be demonstrated. In the end, an integrated electro-optical modulator (EOM) operating in the wide range of MIR will be reported. This device has been made possible thanks to the results obtained during the characterization of the backside contact. I would like to note that the cleanroom techniques and procedures that shall be reported hereafter are processes similar to those of M. Montesinos (a former Ph.D. student at C2N). I have acquired a considerable amount of knowledge and techniques under his guidance and that of X. Le Roux (Former engineer at C2N) during the initial phase of my Ph.D. thesis.

2.1.1 Waveguide Optical Properties

First, a 6-µm-thick graded SiGe layer is grown on a highly n-doped (Si) substrate with a 2×10^{19} cm^{-3} doping concentration using low-energy plasma enhanced chemical vapor deposition (LEPECVD) by our collaborators in the Laboratory for Nanostructure Epitaxy and Spintronics on Silicon (L-NESS) in Italy in the group of G. Isella. The graded SiGe layer is grown by linearly increasing the germanium (Ge) concentration from 0 to 100%, inducing a linear increase in the waveguide's refractive index. The graded epitaxial layer has a residual doping concentration estimated to be in the order of 10^{15} - 10^{16} cm^{-3}. Using standard cleanroom techniques, I first fabricated optical waveguides with spiral designs to achieve different on-chip propagation lengths. The waveguide has been designed with dimensions of 6-µm width and 6.8-µm of etching depth. In order to facilitate a good coupling, the width at the input and output waveguides of the chip has been set to 50 µm, followed by a 2 mm-long taper to reach the targeted width of the waveguide of 6 µm. A set of waveguides in a spiral shape with increasing lengths from 0.56 to 7.2 cm has been fabricated. The bending radius of the spiral has been set to be larger than 600 µm to avoid the bending loss from the structure. The general fabrication process flow is illustrated in Fig.2.3. and detailed hereafter.

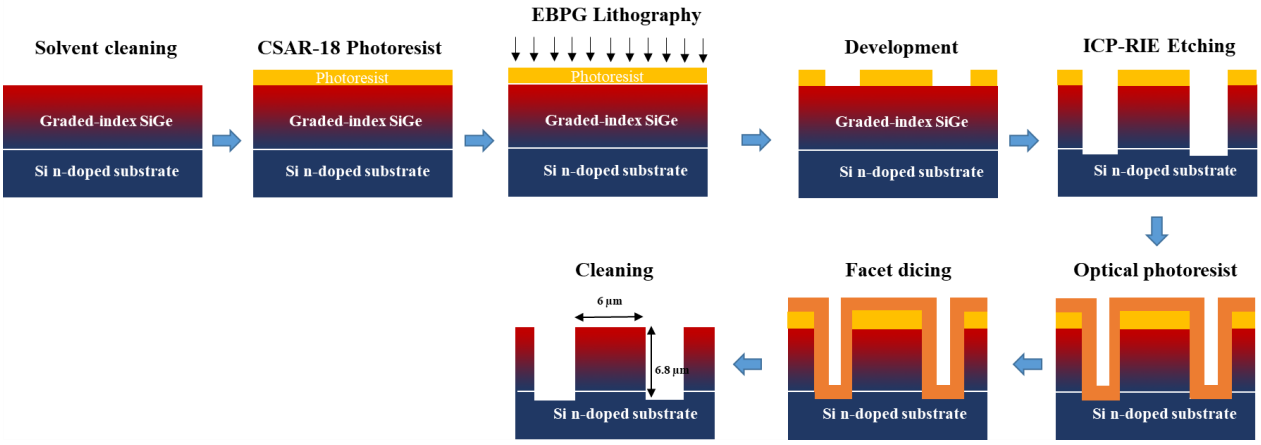

Fig.2.3. Simplified process flow of the spiral waveguide fabrication process.

A sample piece of around 2×2 cm^2 is first manually cleaved from the 4-inch wafer. Then, the sample is cleaned for 10 minutes with acetone and then with isopropanol using an ultrasound cleaning machine, followed by oxygen plasma for 3 minutes. Next, an electronic photoresist, AR-P 6200.18 (CSAR-62), also-called CSAR.18 is deposited upon the sample surface. The CSAR.18 is spin-coated on the sample surface with a speed of 1450 rpm within 60 seconds, followed by 5 minutes of annealing at 180°C on the hot plate. A photoresist layer of about 1.4-µm-thick is obtained. The waveguide patterns are defined by electron beam (EBPG) lithography with a current of 20 nA and a dose of 280 µC/cm^2. After the illumination of the photoresist, development with ZED-N50 developer has been used for 2 minutes, followed by 30 seconds of IPA. The SiGe sample is etched by ICP etching (ICP-DRIE SPTS) to define the etching depth. It should be noted that the use of ICP etching is performed by a combination of two different gases; the first one is SF_6, which is used to etch the SiGe material, and the other is C_4F_8, which is the passivated gas in the etching process, therefore, the etching speed is then controlled by the ratio between two gases. Finally, the waveguide facets are defined by mechanical dicing by using a diamond blade with a fine grain to reproduce the waveguide facet with similar coupling conditions. In the end, the photoresist is removed by putting the sample in an acetone bath during 5 minutes, followed by 5 minutes in IPA. To ensure a sample cleaning, a plasma oxygen cleaning procedure is executed for a duration of 10 minutes. As an additional concluding step, an optional piranha cleaning bath containing hydrogen peroxide (H_2O_2) and sulfuric acid (H_2SO_4) in a ratio of 1:3 can also be employed to guarantee effective cleaning. The SEM image of the spiral waveguide can be seen in Fig.2.4.

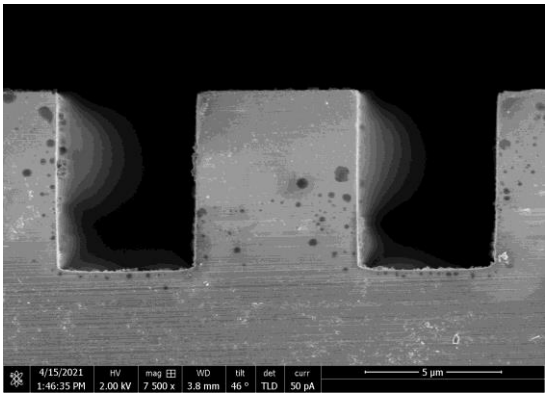

Fig.2.4. SEM image of the 6-µm width waveguide after the fabrication.

Once the fabrication had been done, the cut-back method was then used to determine the propagation losses of the fabricated waveguides for both TE and TM polarization measurements from 5 to 11 µm wavelength. The device was characterized by using the free-space mid-IR setup. A schematic view of the setup is shown in Fig.2.5.

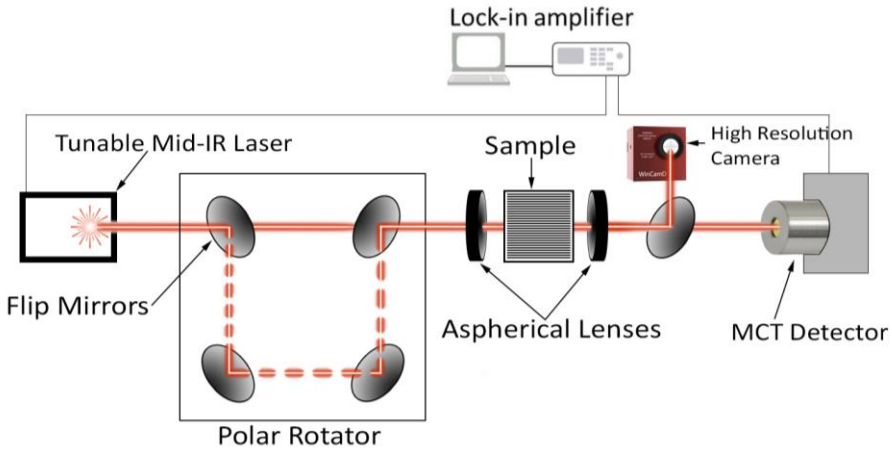

Fig.2.5. Schematic image of the mid-IR characterization set-up.

A broadband external cavity quantum cascade laser (QCL) (MIRCAT, Daylight Solutions), with a duty cycle of 5% and repetition rate of 100 kHz, has been used to measure the transmission of each waveguide. The laser contains four laser chips [97], which provide a tunable wavelength range from about 5.1 µm (1960 cm^{-1}) to 11.2 µm (890 cm^{-1}). Thanks to the use of a pair of aspherical lenses (ZnSe), the light can be coupled into and out of the sample. Then, the light at the output is sent to either the camera to ensure the fundamental mode coupling in the waveguide or to a MCT (HgCdTe) photodetector (DSS-MCT (14)020, Horiba). The detected signal is collected through a lock-in amplifier synchronized with the laser. It is

important to note that the voltage detected from the lock-in amplifier is directly related to the optical power collected by the MCT detector, as shown in the figure below. The spiral waveguides have been measured at a wavelength range from 5.5 µm up to 11 µm in a step of 4 nm. Examples of measured transmission with three different waveguide lengths are represented in Fig.2.6. for TE and TM polarization. The oscillations appearing in the measured transmissions between 5 and 7.5 µm wavelengths are due to the presence of numerous atmospheric absorption lines within this MIR spectral range; indeed, the optical path is more than 1 meter in air between the laser and the device under measurement. In contrast, a smooth spectral can be seen within the second MIR atmospheric transparency window (above 8 µm wavelength).

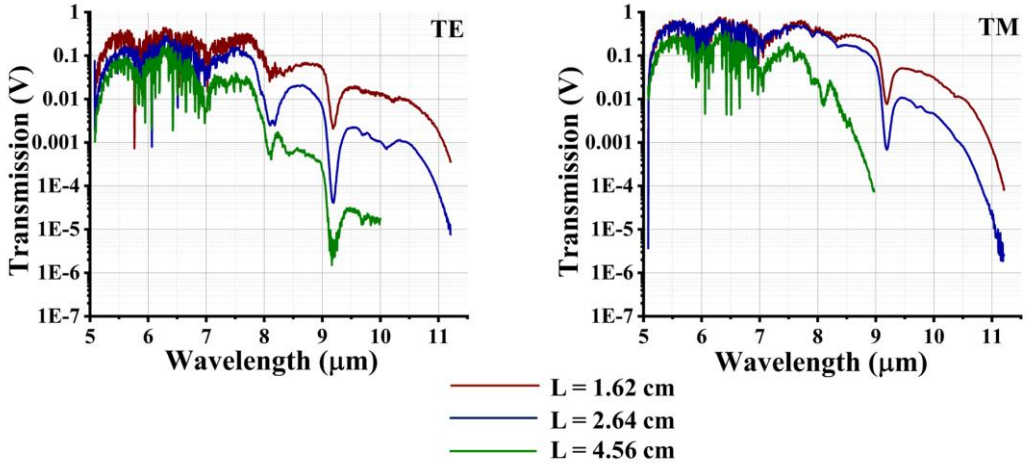

Fig.2.6. Optical transmission spectra of the spiral waveguide with different spiral lengths as a function of wavelength for TE- and TM-polarization.

Then, the cut-back method has been used to determine the propagation losses of the waveguide for both polarization measurements from 5 to 11 µm wavelength. A propagation loss (in dB/cm) can be calculated by a linear regression of the optical transmission as a function of the waveguide propagating length at each wavelength. After that, a Savitzky-Golay (savgol) filter is applied to the measurement to smooth the spectrum oscillations due to the fact that the Savitzky-Golay seeks to preserve the shapes of peaks, so it is a good choice for removing the background noise. The results of the propagation losses with the 3rd polynomial order smooth and scanning over the 10-sampling point window (45 nm wavelength span) are depicted in Fig.2.7.

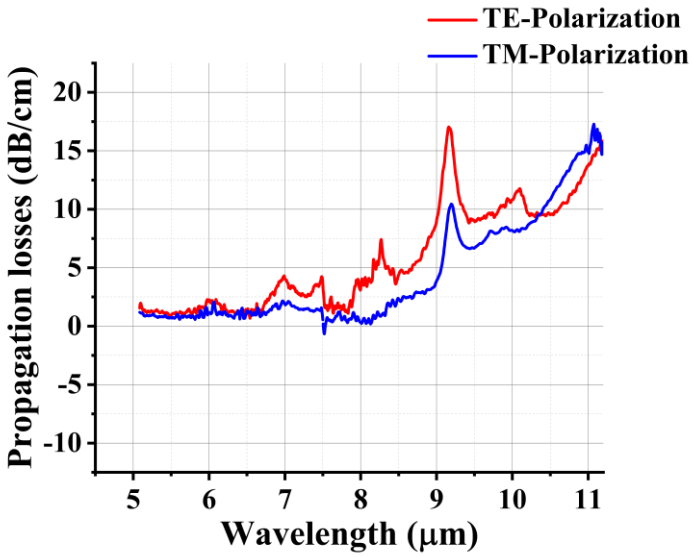

Fig.2.7. Propagation losses as a function of the wavelength for TE and TM polarizations after smoothing the fitting by a Savitzky-Golay method. The optical losses below 3 dB/cm up to 9 μm wavelength have been obtained for TM polarization, which is compatible with QCL integration.

As shown, the propagation losses for TE polarization are slightly higher than the propagation losses for TM polarization. However, both appear to have the same tendency. Broadband low-loss performance is achieved until around 8 μm wavelength. An increase of the loss larger than 8.5 μm can be seen in TE/TM polarization, which is caused by the Si doped-substrate absorption. In fact, Si shows intrinsic multiphonon absorption at a wavelength that is longer than 7.5 μm [98]. In this sense, numerical simulations of the optical mode profile are performed by using the mode-solver to identify the optical mode overlap with the Si substrate. Then, the free-carrier absorption due to the highly doped substrate will be obtained by multiplying the power fraction of the overlap by the absorption coefficient caused by the free-carrier in the Si substrate with the doping electron concentration of 2×10^{19} cm^{-3} [99]. As depicted in Fig.2.8., we have observed the optical mode expanding towards the bottom Si substrate at longer wavelengths. This expansion is causing an increase in propagation losses due to Si multiphonon absorption occurring at these longer wavelengths.

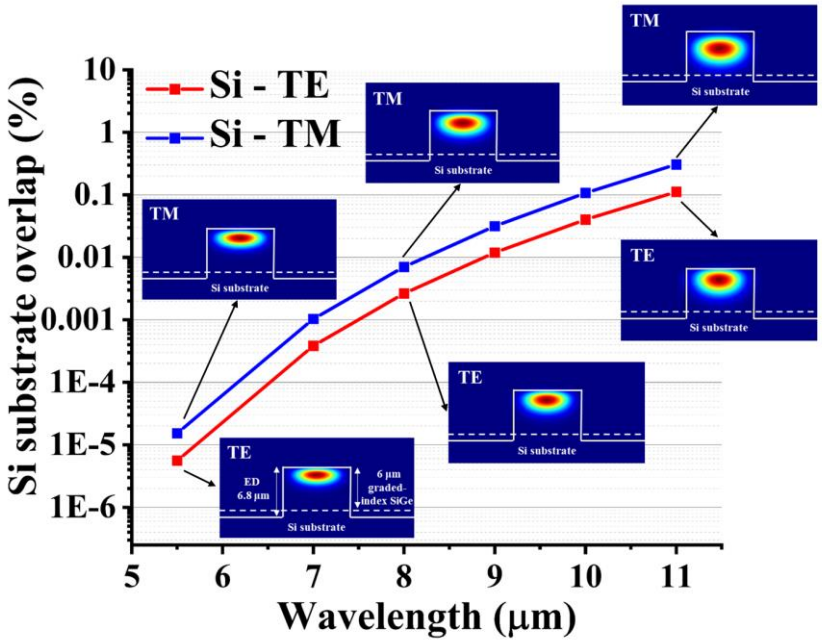

Fig.2.8. Optical mode overlaps of the Si substrate as a function of the wavelength for TE- and TM-polarizations of a 6-µm width and 6.8-µm of etching depth.

In addition, an increase of the propagation loss larger than 10 dB/cm is observed for both TE and TM polarization at 9.2 µm, which is coming from the oxygen impurities during the epitaxial growth [100]. In general, the interstitial oxygen in Si induces the Si-O bond within the lattice, which results in an absorption peak centered at 9.04 µm wavelength [101]. However, the oxygen impurities in SiGe alloy have been shifted towards longer wavelengths. This shift is possibly due to the alteration of the Si-Si bonds within the SiGe lattice [102]. Hence, the rise in propagation losses at a wavelength of approximately 9.2 µm is attributed to the presence of oxygen impurities introduced during the epitaxial growth of the SiGe alloy. This value can thus be expected to improve in the future by developing the epitaxial growth process of the SiGe-alloy layers, such as placing a specific gas filter in the LEPECVD equipment during the growth process.

It can then be concluded that in terms of optical properties, it is possible to use SiGe waveguides grown on a doped substrate for QCL integration below 9 µm wavelength, as propagation losses remain compatible with many optical functions on-chip.

2.1.2 Electrical Characterization

Given that the primary aim of the SiGe-graded platform is its utilization in QCL integration, the second aspect of this investigation involves analyzing the electrical properties to confirm the passage of current through the structure. It was thus decided to test the electrical properties of structures made of a bottom contact on a doped Si substrate and a top contact on top of the SiGe growth, to be able to measure the corresponding resistance. A schematic view of the structure for a bottom contact test is depicted in Fig.2.9(a). Also, the final device of the QCL on top of the SiGe platform can be seen in Fig.2.9(b). For the test of the access resistance, the etching depth is targeted to be around 6 µm. However, for the final device, the etching depth of the SiGe-graded index has to be optimized depending on the application.

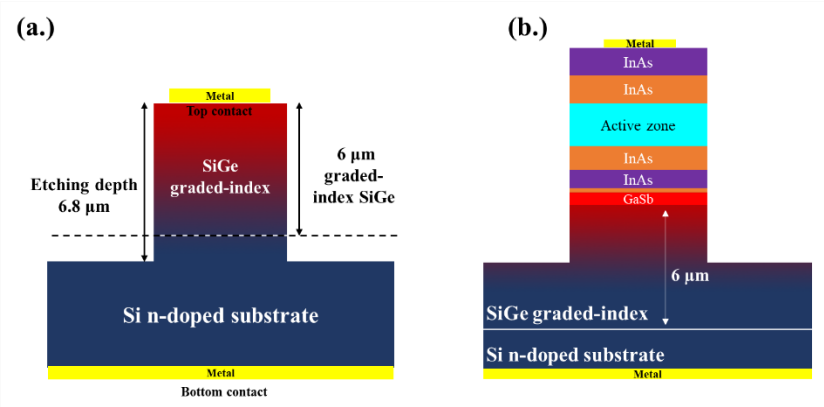

Fig.2.9. The schematic cut-view indicated the metal stack of (a.) the device for the bottom contact experiment and (b.) the final device for QCL on top of the SiGe platform.

In this regard, I have fabricated and characterized squared mesa diodes with sizes ranging from 60 to 150 µm side lengths. The fabrication process step of the mesa structures is illustrated in Fig.2.10. The fabrication now requires two lithography steps to define the mesa structure.

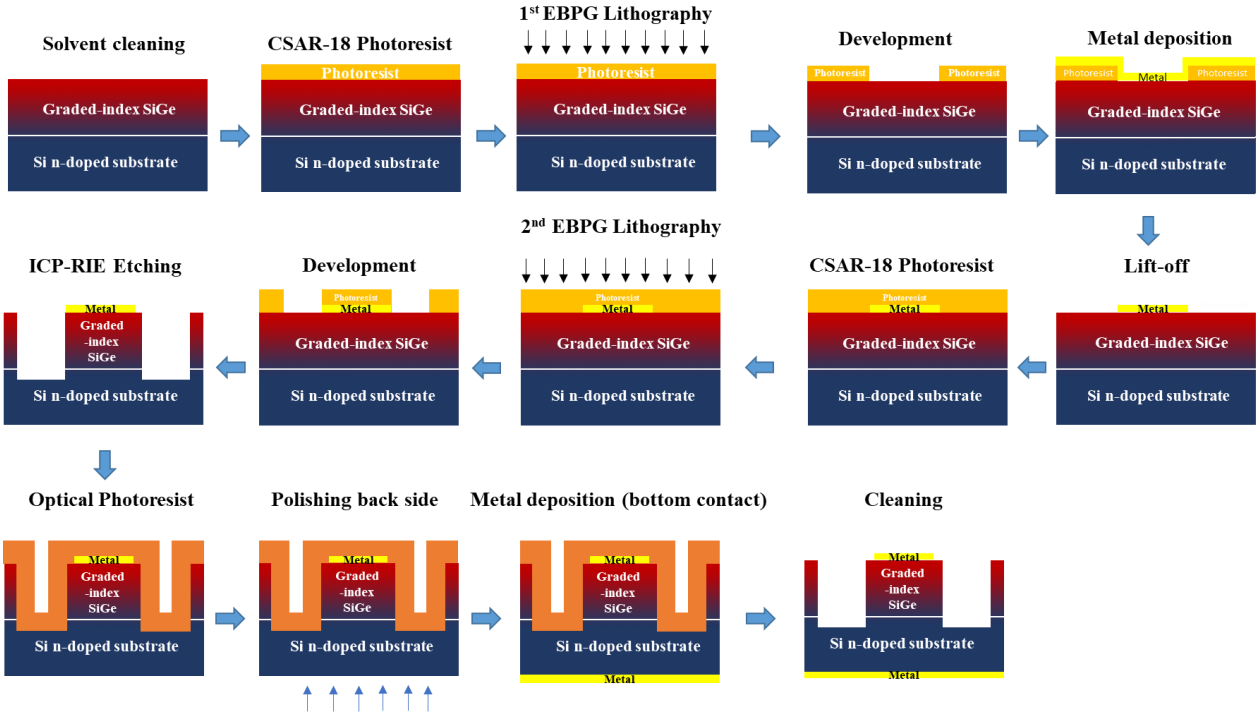

Fig.2.10. Schematics illustrate the general fabrication process flow of mesa structures, indicating 2-step lithography.

In detail, a sample piece of around 2×2 cm^2 is prepared using the same technique as discussed in section 2.2.1. The squared mesas with different sizes, from 60 to 150 µm side length, are patterned by the 1st step of electron beam lithography (EBPG). The exposed area after the lithography is removed by a developer, ZED-N50, followed by 30 seconds of IPA. Metallic layers containing 10 nm of Titanium (Ti) and 300 nm of Gold (Au) are deposited on the sample surface by the E-beam evaporation technique (Plassys Modele MEB 550s), followed by 2-butanol for the lift-off process. Another spin coating using "CSAR.18" is operated again with the same parameters. Then the 2nd E-Beam lithography, development, and an ICP etching (ICP-DRIE SPTS) process are performed. The fabricated structure is protected by a thick optical photoresist, "AZ-4562," before performing the backside contact. The bottom of the sample is polished to enable a uniform surface. Then, a similar metal stack (10 nm of Ti and 300 nm of Au) is deposited on the whole surface of the backside to form the bottom ohmic contact. Before characterization, all the photoresists are cleaned with a standard solvent. An optical microscope image of the fabricated squared mesa with 70 and 150 µm side lengths is shown in Fig.2.11.

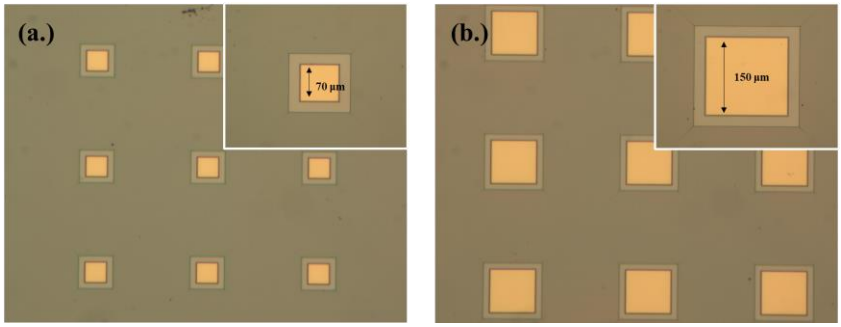

Fig.2.11. Optical microscope image of fabricated squared mesas with (a) 70 µm side length and (b) 150 µm side length, along with the zoomed image of a single mesa structure.

In terms of measurement, the mesa device is characterized by using a pair of tip probe electrodes placed on the sample's top and bottom metal contacts. A power source (Keithley-2400) has been used to apply the voltage into the diode, and then the injected current value required to achieve that voltage is obtained. The injected current is measured as a function of applied voltage (I-V characteristic) and shown in Fig.2.12(a.). Rectifying behavior has been obtained in all devices, which was not expected at the beginning. Interestingly this indicates that a diode has been obtained. Considering that the bottom contact is on a highly doped substrate, it means that a depletion region is formed at the top of the waveguide, so the top contact presents a Schottky behavior while the bottom contact on a highly *N+* doped substrate is ohmic. The ideality of the diode and the Schottky barrier can be estimated from the measurement. The procedure is described below.

Based on the literature [103, 104], the I-V characteristic of the Schottky diode can be approximated by:

$$I = I_s\left[exp\left(\frac{\beta V_D}{n}\right) - 1\right] \approx I_s exp\left(\beta\frac{V_D}{n}\right), \text{ if } \beta\frac{V_D}{n} \gg 1 \qquad (2.2)$$

where n is the dimensionless parameter stands for ideality factor of the diode, in the case of ideal diode $n = 1$, V_D is the voltage across the diode, which is related to the applied voltage in the system through the relation: $V_D = V - IR$, where R defines as series resistance of the diode, and β is a constant, which is in the relation of the electron charge (q), the Boltzmann constant (k), and the absolute temperature (T), $\beta = \frac{q}{kT} = 38\ V^{-1}$.

and the saturation current (I_s) can be written as:

$$I_s = AA^*T^2 exp(-\beta\phi_{B0}) = I_0 exp(-\beta\phi_{B0}) \quad (2.3)$$

where A is the contact area, A^* is the Richardson constant of 120×0.12 A/(cm^{2}K^2), and ϕ_{B0} is the Schottky barrier height.

Substitution the relation of the applied voltage to Eq.2.2, and under the assumption that $V_D \approx V$, which is true for the small values of current gives:

$$I = I_s exp\left(\beta \frac{V}{n}\right), \text{ if } \beta \frac{V}{n} \gg 1 \quad (2.4)$$

Then, Eq.2.4 can be rewritten as:

$$ln(I) = ln(I_s) + \beta \frac{V}{n} \quad (2.5)$$

So, the Schottky barrier of the diode and its ideality factor can be found by plotting $ln(I)\ versus\ V$ and by evaluating the intersection of the curve with the origin (V = 0) and by the evaluating the slope of the curve for low values of V respectively. From our measurement, a Schottky barrier of 0.58 eV can be extracted, with a diode ideality factor around 1.43.

Furthermore, at large values of the current, the derivative of the voltage with respect to the injected current has been calculated to estimate the access resistance R. The results of equivalent mesas diode (70 – 100 µm side length) are plotted in Fig.2.12(b). A resistance around 2.7 – 3.2 Ω can be extracted from the complete structure of graded SiGe on top of the $N+$ doped Si substrate. Moreover, the resistivity between bottom contact and Schottky barrier is deduced from the measurement, resulting from 0.2 to 0.48 Ω·cm. Assuming that the resistivity is around 0.2 to 0.5 Ω·cm, the access resistance from the SiGe waveguide of the final device would be around 0.4 to 1 Ω, which is compatible with the application.

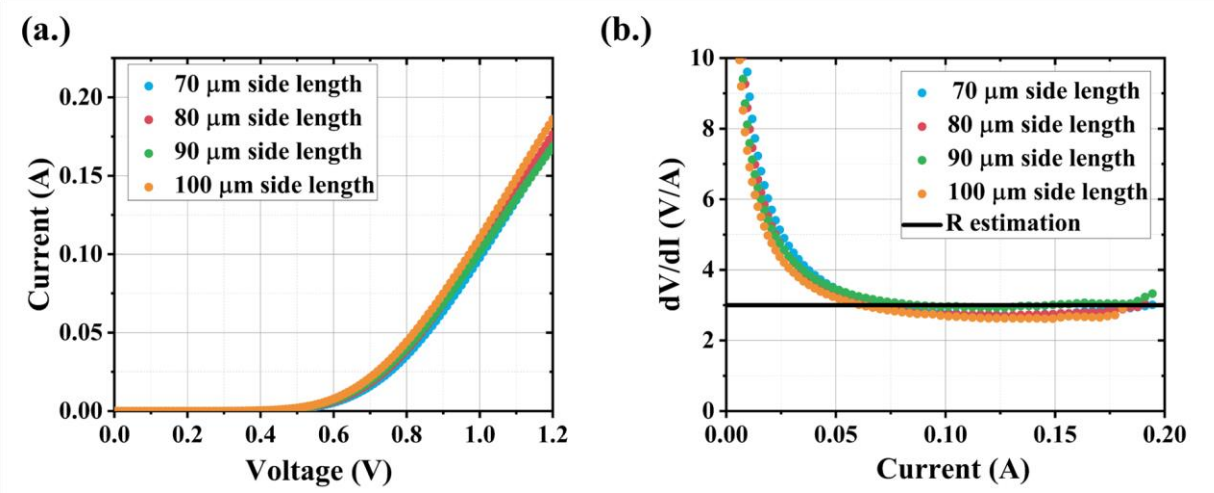

Fig.2.12. (a.) Measured current intensity as a function of the applied voltage in squared mesas with different side lengths of 70, 80, 90, and 100 µm. (b) Measured voltage derivative with respect to the current intensity for different diode mesas. A horizontal solid line represents a 3 Ω resistivity value.

To confirm the result of the Schottky behavior, the arsenic (n-type), phosphorus (n-type), and boron (p-type) concentrations within the graded-index platform were conducted through Secondary Ion Mass Spectrometry (SIMS) analysis, which was carried out by an external company (Eurofins Scientific). The results can be observed in Fig.2.13. Since the values of the dopant concentration that have been measured are dependent on the SiGe alloy by ratio, which has gradually been modified along the depth of the platform, these results tend to have a certain incertitude. Despite that, a low residual n-type doping density estimation (10^{15}–10^{16} cm^{-3}) is associated with the graded-index SiGe layer. This estimation is deduced by evaluating the concentration values illustrated in the figure, while accounting for the p-type contribution (B) subtracted from the n-type concentrations (P and As). It can be clearly seen that the Arsenic (As) dopant (depicted in green color) is the major dopant in the platform and the elevated As concentration within the 6 µm-thick SiGe layer is attributed from the diffusion from the highly-doped Si substrate during the epitaxial growth (As concentration in the Si substate is 2×10^{19} cm^{-3}).

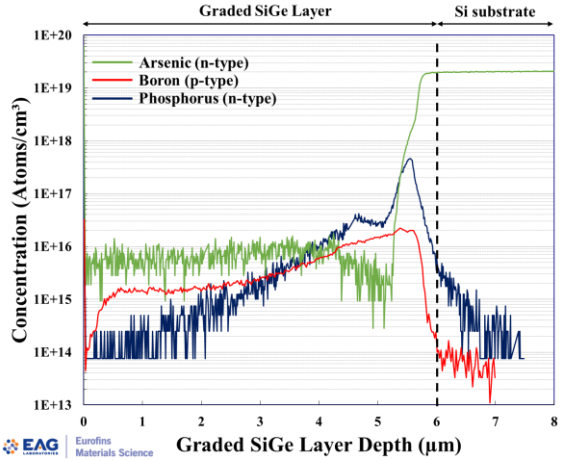

Fig.2.13. SIMS analysis of the SiGe graded index platform on a highly n-doped Si substrate showing the concentration profiles of boron (red), phosphorus (dark blue), and arsenic (green) along the vertical z-axis. Here, the reference point zero corresponds to the top surface of the 6 µm-thick graded-index SiGe platform.

As a conclusion, this study allows: (i) to confirm that small access resistance can be obtained for future integration of QCL on top of SiGe grown on doped-Si substrate. It is important to note that in the final device, there will not be any Schottky contact, as the top contact will be taken on top of doped InAs, (ii) to show the possibility to obtain a Schottky diode on SiGe waveguide. These results paved the way for the first integrated modulators that have then been demonstrated in the group by M. Montesinos [105, 106] and continued further by T. H. N. Nguyen. I will report the main conclusions hereafter.

2.1.3 Integrated Electro-Optical Modulator (EOM) in the Mid-IR

Following the demonstration of low propagation losses in the mid-IR of SiGe graded index on the highly doped Si substrate and the possibility to obtain Schottky diodes embedded within this platform, the experimental investigation of integrated Electro-Optic Modulator (EOM) operating in a wide MIR spectral range has been done. As a matter of fact, the integration of EOM has demonstrated significant potential for enhancing multi-molecule detection within spectroscopic systems. Hence, the development of integrated EOM operating in the mid-IR would pave the way for implementing an on-chip sensor. In this regard, my colleague, M. Montesinos (former Ph.D. student at C2N), had gone through designing, fabricating, and characterizing the EOM based on the free-carrier plasma dispersion (FCPD) effect in the long-wave infrared range by using the Ge-rich graded-index SiGe platform. The same technique as

the one I developed to fabricate the mesa squared has been used to fabricate the EOM device. The EOM has been characterized in two different regimes: injection regime and depletion regime. The results of the normalized optical transmission as a function of the measured current for both injection and depletion regimes are presented in Fig.2.14. Interestingly, a maximum variation of an absorption modulation of 1.3 dB is obtained at 10.7 µm wavelength in the injection regime for a current of 170 mA, which is, in that time, the largest electro-optical modulation reported in the wavelength longer than 8 µm. In the case of the depletion regime (negative voltage), the transmission increases as the reverse bias increases. A maximum variation of 0.4 dB is obtained at -8 V applied to the EOM structure. His research has paved the way for demonstrating the EOM's device in the LWIR spectrum working in both rejection and depletion regime.

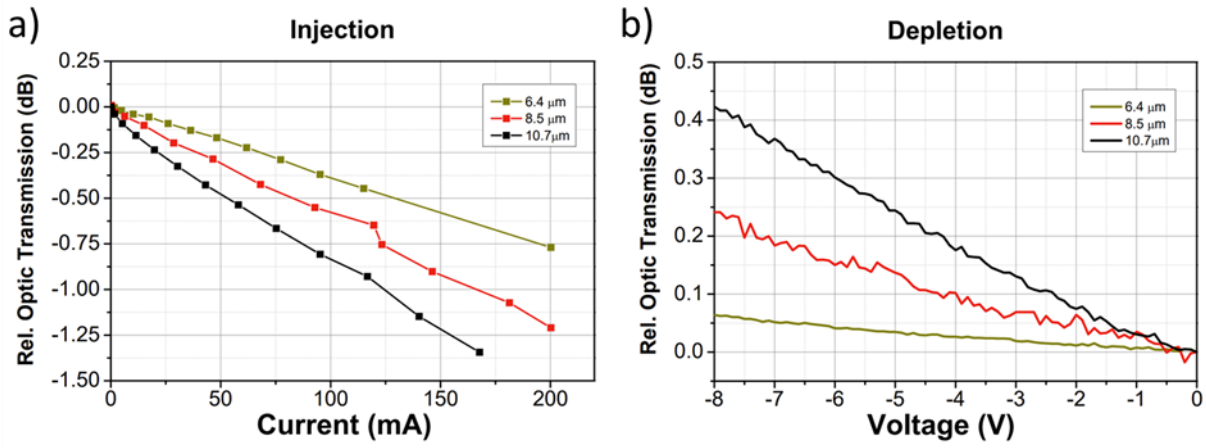

Fig.2.14. Static Electro-optical modulator transmission relative to zero bias voltage as a function of (a.) injected current to a diode and (b) applied voltage in depletion configuration, the image was taken from Ref [106].

Afterward, T. H. N. Nguyen (currently Ph.D. student at C2N) has been continuing to develop the EOM in the long-wave infrared range. Interestingly, an improvement of the wideband integrated electro-optical modulator has been reaching the operation up to 1 GHz frequency [107, 108]. The electro-optical modulator characterizations in the depletion regime of static and dynamic characteristic are illustrated in Fig.2.15. The high-speed operation has been investigated, and the electro-optical modulation measured up to 1 GHz is experimentally demonstrated where a signal to noise ratio larger than 10 dB is still obtained. These results open the road towards the use of EOM in fully integrated systems in the mid-IR spectral ranges.

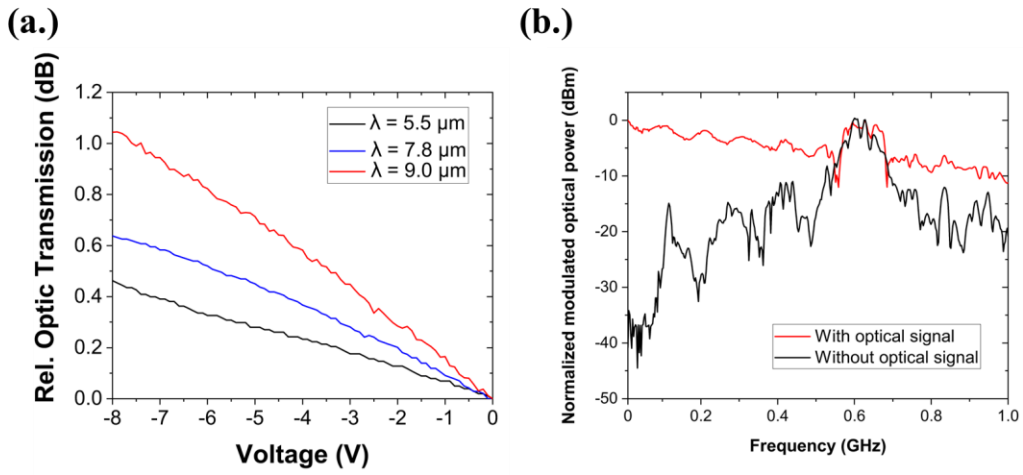

Fig.2.15. EOM characterization in the depletion regime: (a.) variation of the normalized optical transmission as a function of the applied voltage in the DC regime demonstrated from 5.5 to 9 µm wavelength and (b.) amplitude of the photo-detected signal as a function of the applied voltage RF frequency in the dynamic regime. The image was taken from Ref [107].

2.2 ETCHING OF THE BRAGG STRUCTURE

Apart from the establishment of the electrical properties in the SiGe-graded index platform, the development of a monolithically integrated QCL on SiGe platform requires the fabrication of an optical cavity. The cavity is defined by two optical mirrors made by the Bragg grating corrugated waveguides. The main challenge in terms of fabrication is related to the required etching depth and aspect ratio of the etching that is required. Indeed, to achieve efficient coupling between the two waveguides, it is required that the corrugation overlaps with both the SiGe waveguide and the III-V active waveguide. When considering the III-V stack with the doped region, as can be seen in Fig.2.1(b.), a total thickness of more than 9 µm is obtained. This indicates that the corrugated structure depth is more than 10 µm, while the corrugation period is around 1.5 µm as has been shown in the end of chapter 1. This is a main challenge in terms of etching selectivity between the resist and the different materials to be etched. A fabrication process of SiGe photonics circuits is known in our research group, and the epitaxial growth of AlSb/InAs QCL in SiGe photonics circuits is under development at IES and Politecnico di Milano. My priority was then on the advancement of cleanroom techniques for the dry etching of III-V materials which will serve as a light source based on the InAs/AlSb material. I started this development first on a bulk InAs sample and then on an AlSb/InAs QCL sample provided by IES. Unfortunately, the growth of AlSb/InAs QCL on top of SiGe

photonics circuits is still facing challenges related with antiphase boundaries (APB), so integrated QCL has not been fabricated. However, the fabrication steps that I developed, detailed hereafter, will be useful when the material growth challenges are solved by our partners.

The main etching process that will be presented will thus mainly focus on the dry etching process to optimize the optimal recipes, focusing on the obtaining of sidewall verticality, surface smoothness, and flat bottom in the etched profile.

2.2.1 Dry Etching of InAs Bulk Materials

During the first year of my Ph.D. thesis, my main concern was the development of the dry etching process, which will be used in fabricating the real device at the end. This work has been done in close collaboration with cleanroom engineers. It's worth mentioning that processing III-V material is not within the usual scope of our research group since our primary focus revolves around silicon-based technology. However, a significant amount of research on III-V materials has been conducted within Adel's group, so we have adopted the initial sample processing steps from their work. In this work, the QCL material will be supplied by our collaborative partner, the Institut d'Electronique et des Systèmes (IES), Université de Montpellier. Hence, in the preliminary phases of the work it has been proposed to use bulk InAs material as it corresponds to the main material of the future QCL stack. The primary goal of the initial test is to identify a robust mask for the etching process and achieving the optimal process flow. Fig.2.16. presents the general process flow, followed by a detailed exposition of the specific fabrication processes that I developed within the cleanroom facilities.

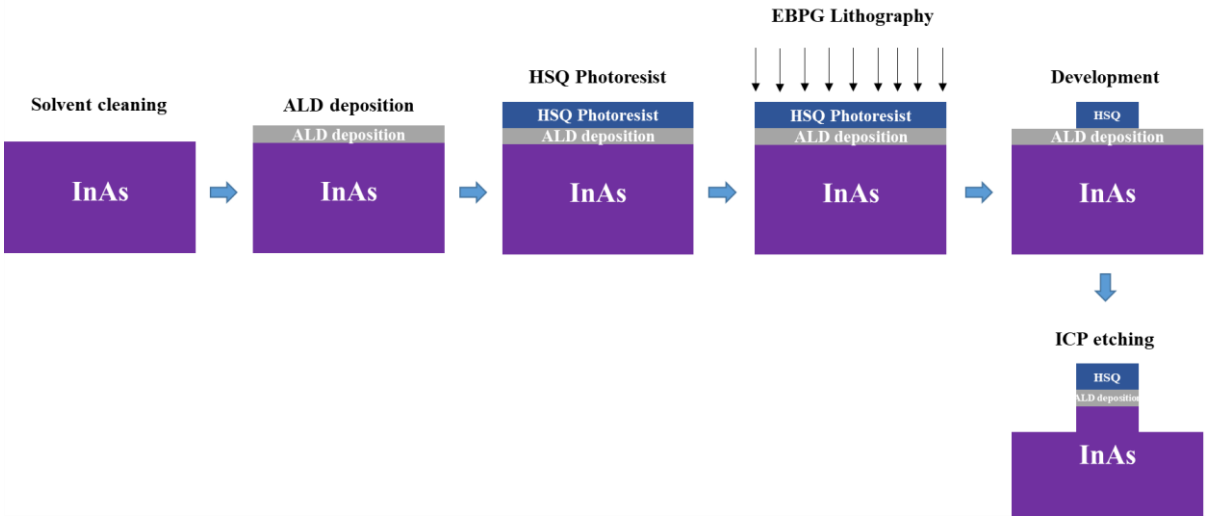

Fig.2.16. Schematic of the general fabrication process flow of InAs bulk materials.

Due to the relatively small size of the InAs bulk wafers, it was necessary to reduce the dimensions of the working sample to 1×1 cm² instead of the usual 2×2 cm² size for SiGe platform. The sample surface is cleaned for 5 minutes in an acetone bath and another 5 minutes in isopropanol. Oxygen plasma has been performed to clean the sample surface for 10 minutes. Then, to ensure the proper cleaning, hydrochloric acid (HCl) has been used in a mixed solution (20% of HCl and H_2O). It is important to mention that the HCl solution has the capability to etch InAs material, which emphasizes the need to carefully manage the cleaning process duration to ensure rapid surface cleaning. Then, atomic layer deposition (ALD) deposition has been carried out to deposit a 5 nm-thin film of SiO_2. The thin SiO_2 film will serve to enhance the adhesion between the surface and the photoresist. Next, the negative photoresist, "HSQ: Fox-15," has been selected to be a resist before the electron beam lithography (EBPG). The thickness of the photoresist is required to be larger than 600 nm. Therefore, spin coating of HSQ is done at 1500 rpm for 1 minute, which provides a resist deposition thickness of approximately 820 nm with good uniformity. Then, a post-bake at 90 °C for 1 hour is performed. After that, electron beam lithography has been performed. In this regard, I have calibrated the minimal dose to achieve the optimal resist profile for the E-beam lithography step when fixing the current during the lithography process to be 100nA since the HSQ required different doses from the SiGe material. The initial hypothesis is that the high doses will result in high contrast. So, the minimal doses have been set to vary from 2500 to 6950 μC/cm^2 with the increasing step size of 50 μC/cm^2 from one waveguide to the other. The development of AZ400K and H_2O in a ratio of $^1/_4 : ^3/_4$ has been done for 2.30 minutes, followed by 3 minutes in the water after the EBPG. The observation under the SEM has been done to monitor the profile of the waveguide after the EBPG and the development. The results of different doses are indicated in Fig.2.17. The resist profile is clearly improved when the dose is decreased.

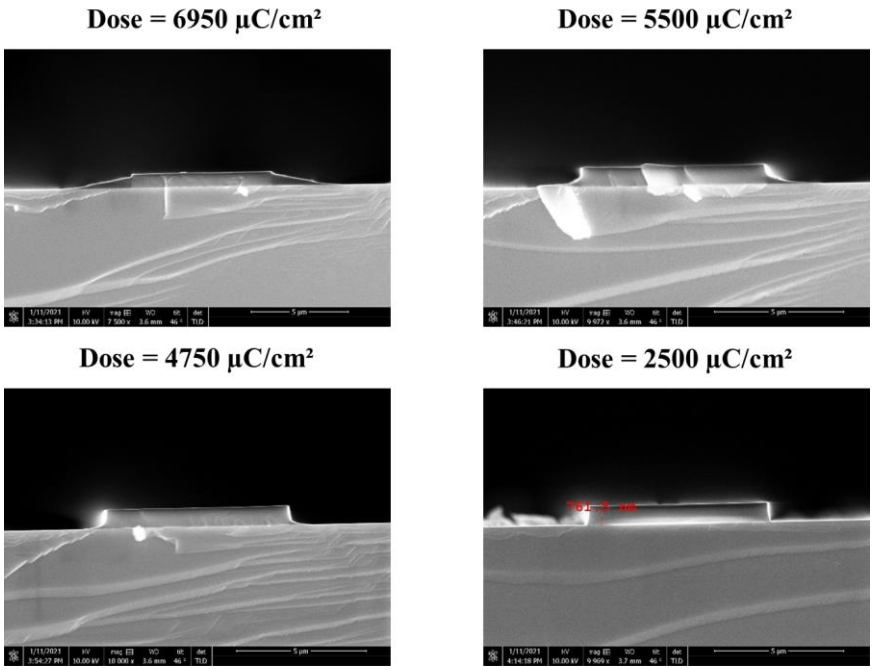

Fig.2.17. SEM profile images of InAs bulk material after the electron beam lithography, followed by the development. The lowest dose has been shown as the best profile.

Then, the sample has been cleaved to separate into 2 small parts. The first sample has then been etched employing the Sentech I machine (ICP-RIE SENTECH SI500) under the supervision of L. Ferlazzo. The etching has been carried out by the combination of 2 gasses of HBr and O_2 for 5 minutes at the working pressure of 1.5 mTorr, thus expecting to achieve an etching depth of 3 µm. In this etching configuration, the HBr gas will serve as the etching gas, with the addition of O_2 to facilitate the formation of SiOBr passivation. This passivation serves to inhibit sidewall under-etching and enable the creation of patterns with highly anisotropic profiles [109]. Additionally, the etching substrate has been set to be at 150 °C for the desorption of the etching products formed, that are non-volatile at room temperature. The profile after etching of the lowest dose is represented in Fig.2.18.

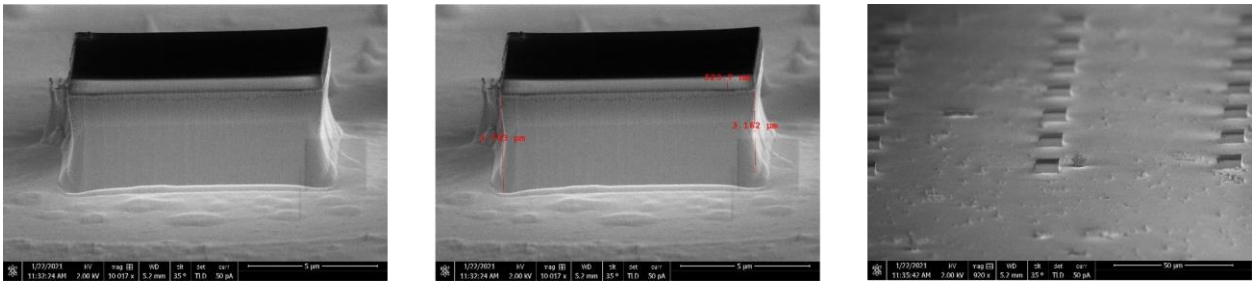

Fig.2.18. SEM profile images of the InAs with the ALD layer and the top remaining photoresist after etching by HBr and O_2 for 5 minutes using Sentech I machine.

An etching depth of around 3 µm has been obtained as expected. Sufficient selectivity between photoresist and InAs surface is achieved. Nevertheless, enhancements are required in terms of isotropy and surface roughness of the bottom layer. For better comprehension, another piece of the sample was processed. As the ALD layer has created an etching delay and then non-uniformity during the ICP etching, the addition of an RIE etching step has been proposed before the ICP etching. The fluorine reactive ion etching (NEXTRAL RIE SF_6 NE100 63) so-called RIE etching is then required for 30 seconds to etch first the 25 nm of SiO_2 mask to remove the ALD layer, leading to the improvement of the ICP etching in followed. Then, the etching process of ICP is employed. The observation of the profile after the 2nd etching step is shown in Fig.2.19. The image reveals that while the ALD layer has been eliminated, favorable adhesion between the resist and InAs surface is maintained. However, further improvement is necessary regarding the surface roughness.

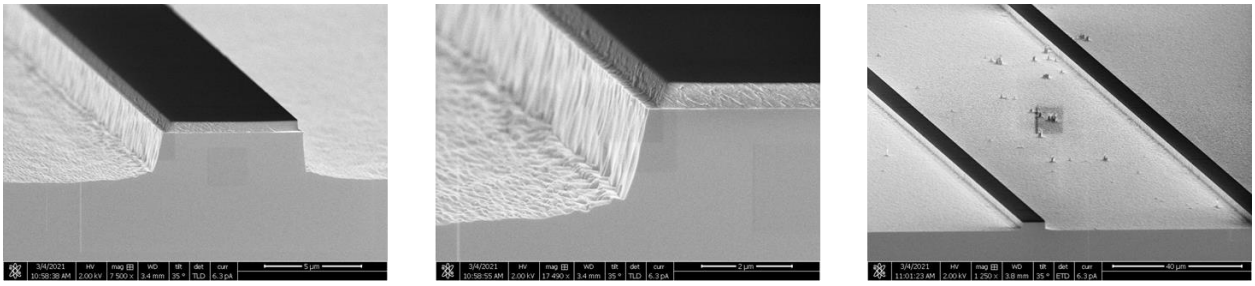

Fig.2.19. SEM profile images of the InAs without the ALD layer and the top remaining photoresist after 2 etching steps.

Then, the comparison between two samples has been taken into consideration, one sample with ALD deposition and the other without. The observation under the optical microscope of the 2 samples is depicted in Fig.2.20. The comparison reveals a noticeable difference in surface

quality between the sample with and without the ALD layer. However, it's worth noting that the RIE etching process led to some surface contamination with NH_4. This issue could potentially be mitigated through the implementation of a plasma O_2 cleaning step prior to the ICP etching process.

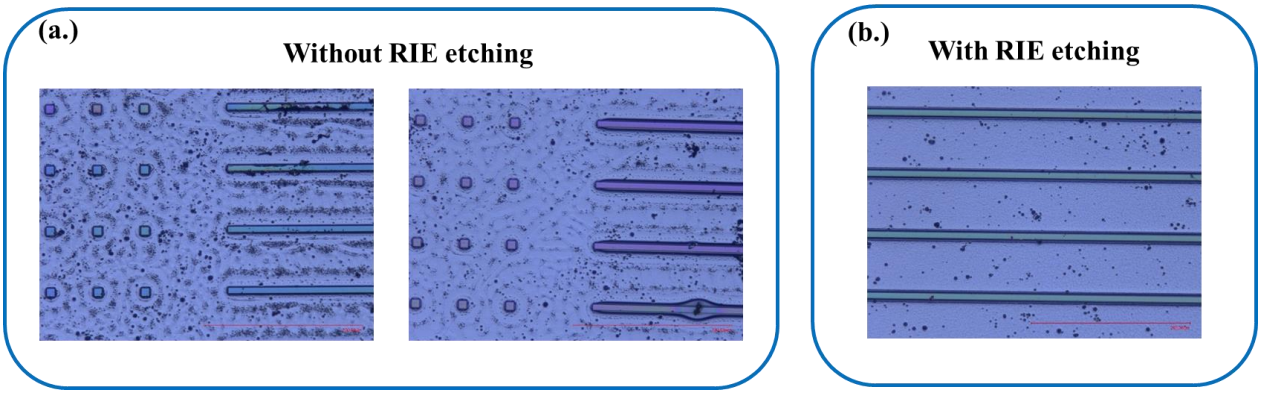

Fig.2.20. The surface observation under the optical microscope after the ICP etching process for (a.) the sample without the RIE etching, and (b.) the sample with the RIE etching.

2.2.2 Dry Etching of an AlSb/InAs Stack

Subsequent to the preliminary investigation of the optimal process for fabricating InAs bulk material, we have received an AlSb/InAs stack from IES, close to the one used for QCL development. The stack is comprised, in sequential order from the top, of 2 µm of doped InAs, followed by 3.5 µm of undoped InAs, before attacking multilayers. The multilayer structure consists of AlSb/InAs. The summary of the material stack can be seen in Fig.2.21.

	Material	Thickness (µm)	
Cladding	InAs n-doped 7.10^{17} cm^{-3}	2	5.5 µm on top of AlSb/InAs multi-stack
Spacer	InAs	3.5	
Active region AlSb/InAs			
Spacer	InAs	3.5	
Cladding	InAs n-doped 7.10^{17} cm^{-3}	2	
Substrate	InAs		

Fig.2.21. The QCL stack shows the growth material and its thickness.

It should be noted that while this structure may not precisely be like the final configuration of the monolithic integration, it does provide us with insights into the processing of QCL

materials. Upon receiving the material, a similar procedure for preparing the InAs material was employed. To ensure uniform and consistent photoresist coverage across the entire surface, the cleaning and spin coating processes were extended to cover the entire wafer. To increase the thickness of the photoresist layer on the surface, the spin coating speed was adjusted to 1250 rpm instead of 1500 rpm. Notably, the successful outcome of the previous test without the ALD layer on the InAs demonstrated promising results. Consequently, the wafer was processed without the ALD deposition. After spin coating, the sample of 1×1 cm² has been manually cleaved from the wafer with a photoresist on top. The waveguide with the corrugation is then patterned on the E-beam lithography step with tuning doses from 2300 to 2500 μC/cm^2. Development with the same process as the one described for InAs is then done after the lithography. Then, the sample was observed under the SEM to see the waveguide profile after the lithography and development. The SEM images are shown in Fig.2.22.

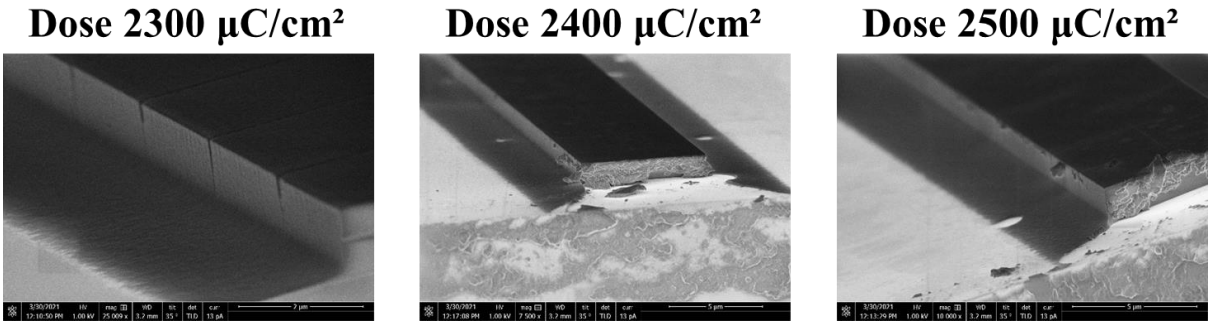

Fig.2.22. The observation under the SEM shows the profile images of the waveguide indicating the different doses of 2300, 2400, and 2500 μC/cm^2. The mask tail can be observed next to the waveguide.

The SEM images display that the current state of the waveguide exhibits a mask tail, which can be attributed to the proximity effect resulting from the presence of a thick photoresist layer. The proximity effects existing now are different between InAs and the AlSb/InAs multistack sample. Additionally, it is noteworthy that the extent of this tail decreases as the dose is increased. The presence of this mask tail can be mitigated by utilizing the SPTS etching machine (ICP-DRIE SPTS) to etch the sample for 50 seconds in order to decrease a bit the photoresist's thickness. In addition to the mask tail that becomes evident after development, an additional stitching error has been identified on the sample's surface. An illustration of the waveguide's profile, observed under the SEM and depicting the stitching error, is provided in Fig.2.23.

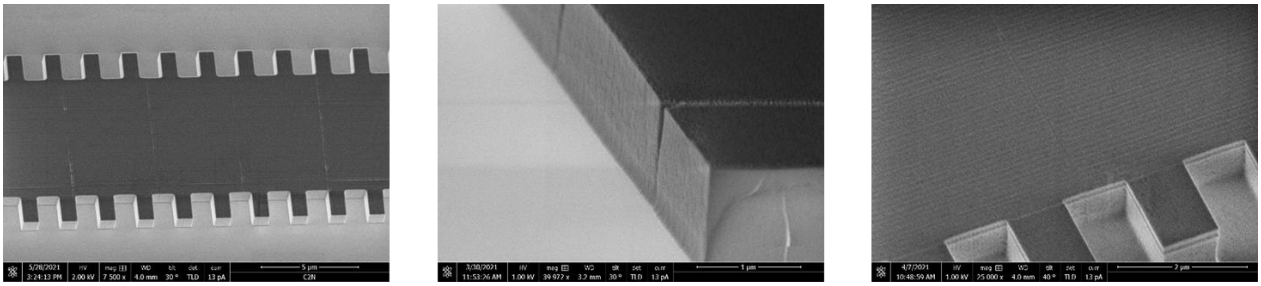

Fig.2.23. The observation under the SEM shows the profile images with the stitching error that happens during electron beam lithography where misalignment or inconsistencies occur in the pattern placement.

Hence, a range of strategies was explored to avoid the stitching errors. Parameters during the E-beam lithography were adjusted, for example, by modifying the current resolution, reducing subfield setting size, and altering field overlap during the electron beam writing process. Nonetheless, this stitching error has no impact on the waveguide profile after etching. Therefore, this issue is currently not our primary focus. Then, one part of the sample has been further etched by ICP etching (HBr and O_2 gases) with the same parameters as the InAs etching process with increasing duration time during the etching, expecting deeper etching depth. The time has been increased to 15 minutes to obtain 9 µm depth; the etching rate is approximately 0.6 µm/minute.

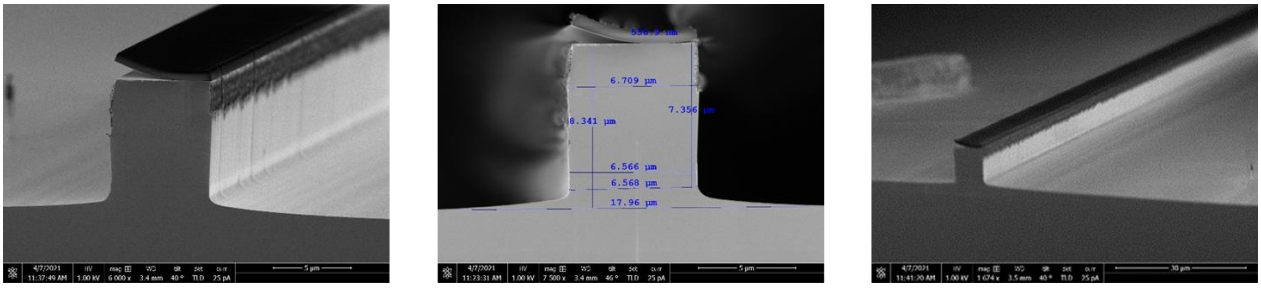

Fig.2.24. The observation under the SEM shows the profile images of the waveguide after 15 minutes of ICP-RIE etching.

A good vertical profile was achieved, spanning nearly 9 µm etching depth as depicted in Fig.2.24. Furthermore, the initial stages of etching the AlSb/InAs multilayers proceeded with no complications. However, the main concern emerged regarding resist adhesion; extended etching times resulted in photoresist detachment. Addressing this issue, the adhesion could be enhanced by reintroducing a 5 nm SiO_2 layer through ALD deposition. In this context, another

piece of the wafer has been cleaved and cleaned by HF acid cleaning for the purpose of preparing the sample surface for ALD deposition. The ALD deposition was performed prior to the photoresist spin coating. Subsequently, the lithography process was executed, followed by the development step. The sample has then been etched by the ICP etching for 10 minutes to verify the adhesion of the resist post-etching. SEM images of waveguide profile after 10-minute ICP-RIE etching are shown in Fig.2.25. As can be observed, the optimization of HSQ adhesion was achieved through the incorporation of a thin SiO_2 film. However, an unusual pattern indicating a slope appearing in a single direction was detected, which could hold significance when considering the required corrugations for the coupler. Additionally, the sample was cleaned by HF acid cleaning as a precautionary step, considering the possibility that the anomalous features might be linked to SiO_2 passivation. Nonetheless, these same features persisted, as depicted in Fig.2.25(b.).

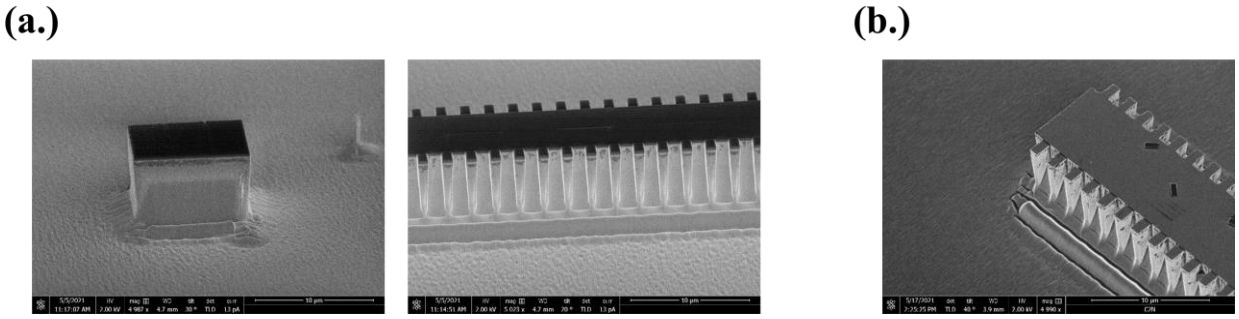

Fig.2.25. (a.) The observation under the SEM shows the profile images of the waveguide after 10 minutes of ICP-RIE etching. Good adhesion has been observed with the plane revelation. (b.) The observation under the SEM shows the profile images of the waveguide after ICP-RIE etching and HF acid cleaning. The same feature of the plane revelation in one direction can still be seen.

To understand the etching behavior of the AlSb/InAs multilayers during the etching process, an additional test involving parameter modification within the etching machine has been operated. The major controllable parameters in the etching contain the ICP power, temperature, chamber pressure, and gas flow rate. In this regard, 2 parameters have been studied. Firstly, the test has been done by increasing the plasma working pressure to 3 mTorr and etched for 10 minutes. The resulting profile indicated increased isotropy in the waveguide, with the etching rate deviating from the original recipe. Since the working pressure has increased, the scattering and diffusion of ions within the plasma have been increased as well, leading to a sidewall

bombardment. Nonetheless, the distinctive shape feature remained consistent in both directions, as depicted in Fig.2.26.

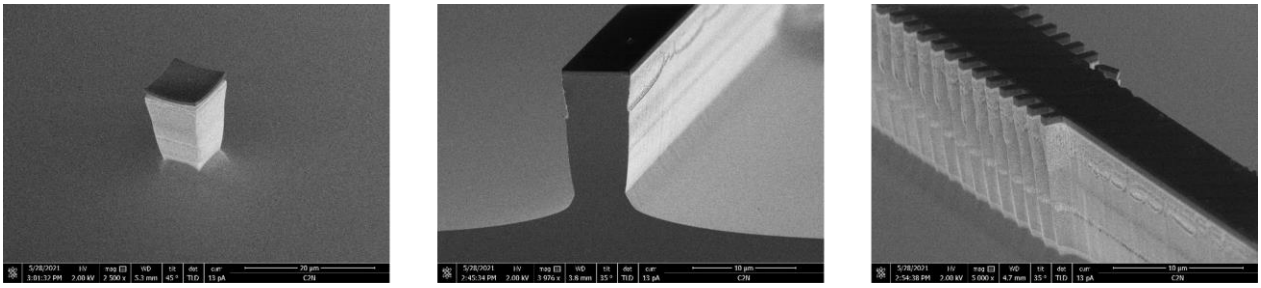

Fig.2.26. The observation under the SEM shows the profile images of too isotropy waveguide after increasing the pressure during the etching process.

Another test has been carried out by increasing the ICP RF power to 1000 Watts, a deviation from the original 800 Watts, and then etched for 10 minutes. While the ICP power is increased, the number of ions created inside the chamber will also be increased, which will increase the chemical etch rate during the process [110]. The results after etching observing under the SEM can be seen in Fig.2.27. A better anisotropic effect was achieved, yielding a vertical profile appearance. However, it is important to note that the same problem of anisotropy of the etching reappeared despite these adjustments.

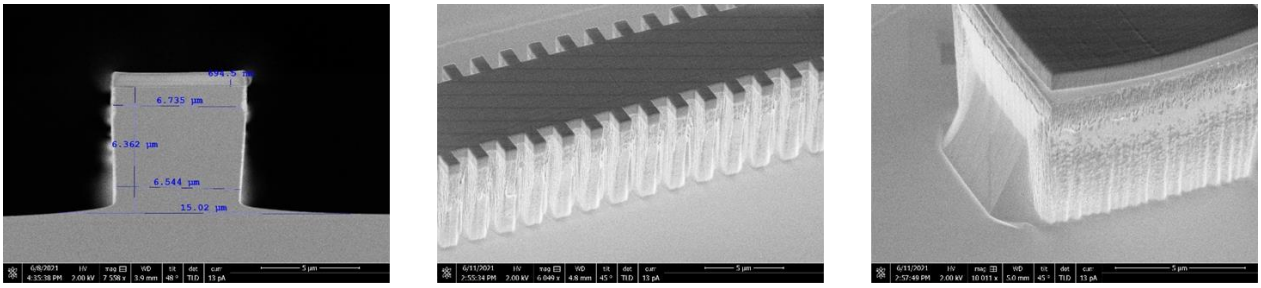

Fig.2.27. The observation under the SEM shows the profile images of the vertical waveguide along with the plane revelation in one direction.

Currently, the primary challenge lies in the occurrence of the “plane revelation” in one direction during the etching process. A leading hypothesis suggests that this phenomenon arises from the crystallographic plane characteristics of the material. It should be noted that one of the concerns has been focused on what might occur when the AlSb/InAs multilayers are etched. In our test, the wafer typically needs a 5.5 µm etching depth before entering the multilayer region but none of our trial runs have been etched so deeply. Even with deeper etching attempts, no

major troubles related to the multilayers have been observed. Hence, there have not been any significant issues reported regarding multilayers from our tests. Moreover, it is essential to underline that this QCL differs from the final QCL material designated for monolithic integration. Further exploration is imperative for the QCL that closely resembles the growth configuration of the device for monolithic integration.

2.3 CONCLUSIONS

In this chapter, the work done towards the fabrication of a monolithically integrated QCL source on top of SiGe waveguide has been presented.

In the first part, the possibility of using SiGe graded index on highly doped Si substrate to exploit backside contact has been demonstrated. This platform has demonstrated its capability for low-loss broadband operation, which holds potential for the development of active photonics devices in the mid-IR. Subsequent investigation has focused on the electrical properties to verify current conduction through the structure using a backside contact. Evident Schottky behavior has been observed, along with the resistance of a few ohms extracted from the measurement. These results led to the first experimental demonstration of an integrated electro-optic modulator operating from 6.4 to 10.7 μm wavelength [105, 106].

Then, the development of fabrication process for etching the Bragg structures, which will be used to form the cavity in the final device, has been investigated. This requires the development of dry etching with large aspect ratio. The development was first done using an InAs bulk wafer to determine the optimal process for III-V fabrication. Following this, an AlSb/InAs stack has been used to test the process on a similar material to the final one. Various parameters have been tuned and optimized. A predominant concern has been shown around the occurrence of plane revelation during the etching process. Further investigation should be centered on examining the impact of the GaSb buffer layer that will be required between SiGe and AlSb/InAs. However, it appeared during the project that the material growth shared between our partner, Université de Montpellier, and Politecnico Di Milano, was more challenging than expected at the beginning of the project, leading to a pause of this aspect of my work for that moment.

3 BUTT-COUPLING OF QUANTUM CASCADE LASER (QCL) TO SIGE PLATFORM ON TWO SEPARATE CHIPS

In response to the difficulties faced during the direct growth of Quantum Cascade Lasers (QCL) on a silicon-germanium (SiGe) platform, the butt coupling of light between two different chips has been investigated. While this option will lose the advantages of integration, we still want to investigate the possibility to couple SiGe photonics circuits with QCL sources in a compact way. As a perspective of this work, both chips could, in the future, be assembled and glued together to achieve a portable and compact electrically driven system, where the SiGe photonics circuit can bring advanced functionality to the light source. This chapter is thus dedicated to the first tests of butt-coupling between the QCL and SiGe platforms. The chapter will begin with a brief overview and motivation, referencing relevant prior work reported in the literature. Then, the methodology emphasizing the precise alignment and integration of a QCL chip with a passive SiGe device will be discussed. Our objective in this study is to shed light on the potential of butt-coupling as a robust and efficient alternative for the development of mid-infrared (mid-IR) photonic systems.

3.1 GENERAL OVERVIEW AND PERSPECTIVE OF THE BUTT-COUPLING STUDY IN THE MID-IR

Nowadays, the development of photonic integrated circuits is driven by the compelling need to reduce both the size and cost of optical systems. In general, the coupling of light is typically done by butt-coupling using a free-space configuration for mid-IR experimental demonstrations, which makes them quite bulky. Regarding this context, several coupling approaches have been investigated to enable a compact integrated photonics circuit. One approach is to couple the light from the sample surface using the grating couplers for fiber-to-chip. This approach is a common way to couple light with low loss on photonics circuits. Several significant research have been made to develop grating couplers. For example, a surface grating coupler of a Ge-on-Si waveguide with an inversely tapered operating at a 3.8 µm wavelength has been investigated in 2016 [111]. Their work has been highlighted in the use of the inverse taper concept, which can substantially improve grating directionality. A simulated and measured fiber-chip coupling efficiency of 15% and 7.9% has been reported. Then, fiber-to-chip grating couplers on Ge-on-Si and Ge-on-SOI platforms operated at 5.2 µm wavelength have been theoretically and experimentally investigated by Radosavljevic *et al.*

[112]. Their optimized grating couplers showed coupling efficiencies of 40% and 70% for the simulation and 32% and 40% for the measurement on Ge-on-Si and Ge-on-SOI platforms, respectively. Another work done by J. Kang from the University of Tokyo has reported a subwavelength grating coupler (SWG) to a suspended membrane Ge waveguide at the focusing SWG's center wavelength of 2.37 μm [113]. They have proved that back-reflection, directionality, and coupling strength can be optimized by exploiting the advantage of suspended membrane Ge waveguide with focusing SWGs. Also, a dual-band mid-IR grating coupler with Bragg gratings for wavelength crosstalk suppression on a Ge-on-SOI platform has been theoretically studied recently in 2022 [114]. A high theoretical coupling efficiency of 46.38% and 59.93% for the 8.5 μm and 4.95 μm bands has been reported.

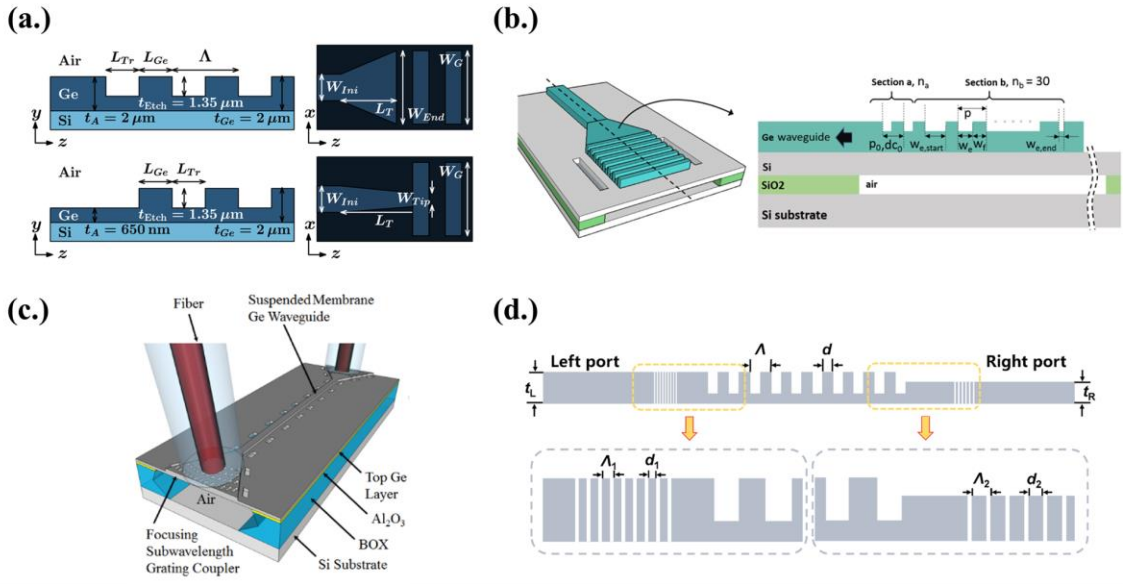

Fig.3.1. (a.) Schematic view of grating coupler with an inverse taper from Ref [111], (b.) Grating structure with their designed for Ge-on-SOI waveguide platform from Ref [112], (c.) 3D view of suspended membrane Ge waveguide and focusing SWGs from Ref [113], and (d.) Cross-sectional views showing geometric parameters of the gratings from Ref [114].

However, going deeper in the mid-IR range, the use of a grating coupler is more challenging. In the long-wave infrared regime, it requires a large grating period (Λ) to obey the phase-matching condition. Also, commercially available single-mode optical fibers in the long-wave infrared have mode field diameters around the operating wavelength's scale. In this sense, a few grating periods already cover the typical beam size. As an illustration, one work of grating coupler was designed at λ = 7.5 μm for the graded Ge-rich SiGe platform in the C2N lab during

the Ph.D. thesis of Q. Liu. He theoretically demonstrated a design for surface grating couplers for TE and TM polarizations [115]. However, the results have shown a comparatively low coupling efficiency of 6.3% (−12 dB) for TE and 11% (-9.6 dB) for TM polarization. A micro-antenna has then been proposed as an alternative way for efficient fiber-chip coupling in the long-wavelength range [116]. Still, an experimental demonstration is required.

Another approach is to couple the light directly from the edge of the sample, which will be mainly discussed in this thesis. In this context, the butt-coupling between 2 separate chips emerges as a significant approach to achieve compactness and cost-efficiency in photonic devices and systems. By enabling the precise alignment and integration of optical components, butt-coupling plays a crucial role in minimizing the space requirements for these components, ultimately leading to more compact optical systems. However, it's worth noting that there is a lack of reports of butt-coupling in the mid-IR. Most of the research and experimentation has been done in the near-IR range. For example, research done by S. Boust *et al.* [117] reports a compact optical frequency comb source based on the butt-coupling between the III-V distributed feedback (DFB) laser and a Si_3N_4 microresonator (Fig.3.2.). That work takes benefit from backscattering from a ring resonator to a butt-coupler laser, which provided a broad comb with a 30 dB bandwidth of 13.6 THz at a center wavelength of 1576 nm without electronic stabilization.

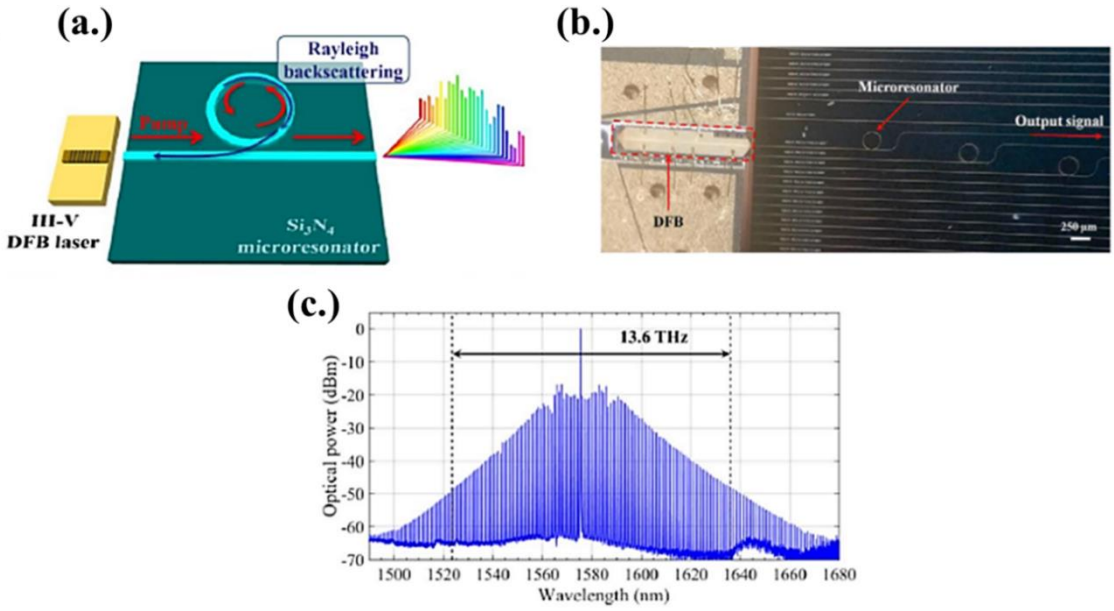

Fig.3.2. (a.) Schematic of optical frequency comb generation by pumping the nonlinear microresonator with the DFB laser. (b.) The photograph of the butt-coupling. (c.) A spectrum

of the generated Kerr comb from the butt-coupling of a DFB laser and a high-Q Si_3N_4 microresonator. Image is taken from [117].

As another example, the ultralow phase noise lasing based on self-injection locking has been demonstrated by using self-injection locking (SIL) of an III-V InP laser to an ultralow-loss CMOS-compatible Si_3N_4 microresonator monolithically integrated with aluminium nitride (AlN) microelectromechanical systems (MEMS) based actuators [118]. A laser combining both low noise and frequency agility - enabling laser tuning at 1.6×10^{15} Hz/s has been achieved.

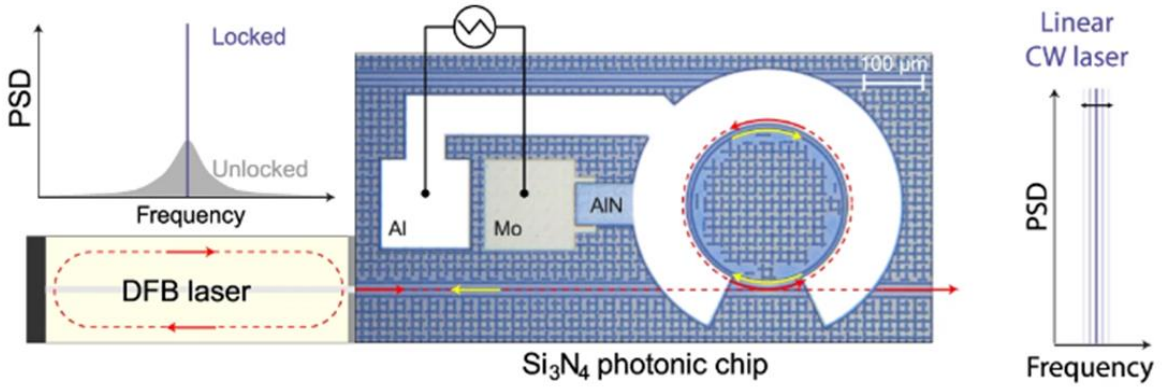

Fig.3.2. Principle of laser linewidth narrowing through laser self-injection locking. The laser frequency tuning is realized by applying a sweeping electrical signal on the monolithically integrated AlN actuator. Image is taken from [118].

Another work developed by G. Roelkens' group from Gent University reported the chip-scale Vernier tunable racetrack resonator filter on the Ge-on-SOI waveguide platform [40]. They implemented widely tunable mid-IR lasers on the Ge-on-SOI platform by butt-coupling a mid-IR III-V gain chip to the silicon photonic IC that comprises a widely tunable filter for the laser wavelength selection. Thermally tunable racetrack resonators with a Q-factor of ~20000, operating in the 5 µm wavelength range, have been experimentally demonstrated.

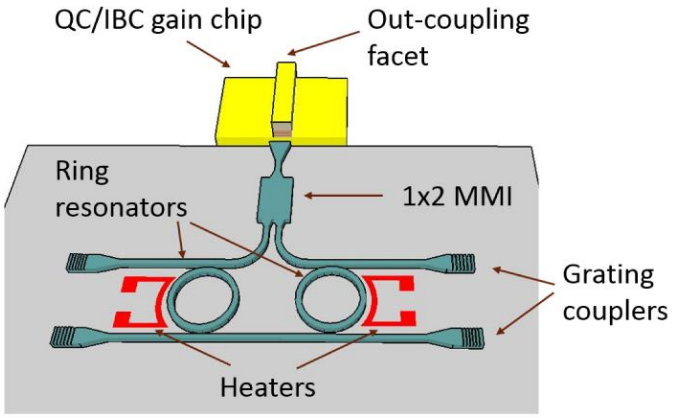

Fig.3.4. A schematic view of widely tunable mid-IR lasers on this Ge-on-SOI platform. Image taken from [40].

In this context, we aim to explore this butt-coupling with our SiGe platforms operating in the 7-8 µm wavelength range. In the following section, I will present the preliminary results done during my Ph.D. thesis, focusing on the initial measurements of butt-coupling. A QCL-based III-V material, similar to the one intended for monolithic integration, will stand as the active source, which will be coupled to one of our SiGe devices. The primary aim of this investigation is to assess the feasibility of direct butt-coupling from a QCL to a SiGe waveguide and to evaluate the limitations in terms of distance and alignment between both chips and their influence on the coupling losses.

3.2 BUTT-COUPLING MEASUREMENT IN THE MID-IR

3.2.1 Initial Results in QCL-to-SiGe Chip Butt-Coupling

In order to facilitate the butt-coupling experiment, I established a new experimental setup at C2N facilities, with the guidance of my Ph.D. supervisor, D. Marris-Morini. The QCL laser is provided by one of our collaborators from the Institut d'Electronique et des Systèmes (IES), Université de Montpellier. The photograph of the first QCL chip can be seen in Fig.3.5(a.). along with their threshold current data. The laser will emit light at 7.4 µm wavelength. The polarity (+) is on the top of the device. After receiving a chip, the bonding between the QCL and the gold pad was done by A. Bousseksou. Also, the facet of the QCL has been observed under the optical microscope as can be seen in Fig.3.5(b.).

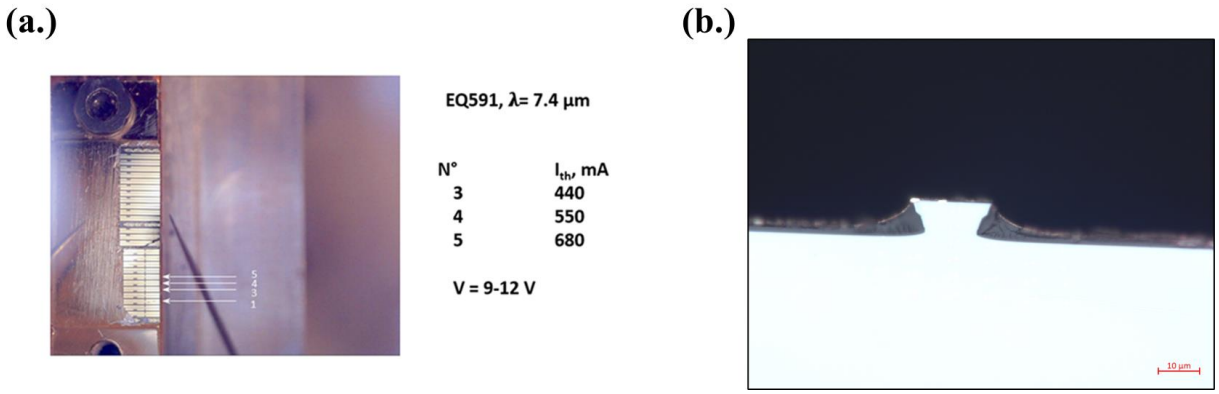

Fig.3.5. (a.) The photograph of the QCL chip provided by the IES. Each number refers to each laser. (b.) QCL facet observation under the optical microscope.

After bonding a laser, I performed the first test by using the experimental setup from A. Bousseksou's group. This involved observing both I-V and far-field measurements. The initial test has been done with the laser number 3, whose threshold current is expected to be 440 mA. The experiment was operated under pulsed current injection with an 84 kHz repetition rate and 200 ns pulse width using an FTIR equipped with an external Mercury Cadmium Telluride (MCT) detector. The current-voltage (I-V) and current-optical peak power (I-L), along with the optical response of the laser, are reported in Fig.3.6. In the current-optical plot, the laser demonstrates lasing activity beyond 375 mA, indicating that the threshold current lies at 375 mA. The laser spectra exhibit a multimode laser with Fabry-Perot characteristics. At the higher pumped current, additional modes become more visible due to an increasing power activation in the gain.

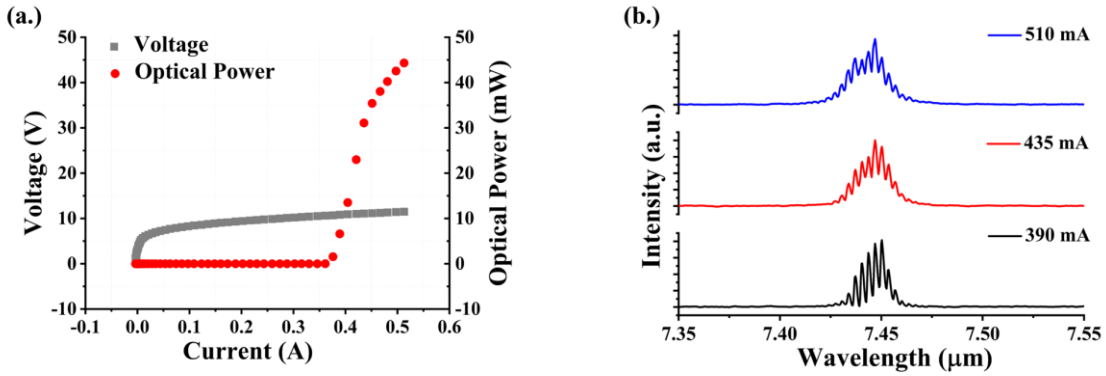

Fig.3.6. Experimental results obtained from laser number 3 under pulsed current injection (a.) Current-voltage and current-optical peak power characteristics at 300 K. (b.) Emission spectra with different pumped currents above the laser threshold.

Then, the far-field emission pattern has been observed in order to assess the appearance of the laser beam. The measurements were performed by sweeping a liquid-nitrogen-cooled MCT detector on a sphere centered on the device facet. The result can be seen in Fig.3.7. A single loop laser can be observed with an artifact in the high power resulting in the red part, which is coming from refraction during the measurement process. Also, the cut-view in one direction (1D) of the sphere has been observed within the sweeping scan step of 0.5° along ϕ and 1° along θ direction.

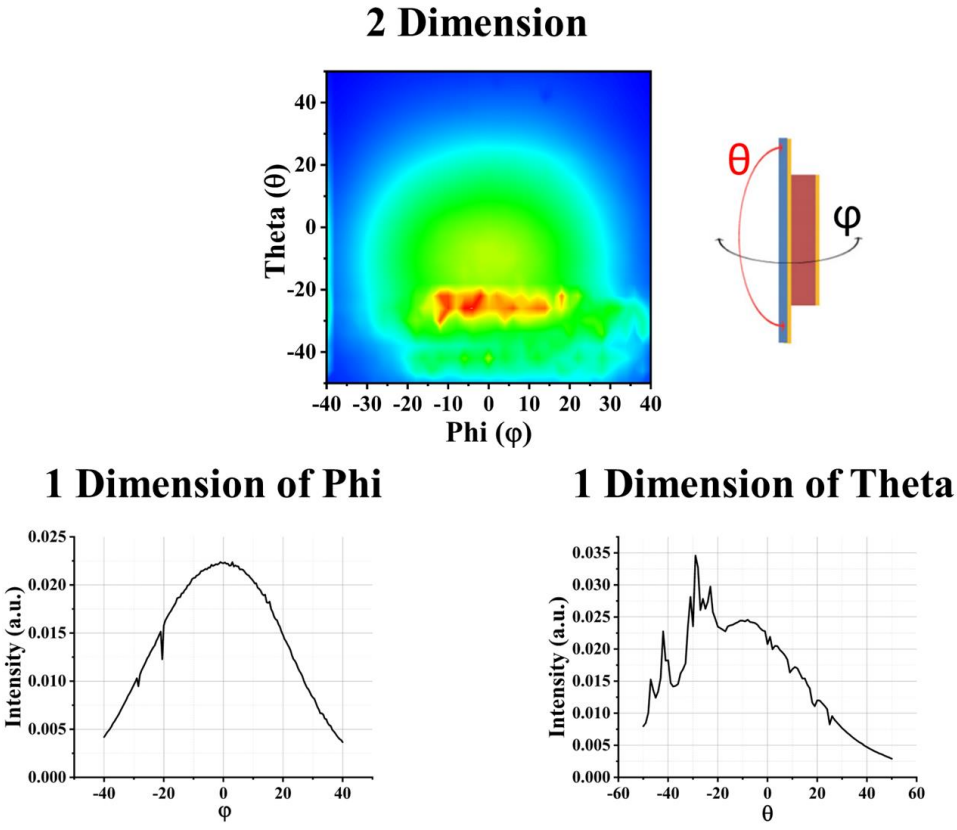

Fig.3.7. Experimental far-field emission pattern of the laser.

Afterward, the butt-coupling study was performed by using our own experimental setup. In fact, the regular mid-IR setup was unsuitable for this particular experiment because it required a specific holder for the QCL and SiGe chip. Therefore, a new experimental setup has been built at the C2N facilities, as mentioned earlier. Fortunately, the new setup did not require extensive space, allowing us to position them closely alongside the standard mid-IR setup. This enabled the simultaneous operation of both setups, providing a valuable opportunity to run experiments concurrently.

The first experiment was carried out to validate the proper functioning of our new setup. In this regard, once again, A. Bousseksou provided me with valuable advice during the experiment. In the beginning, the chip is placed on the holder with the micrometric screws, followed by the ZnSe aspherical lenses to focus the light beam to a high-resolution camera (winCAM). The QCL has been pumped by connecting to the pulse generator (8114A High Power Pulse Generator, 100V/2A). The image of the chip under the test is presented in Fig.3.8(a.), and the observation of the light beam focused on the winCAM camera is shown in Fig.3.8(b.).

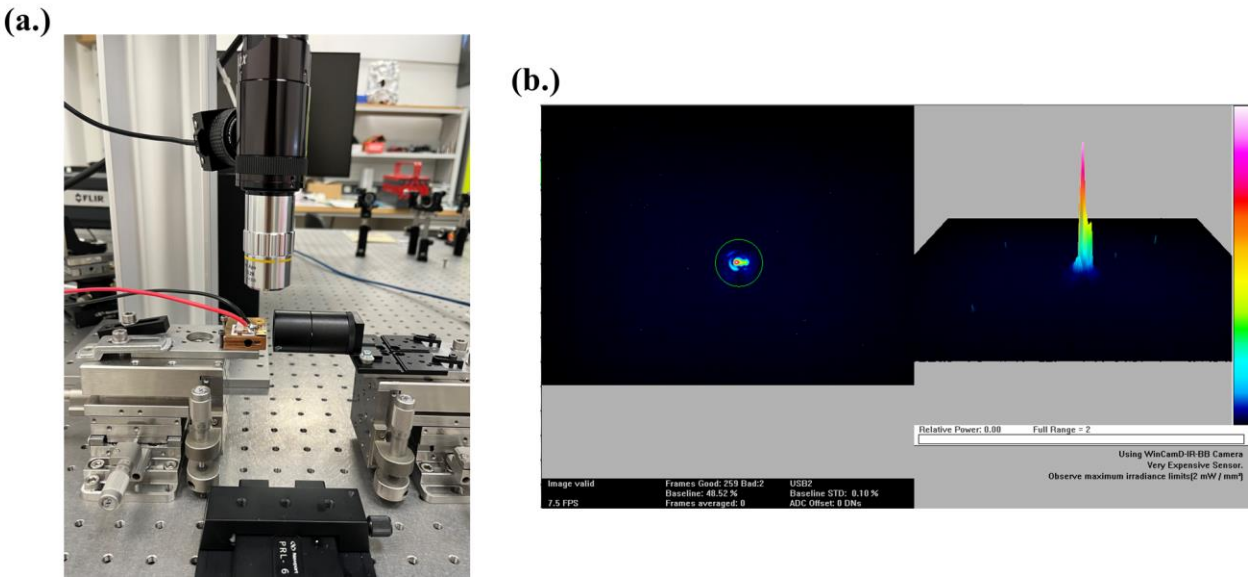

Fig.3.8. (a.) The photograph of QCL-based III-V material coupled with the lens. (b.) Observation of the light beam coming from the laser focused on the camera.

Subsequently, the experiment of the coupling between the two components, the QCL chip and SiGe device has been done by placing the components side-by-side. The straight waveguide with a length of 1.085 cm from a 6-µm-thick-graded SiGe buffer layer with a 2-µm-thick pure Ge on top platform has been chosen as a passive device for a first coupling test. The goal is to observe the light mode through a camera after bringing a passive component closer to an active one. Each component is placed on a different holder with the movement controlled by micrometric screws in three dimensions. The schematic view of the experimental setup can be seen in Fig.3.9(a.). An optical microscope has been used to manage butt-coupling between the QCL laser and the passive chip. A procedure has been established to achieve the coupling condition. First, an IR laser has been used to position the SiGe chip and the lens precisely. Then, the QCL's position has been adjusted to get it in close proximity to the passive device.

In this step, only the position of QCL will be changed to find the mode capture on the camera. The top view of both samples after alignment is shown in Fig.3.9(b.). In the end, I was able to observe light at the output of the SiGe waveguide in the winCAM, as seen in Fig.3.9(c.).

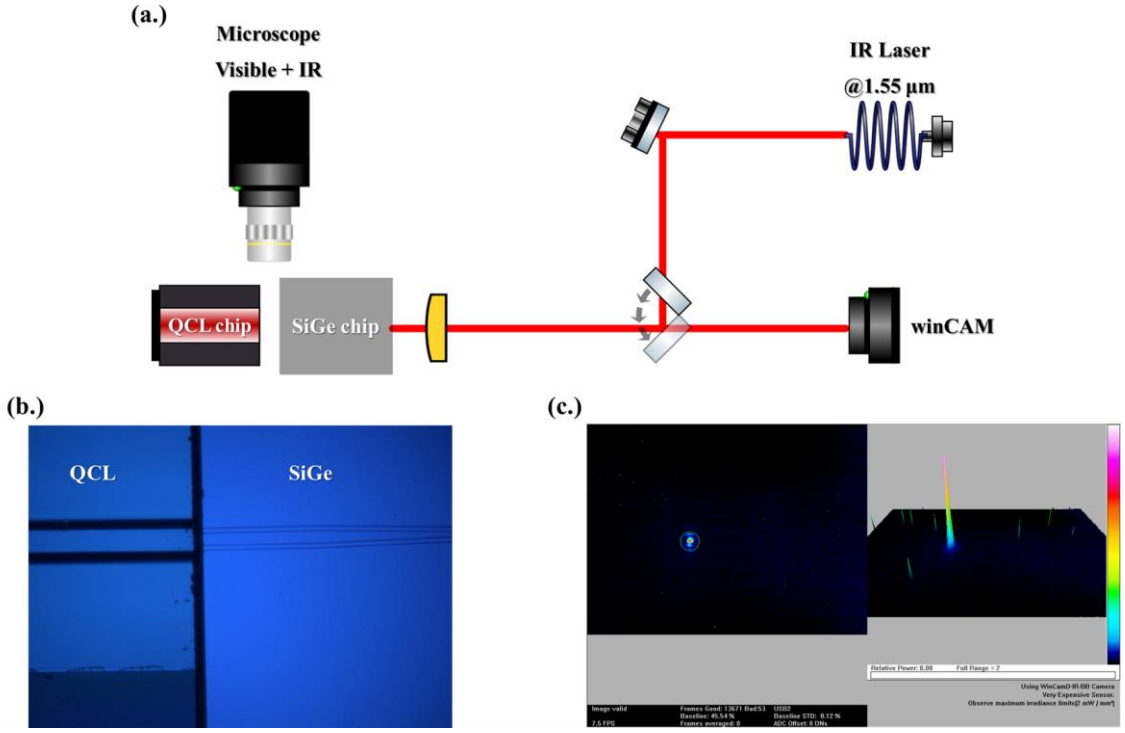

Fig.3.9. (a.) Schematic view of the butt-coupling setup. (b.) The top view image from the optical microscope shows the alignment of an active component (QCL) and the passive chip (SiGe). (c.) Observation of the mode profile from the SiGe device after the butt coupled.

As an initial step, we successfully achieved direct butt-coupling from the QCL to the SiGe platform in the mid-IR range (λ = 7.4 µm). The gap between the QCL and the SiGe has been manually estimated from the optical microscope, which is around 12 µm. In order to minimize the separation between the two chips, both their facets must be perfectly aligned. For QCL, it has been required to push the laser slightly away from the chip holder as the edge of the holder was causing interference with the coupling. Also, the SiGe chip has to be completely diced to achieve the flat facet. Our next phase will be to extract the coupling losses between the two components.

3.2.2 Coupling Loss for QCL-to-SiGe Chip

In order to take advantage of this measurement in the future, the coupling loss of the QCL-to-

SiGe chip should be evaluated. To do so, a high-speed MCT detector (PVI-4TE-10.6, Vigo System) has been used to collect the output light. In this regard, a new QCL chip EQ591.1D, has been used for the coupling loss measurement. The threshold current is estimated to be 490 mA. The same SiGe chip has been employed, which is the 6-µm-graded SiGe layer with a 2-µm pure Ge on top. The propagation loss of this platform has been experimentally demonstrated by another PhD student, V. Turpaud. The losses should be around 1.5 dB/cm at 7.4 µm wavelength. It is worth mentioning that this experiment was done with invaluable assistance from my colleague H. Dely. The output power has been measured when placing and removing the SiGe chip by the high-speed MCT detector, which is connected to the oscilloscope with a 50Ω impedance. The signal collected from the oscilloscope of different pump powers of the QCL-to-lens and QCL-to-SiGe chip can be seen in Fig.3.10.

	QCL Output	**SiGe photonics circuit output**
Pump = 17.5 V	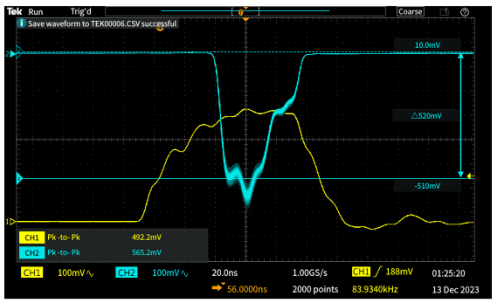	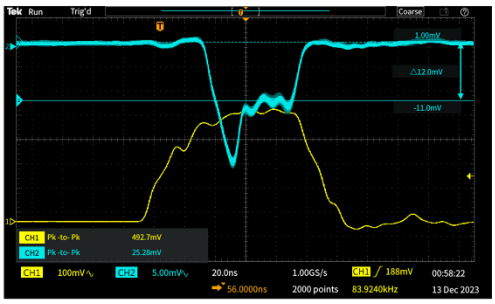
Pump = 18.4 V	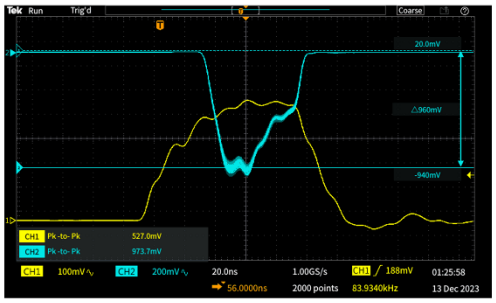	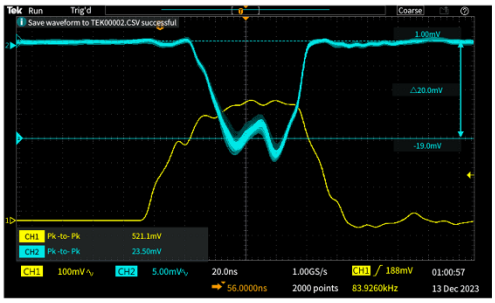
Pump = 20.8 V	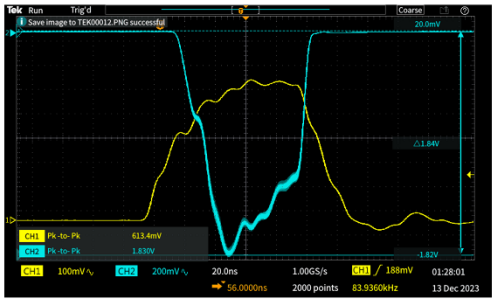	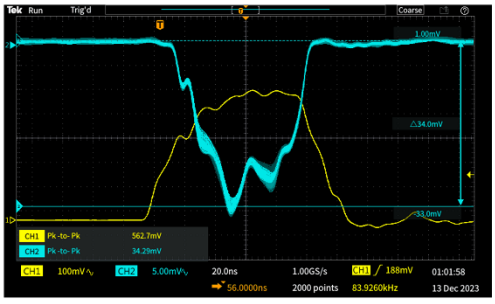

Fig.3.10. The collected signal with and without SiGe photonic circuit during the butt-coupling measurement at different pump power. The yellow line represents the current applied to the laser, and the blue line represents the voltage at the output of the VIGO detector, which is proportional to the detected power.

The power measured at the output of the laser and at the output of the SiGe photonic circuit can be seen in Fig.3.11. The power fraction of coupling has been calculated to be around 2% between the QCL-to-lens configuration (without SiGe) and butt-coupling between QCL-SiGe chips (with SiGe). It should be noted that the power collected at the output of the SiGe photonic circuit has suffered from the coupling loss between QCL and SiGe photonic circuit, the propagation loss of the waveguide, and also the collection loss at the output facet (~5 dB/facet).

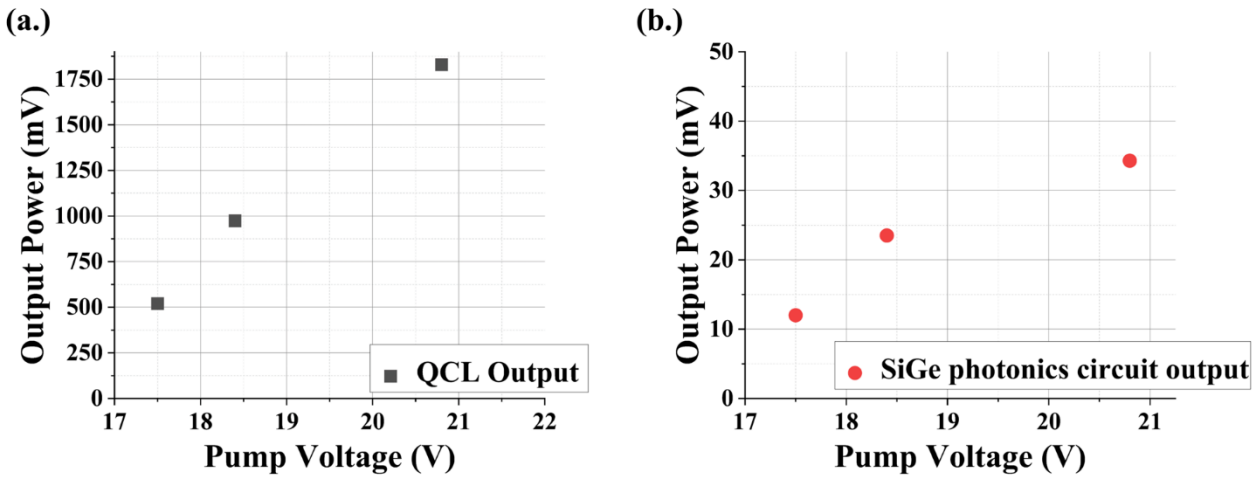

Fig.3.11. The output power in the function of the applied voltage for different configurations: (a.) from QCL output and (b.) from SiGe photonics circuit output.

Then, the total losses in the system can be calculated by using this expression:

$$Total\ loss\ (dB) = -10 \times \log\left(\frac{P_2}{P_1}\right) \tag{3.1}$$

When P_1 is an input power measured when removing SiGe chip, and P_2 is a coupled power.

Considering the average value calculated from each applied voltage, a total loss of 16.6 dB has been obtained. In this sense, the coupling loss of around 10 dB has been extracted when considering the waveguide propagation loss of 1.5 dB/cm, and the loss due to the facet of 5 dB/facet.

Furthermore, I conducted a preliminary numerical analysis to quantify the loss resulting from the beam's overlap with the SiGe chip. To achieve this, I simulated a beam at various gap distances and determined the overlap within a square area matching the dimensions of the input waveguide (15 μm width, and 4 μm etching depth). The percentage of the overlap of the beam in a function of the gap distance can be seen in Fig.3.12(a.). The percentage decreases when the gap distance increases which is leading to a higher coupling loss at the larger gap. Additionally, the loss attributed to refraction at the input waveguide was estimated to be approximately 4 dB using Fresnel's refraction equation. Consequently, the combined coupling loss, incorporating both the overlap and refraction, is depicted in Fig. 3.12(b).

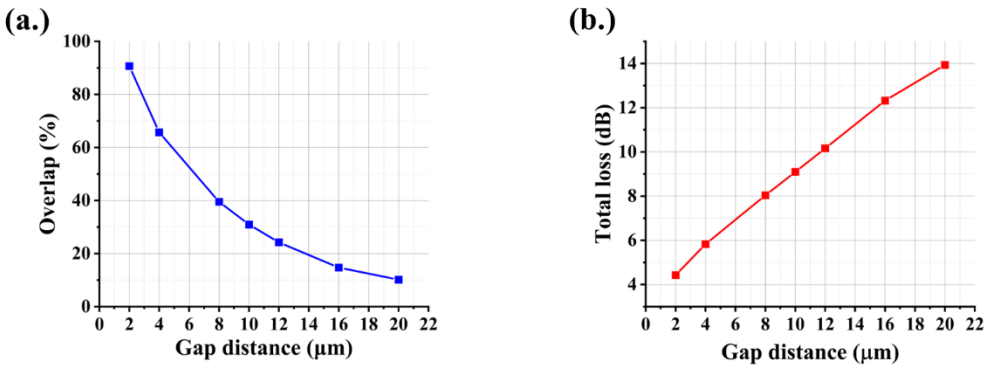

Fig.3.12. Numerical simulation of (a.) the overlap percentage in a function of a gap distance between QCL and SiGe chip, (b.) the combined coupling loss from both the overlap and refraction.

3.3 CONCLUSIONS

In this chapter, I have addressed an experimental demonstration of the butt-coupling between the QCL-based-III-V material and the SiGe photonics circuit operated at 7.4 μm wavelength. The butt-coupling technique has been demonstrated as a promising method for integrating QCLs source with SiGe devices in a compact way. A successfully separated chip coupling has been obtained. A coupling loss of around 10 dB can then be extracted from the measurement. However, further improvements in alignment and chip-to-chip spacing are necessary to optimize to obtain better coupling efficiency. The 3-axis blocks piezoelectric holder should then be introduced in order to control the coupling position in a very high resolution. This work has opened the route for future advancements in mid-IR integrated photonic systems.

4 BROADBAND RACETRACK RESONATOR IN THE LWIR

The second objective of the thesis was the development of passive building blocks to complete the functionalities offered by the mid-IR photonic platform. Indeed, over the past few years, a whole set of mid-IR photonic components have been demonstrated exploiting graded SiGe waveguides, including Mach-Zehnder interferometers [56], Bragg grating Fabry-Perot cavities [57], racetrack resonators [58], or integrated Fourier-transform spectrometers [59, 119]. However, the quality factor (Q-factor) of these resonators was limited to a few thousands.

This chapter is devoted to the work done towards the development of high Q-factor integrated resonators in the long-wave infrared region (spanning the spectral range of 8 - 14 µm wavelength) based on the SiGe-graded index platform. To begin, I will provide an overview of the underlying motivation and the current state of the art. Next, the concept of racetrack resonator will be discussed, followed by the presentation of the first run of resonators that I characterized, which is fundamentally based on previous research work [8]. The challenges encountered during the design, fabrication, and optical characterization will be discussed. The new approach developed during this thesis will then be described. Interestingly a thermal heater will be embedded in the resonator to overcome the set-up limitation in terms of spectral resolution. The design, fabrication, and characterization results of this second run of resonators will then be discussed. To close this chapter, the conclusion and perspective for future work will be discussed.

4.1 STATE-OF-THE-ART OF THE RACETRACK RESONATOR

4.1.1 Literature Reviews and Motivation for Integrated Resonator in the LWIR

Generally speaking, ring (and racetrack) resonators play a critical part in a wide variety of different on-chip integrated sensing schemes. They are commonly developed at telecom wavelength (1.55 µm), and it has been shown that they can be used (i) as a compact sensor that effectively increases the interaction length between the propagation mode and the analyte [120], (ii) as a notch filter that is used to finely select and reject narrow frequency band [121], (iii) to enhance the non-linear Kerr effect which can benefit for a frequency comb generation around the pumping wavelength [122], or (iv) as an interferometric structure for a compact and efficient modulator [123]. In all these sensing schemes, a high-quality factor (Q-factor) is necessary. It is worth noting that the maximum achievable Q-factor (also called intrinsic Q-

factor) depends only on the waveguide losses in the ring. At telecom wavelengths, the highest Q-factor has been obtained using silicon-on-insulator (SOI) [20] and silicon-on-sapphire (SOS) [124] platforms. However, these waveguides become lossy when the wavelength is beyond ~3.5 µm and ~6.5 µm, respectively, which limits their use in the mid-IR.

Focusing on the mid-IR spectral range, integrated resonators are developed mainly for frequency comb generation in the context of dual-comb spectroscopy (DCS), which is an interesting method for measuring optical spectra across a broad spectral range with high-frequency resolution. Indeed, among the different approaches that have been demonstrated for the on-chip frequency comb generation, microresonator-based comb generators have the potential to generate broadband frequency comb in a compact integrated platform, providing that low waveguide loss, strong light confinement, and significant third-order nonlinearity can be obtained simultaneously.

However, there are only a few reports of integrated resonators operating in the mid-IR spectral range. On one hand, most of the integrated resonators have been reported below 6 µm wavelength. For instance, T.-H. Xiao *et al.* have demonstrated an air-cladding microring resonator coupled with a suspended-membrane waveguide with a loaded Q-factor of ~57,000 at 2.15 µm wavelength, on a GOI platform [45]. In another work on the MWIR, using a $Si_{0.6}Ge_{0.4}$ ring resonator operating around 4.18 µm, a loaded Q-factor of 90,000 has been obtained [125]. On the other hand, there have been only a few research works on integrated resonators beyond 6 µm wavelength reported in the literature. For example, a germanium-on-silicon (GOS) resonator operating in the LWIR up to 11 µm wavelength has been reported in ref [38] with a Q-factor of 10^4. Also, D. Ren *et al.* have observed an intrinsic Q-factor of 2.5×10^5 at 8 µm wavelength from Ge microdisks coupled with a partially suspended waveguide on a separated circuit [126]. However, such microdisks still remain unpractical for on-chip integration.

Interestingly, a broadband integrated racetrack resonator operating at 8 µm wavelength and based on a graded SiGe photonics circuit has been reported previously in our research group [58]. Based on this previous result, my work has been devoted to the improvement of the racetrack resonator targeting Q-factor up to 10^5 operating in the LWIR regime. Indeed, this corresponds to the estimated minimum value for future demonstration of micro-comb generation based on Kerr effect in the mid-IR.

4.1.2 Fundamental Principles of Ring Resonator

Ring resonators consist of a looped optical waveguide and a bus waveguide used for light input/output. The looped waveguide and the bus are coupled together. When the shape of the resonator is elongated with a straight section to increase the coupling length, we usually call it a racetrack resonator. A pictorial representation of a ring and racetrack resonator is given in Fig.4.1.

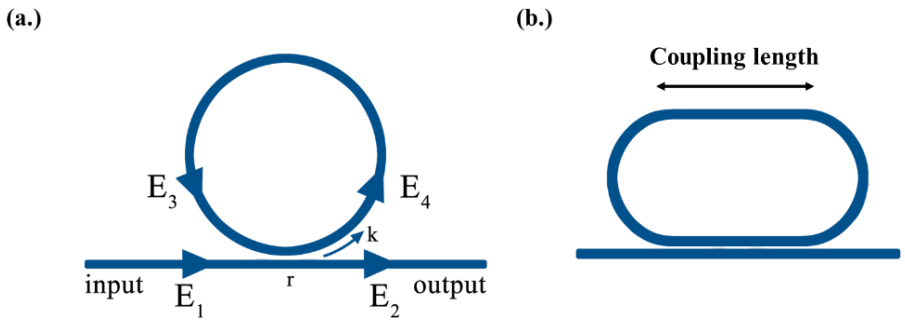

Fig.4.1. Schematic view of (a.) Ring resonator indicating the field associated with the resonator, (b.) Racetrack resonator, readapted from Ref. [127].

Given that the work presented in this thesis is based on the all-pass filter (APF), also known as the notch filter configuration, which corresponds to the case where there is only one bus waveguide, all subsequent descriptions will similarly be based on the all-pass filter. The fundamental spectral characteristics of ring resonators can be easily derived by assuming continuous wave (CW) operation and matching fields. This analysis assumes that reflections back into the bus waveguide are negligible. The fundamental relationships between the incident E_1, transmitted E_2, and circulating fields of a single resonator E_3, E_4 is obtained by combining the relations for the coupler with those of the feedback path and can be described by the matrix relation [123, 127, 128]:

$$\begin{pmatrix} E_4(\omega) \\ E_2(\omega) \end{pmatrix} = \begin{pmatrix} r & i\kappa \\ i\kappa & r \end{pmatrix} \begin{pmatrix} E_3(\omega) \\ E_1(\omega) \end{pmatrix} \tag{4.1}$$

where the lumped self- and cross-coupling coefficients r and κ are assumed to be independent of frequency. This means $r^2$and κ^2 are the power splitting ratios of the coupler, and they are assumed to satisfy the relation $r^2 + \kappa^2 = 1$ (no loss in the coupling regime).

The relation between circulating field E_3 and E_4 can be expressed as:

$$E_3 = e^{-\frac{\alpha ring}{2}2\pi R} e^{i\beta L} E_4 \equiv a e^{i\phi} E_4 \tag{4.2}$$

where ϕ represents the single-pass phase shift, $\phi = \beta L = \frac{2\pi n_{eff}}{\lambda} L$, when L is the round-trip length, β is the propagation constant of the circulating mode, n_{eff} is the effective index of the propagating mode in the ring, and a represents the single-pass amplitude transmission, which is related to the power attenuation coefficient $\alpha_{ring}[1/cm]$ as $a^2 = exp(-\alpha L)$.The ratio of the transmitted and incident field in the bus waveguide can be written by solving the Eq.4.1. and Eq.4.2. as:

$$\frac{E_2}{E_1} = e^{i(\pi+\phi)} \frac{a - re^{-i\phi}}{1 - rae^{i\phi}} \tag{4.3}$$

In order to obtain the intensity transmission T, squaring Eq.4.3. is used. It can be written as:

$$T = \frac{I_2}{I_1} = \left|\frac{E_2}{E_1}\right|^2 = \frac{a^2 - 2ra\cos\phi + r^2}{1 - 2ar\cos\phi + (ra)^2} \tag{4.4}$$

The resonance in the ring can be found when light propagating in the ring acquires after a turn a phase shift corresponding to an integer multiple of 2π ($\phi = 2\pi m$), or when the optical length corresponds to a discrete number of times the field wavelength, as written:

$$\lambda_{res} = \frac{n_{eff} L}{m}, m = integer \tag{4.5}$$

One important concept when working with ring resonator is the coupling regime. The coupling regime can be explained using transfer matrix modeling, which considers the balance between the loss due to the coupling out of the resonator, and the loss inside the resonator itself. Three regimes can be obtained:

1. Under coupling regime (r > a) or ($\kappa^2 < \alpha L$): In this regime, only a small fraction of light couples into the resonator. Most of the light remains in the bus waveguide. This configuration indicates a high Q-factor because light that is trapped in the resonator circulates inside for a long time before decaying.
2. Critical coupling regime (r = a) or ($\kappa^2 = \alpha L$): When light from the input waveguide couples into the ring, it is perfectly matched to the ring cavity loss rate. This results in

maximum power transfer from the input waveguide to the ring resonator. In this regime, the largest extinction ratio (ER) will be found.

3. Over coupling regime (r < a) or ($\kappa^2 > \alpha L$): In this regime, the loss due to the coupling out the resonator is higher than the loss inside the resonator itself. This results in a reduction in both the ER and the Q-factor.

The three different coupling regimes, and their influence in the transmission spectra are illustrated in Fig.4.2.

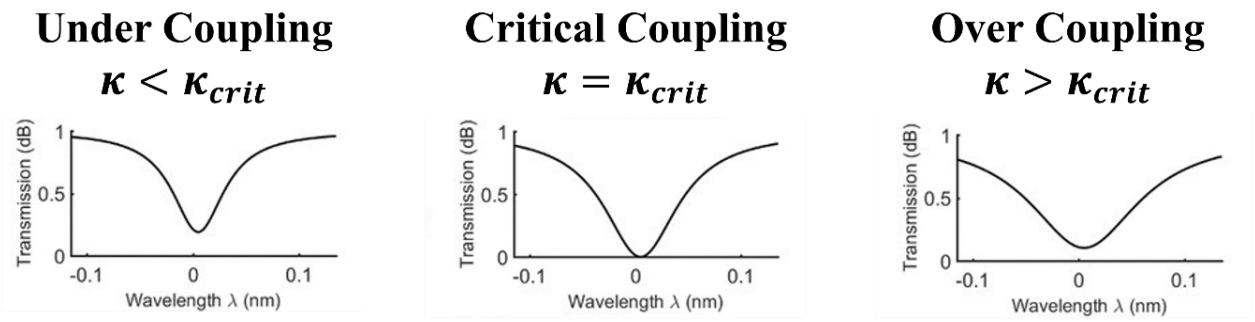

Fig.4.2. Schematic view of the transmission spectra of resonators under three different regimes. The resonance is getting wider from the under coupling to over coupling. Images have been readapted from [129].

Considering the critical coupling, the coupled power is equal to the power loss in the ring, $r = a$, leading to $T = 0$ at resonance condition. The transmission at resonance drops to zero.

In the next step, I will discuss the key parameters to compare the properties of ring resonators. One of the important parameters is the distance between the resonance peaks, so-called the free spectral range (FSR) [123] which is given by:

$$FSR = \frac{\lambda^2}{n_g L} \tag{4.6}$$

where $n_g$is the group index. The link between the effective index and the group index can be written as:

$$n_g = n_{eff} - \lambda_0 \frac{n_{eff}}{\lambda} \tag{4.7}$$

Another important parameter is the full width at half maximum (FWHM), which is used to

define the resonance width in the spectral domain. The FWHM is related to the parameter of the ring [109] as:

$$FWHM = \frac{(1-ra)\lambda_{res}{}^2}{\pi n_g L\sqrt{ra}} \tag{4.8}$$

In the experiment, the extraction of the FWHM comes after fitting the resonator intensity transmission around a resonance with a Lorentzian function, which can be generally written as:

$$y = y_0 + \frac{1}{\pi}\frac{2\sigma}{[4(x-x_0)^2+\sigma^2]} \tag{4.9}$$

where σ represents the spectral width of the Lorentzian fitted curve which gives the -3dB resonance bandwidth.

The next parameter is the quality factor (Q-factor) of the resonator, which quantifies the sharpness of its resonance concerning its central frequency, and can be written as:

$$Q = \frac{\lambda_{res}}{FWHM} \tag{4.10}$$

In another way, the Q-factor can be defined by the ratio of the stored energy circulating inside the resonator to the energy lost per optical cycle as: $Q = \omega_o \frac{Stored\ energy}{Power\ loss}$. It can be seen that the Q-factor denotes the number of field oscillations that occur before the circulating energy is reduced to $1/e$ of its initial energy. It can also be rewritten as a function of the all-pass ring resonator physical parameter as:

$$Q = \frac{\pi n_g L\sqrt{ra}}{\lambda_{res}(1-ra)} \tag{4.11}$$

It should be noted that this Q-factor is the total Q-factor of the device-also known as loaded Q-factor. In fact, the energy loss per cavity round trip is coming from 2 contributions. The first one is the intrinsic cavity loss in the cavity, which consists of light scattering, radiation loss, and absorption. Another one is the extrinsic coupling loss by the coupled waveguide [130]. Therefore, the loaded Q-factor has two contributions: one originating from propagation losses and the other related to losses caused by the coupler. This is conventionally expressed as follows:

$$\frac{1}{Q_L} = \frac{1}{Q_i} + \frac{1}{Q_C} \tag{4.12}$$

where Q_L is the total or loaded Q-factor, which can be measured experimentally, Q_i is the intrinsic Q-factor of a stand-alone resonator, and Q_C is the Q-factor contribution due to the coupling.

The intrinsic Q-factor can be determined from the loaded Q-factor and the measured extinction ratio [20] following by this equation:

$$Q_i = \frac{2Q_L}{1 \pm \sqrt{T_0}} \tag{4.13}$$

where T_0 is the normalized transmitted power at the resonance wavelength. The sign for the term in the denominator is determined based on the coupling regime of the resonator whether the ring is in the under- or over-coupled regime. In this thesis, the main objective is to improve the Q-factor of the resonator, the under coupled condition is required. Then, Eq.4.13 can be rewritten as:

$$Q_i = \frac{2Q_L}{1 + \sqrt{T_0}} \tag{4.14}$$

Moreover, when knowing the intrinsic Q-factor deduced from the Eq.4.14, and the transmitted power at the resonance wavelength from the measurement, it is possible to extract the propagation loss [131] by this relation:

$$Q_i = \frac{2\pi n_{eff}}{\alpha \lambda_{ref}} \tag{4.15}$$

From Eq.4.15, the main parameter that influences the intrinsic Q-factor is the power attenuation coefficient related to the loss of the waveguide. Loss can come from different origins: the propagation loss, the bending loss, or the loss of the mismatch between the interface of the bus waveguide and the bend. The relation of the power attenuation coefficient can be expressed as:

$$\alpha_{tot} = \alpha_{prop} + \alpha_{bend} + \alpha_{mismatch} \tag{4.16}$$

Therefore, in this work, I am trying to negotiate all the parameter be obtain the highest Q-factor in the LWIR based on the SiGe waveguide platform.

4.2 RACETRACK RESONATOR FOR THE LONG-WAVE INFRARED (LWIR)

4.2.1 Previous Work on the Racetrack Resonator for LWIR

To begin with, my work has been built upon the foundations laid by J. Ramirez *et al.* [58], who was a Postdoc in our research group (MINAPHOT at C2N), to continue his work in the racetrack resonator in the LWIR. In 2019, J. Ramirez demonstrated racetrack resonators operating at 8 µm wavelength with loaded Q-factor of 3200 on the SiGe-graded index platform. The conclusion of his work was that the measurement was limited by the resolution of the set-up. Indeed, a pulsed laser was used, whose emitted spectral width was comparable with the width of the resonance features to be measured. I have thus started the work by choosing a pre-existing sample, which had been fabricated in the previous work in my research group [8], to replicate the experiment. The SEM images of the pre-existing sample can be seen in Fig.4.3. This sample will be called "run 1".

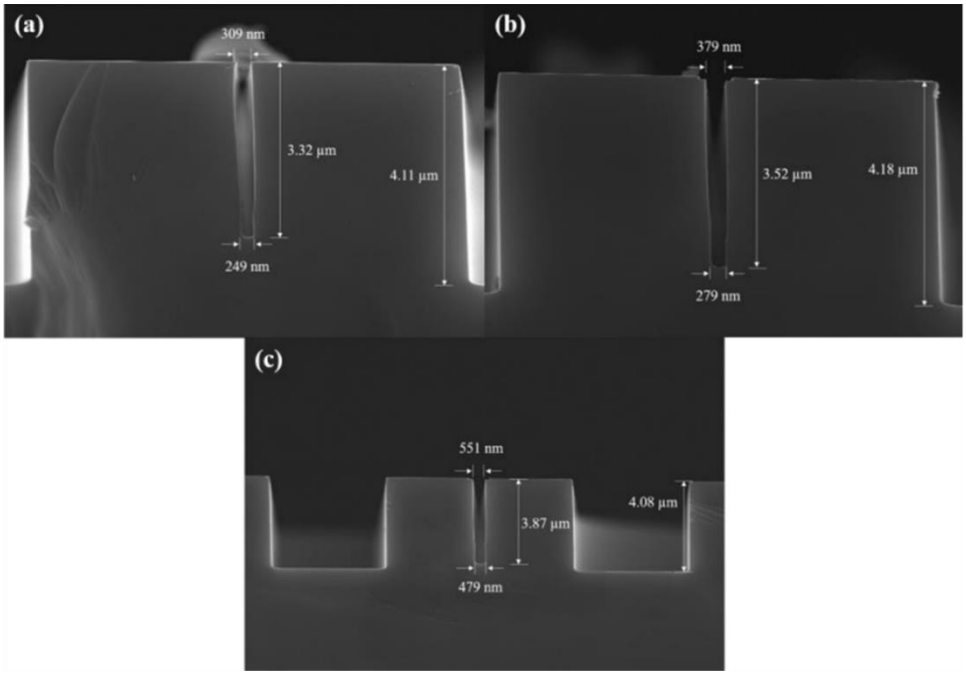

Fig.4.3. SEM images of fabricated racetrack resonator showing different gap of (a.) gap of 500 nm, (b.) gap of 400 nm and (c.) gap of 500 nm with the etching depth around 4 µm. The image is taken from [132].

4.2.1.1 Mid-Infrared Free Space Experimental Measurement

The measurement has been done by using 2 different MIR lasers (MIRCAT, Daylight Solutions), which are both external cavity Quantum cascade laser, operating in different

conditions: i.) in pulsed regime with 100 kHz repetition rate and 5% duty cycle, and ii.) in continuous wave (CW) operation. All measurements of the photonic devices reported in this chapter are done in quasi-TM polarization. Briefly, the light emitted from the QCL is butt-coupled to the photonic chip. A pair of ZnSe aspherical lenses are utilized to inject and collect the light in the waveguide. The light at the output of the device is collected and detected by a Mercury Cadmium Telluride (MCT) detector (DSS-MCT-020, Horiba) cooling down with liquid nitrogen, which is connected with lock-in detection. As the first laser operated in pulsed operation, the trigger signal can be obtained directly in the lock-in amplifier system, which means the voltage detected in the lock-in amplifier is directly related to the optical power collected from the MCT detector. To ensure that the light is well-coupled in the waveguide, the mode has been monitored by using a high-resolution camera (WinCAM). The schematic view of the experiment is illustrated in Fig.4.4.

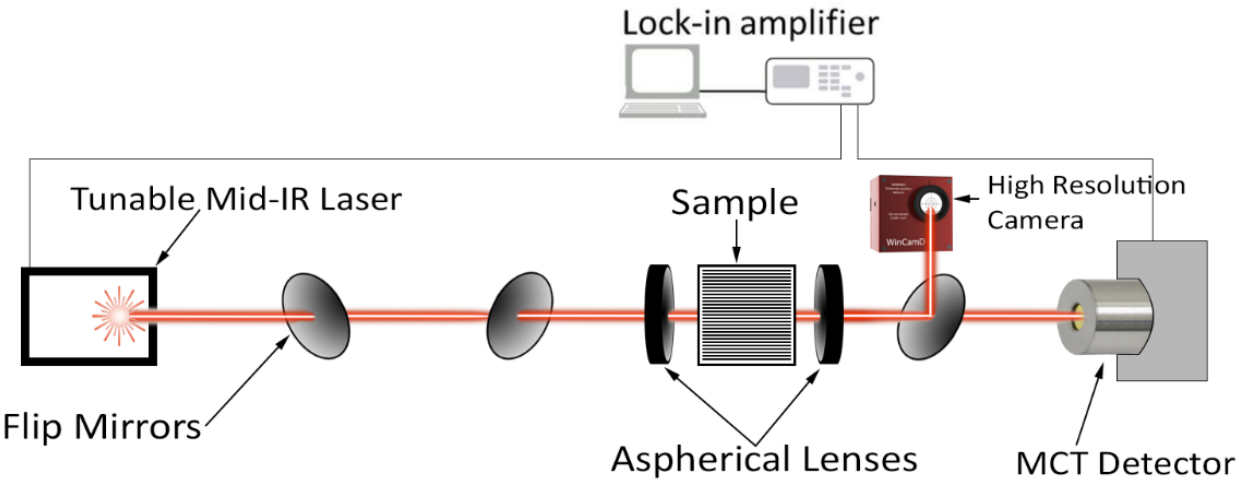

Fig.4.4. The scheme of the characterization setup.

The results are reported in Fig.4.5. A set of resonators (radius of 250 µm, coupling length of 60 µm, and different values of the gap between the bus waveguide and the resonator) have been characterized with the two lasers. It should be noted that the value of the gap reported in Fig.4.5. is the value from the GDS design, not the real gap of the device. The shown transmission spectra have been normalized by the raw transmission spectrum over its envelope.

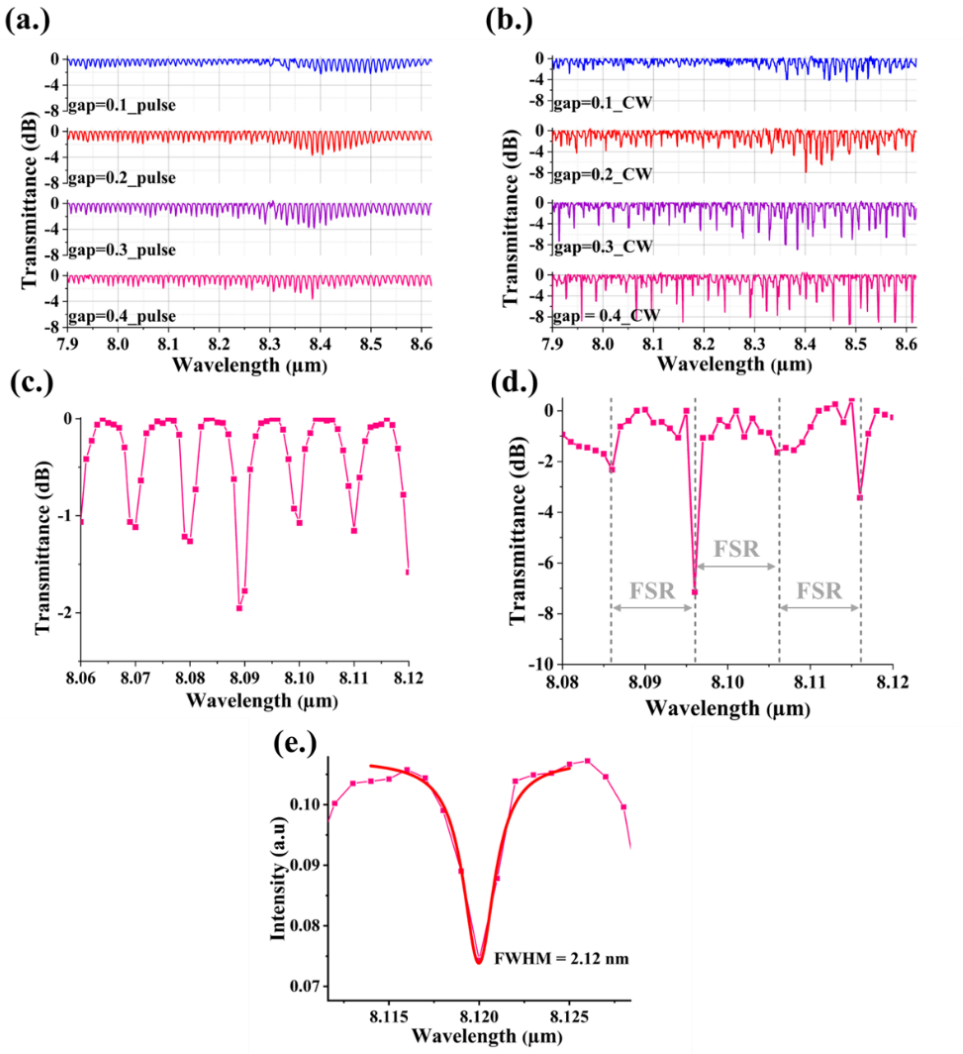

Fig.4.5. Measured transmission spectra of racetrack resonator operating in TM-polarization when the radius is 250 µm, the coupling length of 60 µm with the different gaps measured with (a.) a QCL laser in pulsed regime; (b.) a CW QCL. The comparison of the zoom-in views of the measurement of the racetrack with the gap of 0.4 µm shows the limitation coming from each laser: (c.) in pulsed regime, the laser linewidth smooths the measured resonance; (d.) in CW regime the laser linewidth is much narrower, but the measurement is limited by the resolution of the external cavity laser. (e.) Zoom in view of a single-resonance peak (racetrack with R = 250 µm, coupling length = 60 µm, and gap of 0.4) measured in pulses operation, the solid red line indicates the Lorentzian fitting to extract the FWHM.

A clear interferometric pattern characteristic of the transmission of ring resonator has been observed from both setups, in a wide spectral range (wavelengths from 7.9 to 8.6 µm). Nevertheless, when comparing zoom-in views of both measurements, the limitation

measurement coming from each laser can be seen. For the pulsed operation, the linewidth of the laser is not negligible when compared with the width of the measure resonance leading to a smoothing effect of the resonance; from the manufacturer specification, the linewidth of the pulsed operation is supposed to be <1 cm^{-1}, which corresponds to 6 nm at 8 µm wavelength. Still, the FWHM can be extracted after the Lorentzian fitting of the resonance peaks, as shown in Fig.4.5(e). The highest Q-factor obtained from this measurement is 3800 at 8 µm wavelength, which is comparable with the result reported previously [58]. When considering the results obtained using the CW laser, a larger extinction ratio of the resonance peaks can be seen due to a narrower linewidth of the laser. Indeed, the linewidth of the CW laser is <100 MHz, corresponding to 20 pm at 8 µm wavelength, which allows, in theory, to probe cavity resonances with Q-factors up to 4×10^5. However, the patterns of the resonance are not uniform because of the limited tuning step size of the emitted wavelength, coming from the laser itself (QCL in an external cavity). Indeed, the minimum tuning step size has been set at 1 nm, which is the smallest step size of the laser. If considering that the resolution of 1 nm is not fine enough to resolve all resonance peaks, the FWHM is typically smaller than 1 nm, leading to a Q-factor larger than 8×10^3 at 8 µm wavelength.

4.2.1.2 Distributed Feedback Quantum Cascade Laser (DFB-QCL) Measurement

To confirm the limitations of our MIR setup, and investigate further the performances of the resonators, a DFB-QCL laser has been used. Indeed, DFB lasers benefit from the possibility to finely tune the emitted wavelength by tuning the temperature (or current) of the laser. The price to pay is the limited bandwidth in comparison with external cavity lasers. A mid-IR DFB-QCL was available in the team of A. Bousseksou, operating around 8.5 µm, and has been used to measure the transmission of the resonators. In this regard, A. Bousseksou and his Ph.D. student, L. Lucia, have provided significant assistance during the experiment by guiding me through the setup alignment and all the measurements. The schematic representation of the setup can be seen in Fig.4.6.

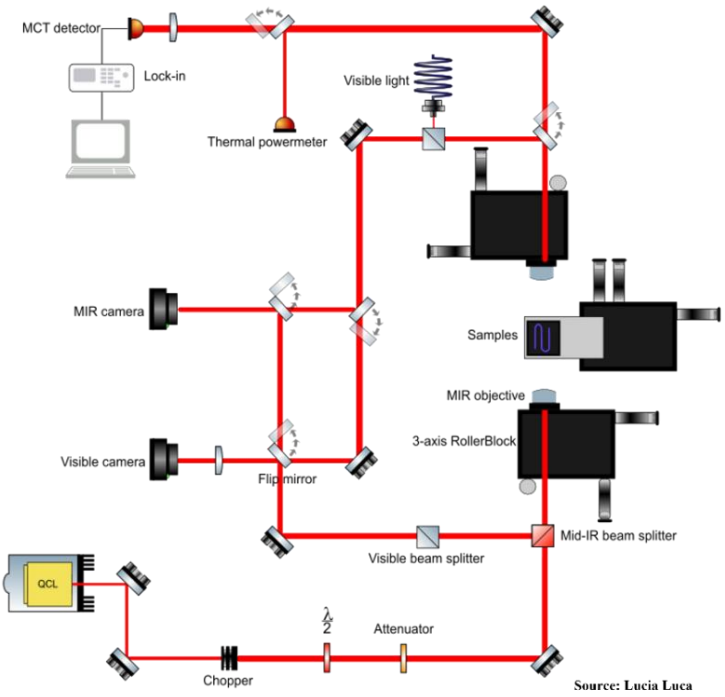

Fig.4.6. Schematic view of the DFB laser setup.

Shortly, the sample is positioned within a holder that allows for three-axis movements. The MIR objective lenses are used for coupling light into and out of the sample. The signal is collected using a cooled Mercury-Cadmium-Telluride (MCT) infrared photodetector. The MIR camera and visible camera are applied during the alignment to ensure that light is well-coupled in the waveguide. The spectral tuning range is from 8.4986 – 8.5489 µm, over 20 – 40 °C. The relation between the wavelength, current and temperature tuning is shown in Fig.4.7. A rough estimation of the wavelength tuning can be estimated by analyzing the slope of the graph at a specific temperature. In the measurement, the temperature has been set to 30 °C, leading to a change of 0.0857 µm/A.

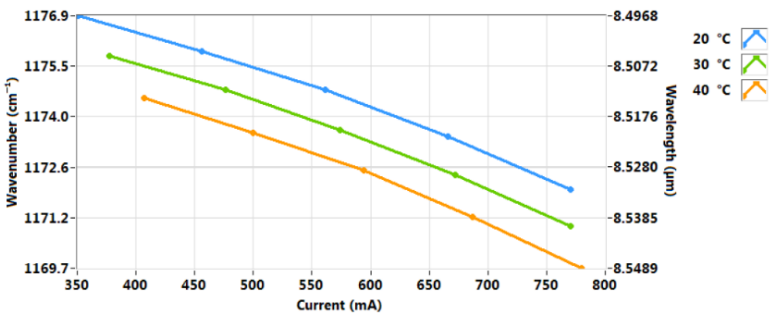

Fig.4.7. Wavelength tuning of the DFB-QCL as a function of the applied current at different temperatures, from Ref [133].

Examples of measured transmission of the integrated resonators are reported in Fig.4.8., along with the zoom-in view at the resonance peak. It is worth noting that thanks to the very fine-tuning step size of the measurement, for the first time, the Fabry-Perot fringes coming from the facet of the waveguide have been observed.

Interestingly, a FWHM of the resonance of 1.44 nm has been measured, leading to a Q-factor of 5900 at 8.5 µm wavelength, which verifies that the results of our original setup have been limited from the laser.

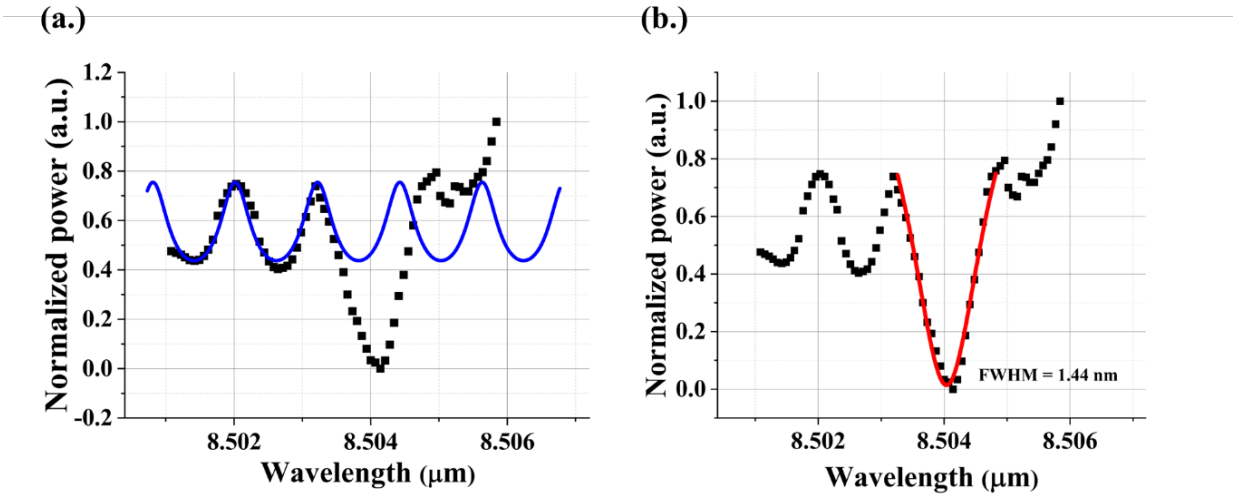

Fig.4.8. (a.) Experimental transmission spectra of racetrack resonator operating in TM-polarization from the DFB setup. The racetrack radius is 250 µm with a coupling length of 60 µm. The blue curve indicates the simulated Fabry-Perot model. (b.) Zoomed-in view of a single resonance of the left-side graph, showing the Lorentzian fit in red curve.

In conclusion, the analysis of the run 1 sample allowed us (i) to compare and analyze different experimental set-up and experimental conditions, (ii) to demonstrate the possibility to achieve Q-factor of 5900. Considering the loaded Q-factor of 5 900 from the racetrack with 250 µm radius and 60 µm coupling length operating at 8.5 µm wavelength, the intrinsic Q-factor of 1.1×10^4 has been extracted by using the Eq.14. Also, average propagation loss (that includes both absorption and radiative/scattering losses) can then be calculated using Eq.15, and loss around 11 dB/cm is obtained. It can be noticed that this deduced loss is higher than the experimental propagation loss measured on this platform, the propagation loss is supposed to be around 3 dB/cm. Considering the three contributions of loss, propagation loss seems to be the main limitation of achieving high Q-factor. However, run1 was fabricated before 2019. As

fabrication process of the SiGe photonics circuits has been improved in the recent years, I then started a second run, starting from the design, up to the fabrication of the sample in C2N cleanroom and its characterization on the different experimental benches.

4.2.2 Integrated Resonator: Run 2: Design, Fabrication, and Characterization

4.2.2.1 Design and Simulation

The device relies on the 6 µm-thickness SiGe platforms on top of Si substrate, which has been grown by the low-energy plasma-enhanced chemical vapor deposition (LEPECVD) by G. Isella's group of Politecnico di Milano (Como, Italy). On this platform, Ge concentration is increased linearly from 0% (pure Si) to 100% (pure Ge) along the growth direction over a 6-µm-thick layer. This platform has been chosen as a good candidate to achieve a good tradeoff between a low-defect density in the material and thus low propagation losses and a good confinement of the optical mode that will be required to enhance Kerr nonlinearity in the perspective of using such integrated resonators for comb generation. Further information on this platform can be found in [55]. As for the sample from run1, the waveguide has been chosen to be 4 µm-wide and the etching depth is 4 µm, which allows good confinement of the guided mode in the wavelength range of interest. The schematic view of the waveguide dimension can be seen in Fig.4.9. along with the refractive index profile of the material.

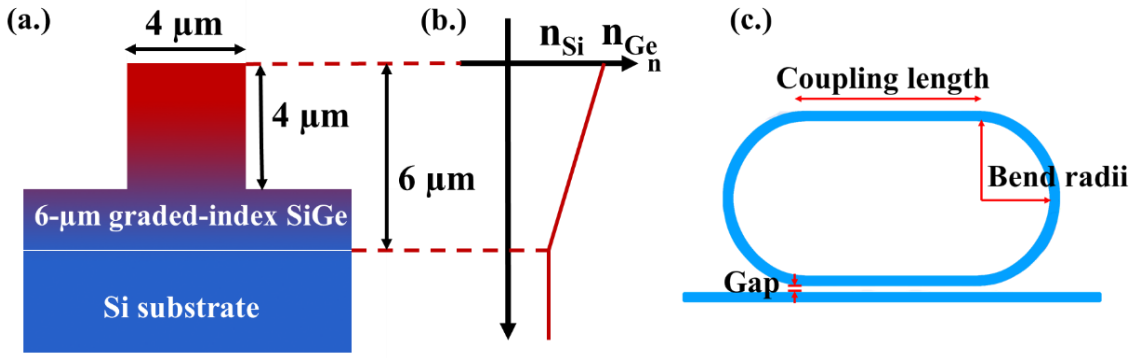

Fig.4.9. (a.) Cut-view of the Ge-rich SiGe waveguides showing the waveguide dimensions. (b.) Profile of the refractive index in the SiGe layer: linear variation of the refractive index from pure Si (n=3.42) to pure Ge (n=4.01). (c.) General top view of the racetrack resonator.

The number of modes depends on the wavelength and can be calculated numerically by using Finite Difference Eigenmode (FDE) method. Considering quasi-TM polarization, 2 modes can

be found when the wavelength is smaller than 8.6 µm, while the waveguide is single mode when the wavelength is larger than 8.7 µm, as reported in Fig.4.10. This behavior is common to graded SiGe waveguide, and it has been shown previously that multimode operation is not detrimental to the device performance. Indeed, when 2 modes are found, the high order mode shows 2 lobes in the vertical direction, and not in the lateral direction as obtained more usually in the optical waveguide with constant refractive index material core. Coupling to higher order occurs when there is perturbation of the confinement. In our case, higher order modes will not be excited in the photonics circuits or in the ring resonator, as there is no perturbation of light confinement in the vertical direction.

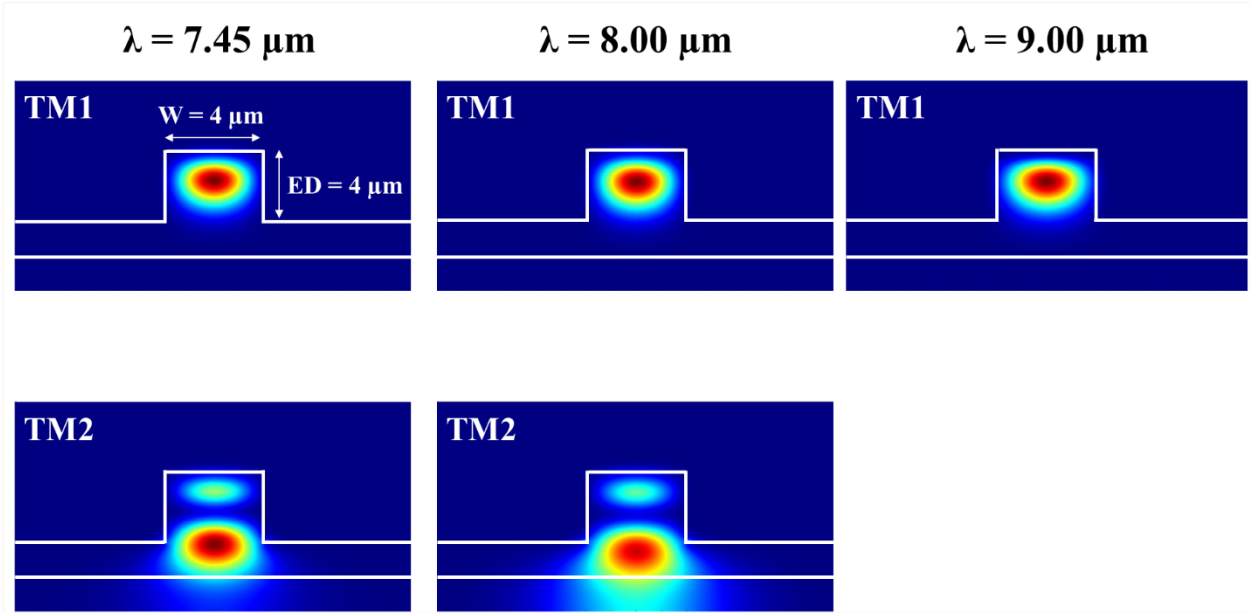

Fig.4.10. Simulated TM mode profiles at different wavelengths (λ = 7.45, 8, and 8.5 µm). In TM2, it can be seen that the higher order mode shows 2 lobes in the vertical direction.

Then, the racetrack resonator should be designed to optimize the resonator Q-factor. The resonator parameters are the radius of the resonator, the coupling length, and the gap between the bus waveguide and the resonator. In order to achieve a high Q-factor, the first losses should be as small as possible, to maximize the intrinsic Q-factor of the resonator.

In this regard, I first started with the 3D simulation using the Finite-Difference Time-Domain (FDTD) method on Lumerical's software to estimate bending losses of the waveguide, as a function of the bending radius. The simulated bending loss is shown in Fig.4.11. As expected, loss decreases when the bend radius increases. Losses around 3.06 dB/cm are obtained for a

radius of 100 µm. Unfortunately, simulation of the structure with bending radius larger than 100 µm is not possible because of the size of the structure.

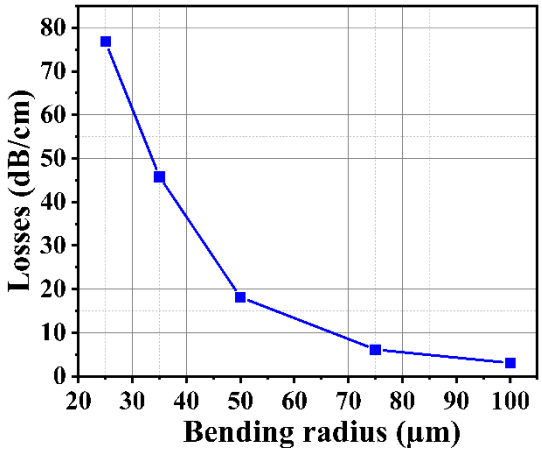

Fig.4.11. The simulated bending loss in a function of each radius. The bending loss of R > 100 µm cannot be simulated due to the size of the structure.

Then in a second step, the coupler dimensions should be defined (gap and coupling length). Generally speaking, the ring part and the bus waveguide must be in close proximity, so, they can couple the light from one waveguide to the other. Typically, the gap will be set around 100 nm for strip waveguides on a 220-nm-SOI platform to be able to achieve the critical coupling at telecom wavelength (~1.55 µm wavelength). However, regarding the SiGe-graded fabrication, the waveguide etching depth needs to be a few µm to maintain the light confinement in the upper part of the waveguide. To do that, it is very challenging to etch such a narrow gap to achieve the same etching with the waveguide. In this work, the gap has been set to ease the fabrication process, and a value of 1 µm is typically used. In the simulations, the coupler was thus designed using two 4 µm-wide waveguides, an etching depth of 4 µm and a fixed gap of 1 µm to facilitate device fabrication.

To achieve a high Q-factor, operating in the under-coupled regime (r > a) is targeted. In this context, only a small fraction of light should couple into a resonator (small κ^2). Considering a resonator radius of 250 µm (to be able to neglect bending losses), and propagation losses of 1 dB/cm, Eq.4.11 can be used to estimate that a coupling coefficient around 1% is required to target a resonator Q-factor of around 10^5.

Based on this estimation, the coupler length can then be designed using the results from the

coupled mode theory (CMT). In summary, in a directional couleur, it is possible to model light propagation by calculating the "supermodes" of the structure, namely the symmetric and anti-symmetric modes, as shown in Fig.4.12(a,b). If we initially consider that we have 100% power in waveguide 1, then the power in waveguide 2 is given by [134]:

$$P_2(L) = P_0 sin^2\left(\frac{\pi L \Delta n_{eff}}{\lambda_0}\right) \tag{4.17}$$

Where P_0 is the input power, L is the length of the coupling region, and λ_0 is the wavelength and Δn_{eff} is the effective index difference between the symmetric and anti-symmetric modes of the structure. Then, the coupling length (L) to achieve any desired power coupled to waveguide 2 can be calculated as in Eq.4.18:

$$L = \frac{\lambda_0}{\pi \Delta n_{eff}} sin^{-1}\left(\frac{P_2}{P_0}\right) \tag{4.18}$$

The Finite Difference Eigenmode (FDE) method on Lumerical's software is used to calculate the supermodes within the coupler. The evolution of the coupling coefficient as a function of the coupler length can thus be deduced using Eq.4.18., as can be seen in Fig.4.12(c).

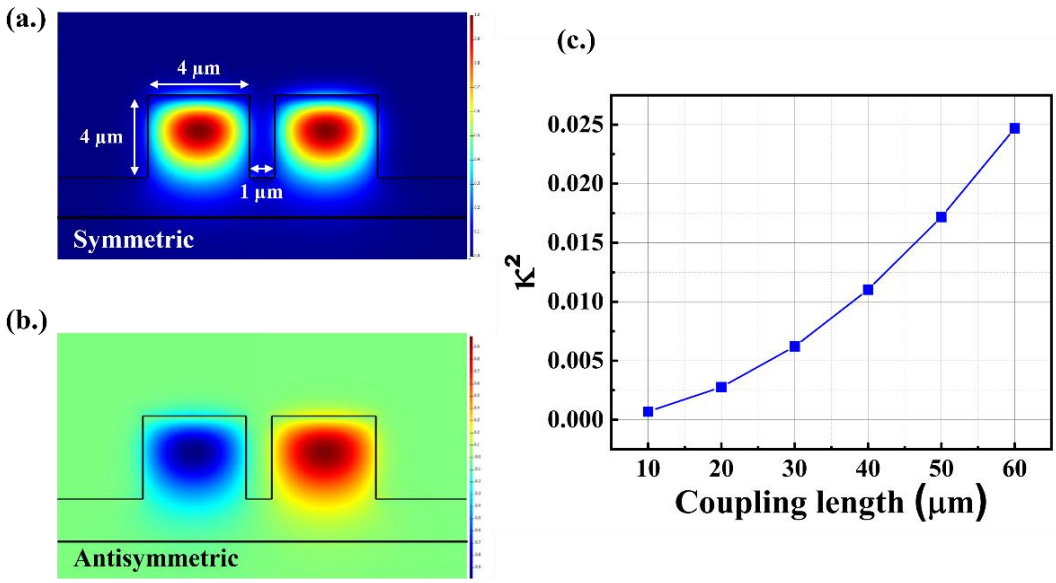

Fig.4.12. Simulated coupled mode at 8 µm wavelength for (a.) symmetric and (b.) antisymmetric quasi-TM mode. (c) Simulated coupling coefficient κ^2 of the 1-µm-gap waveguide as a function of coupling length at λ = 8 µm.

Based on these numerical fabrications, the parameter of the rings in the second run of

fabrication have been tuned as following: The resonator radius size has been selected as 50, 100, 150, 200, and 250 µm. The coupling length is then designed to be 0, 30, 45, and 60 µm. The gap is set around 0.8 and 1 µm. The GDS design for the lithography can be seen in Fig.4.13.

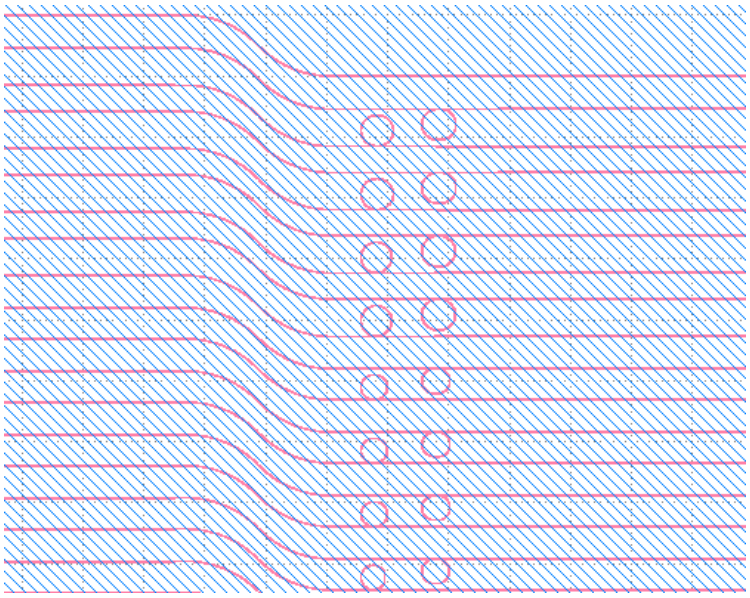

Fig.4.13. The GDS design shows different radius, gap and coupling length dimensions for run2 device.

4.2.2.2 Fabrication Process

Standard cleanroom techniques are used to fabricate the sample. The fabrication flow is presented in Fig.4.14. Once we receive the wafer, the wafer is first cleaned with acetone for 10 mins, followed by isopropanol for 10 mins. In order to ensure proper cleaning, a diluted HF solution is used after solvent cleaning. Then, an electronic photoresist "CSAR.18" is spin-coated on the surface with a speed of 1450 rpm, expected to achieve a thickness of 1.4 µm. An annealing is first started with a temperature of 90 °C for 1 min and then the temperature is increased to 150 °C; this approach can reduce the stress inside the photoresist during the annealing. The electron beam lithography (EBPG) is deployed to pattern the waveguide, followed by the ICP-RIE dry etching. The width and etching depth of the waveguide are designed to be 4 µm as mentioned. The waveguide facets are then diced by using mechanical dicing to obtain smooth facets for the butt coupling in the experimental setup. In the end, the sample is cleaned by piranha and HF cleaning to remove the photoresist that has been left on the surface. The top view of the devices has been observed under the optical microscope and shown in Fig.4.14. as well.

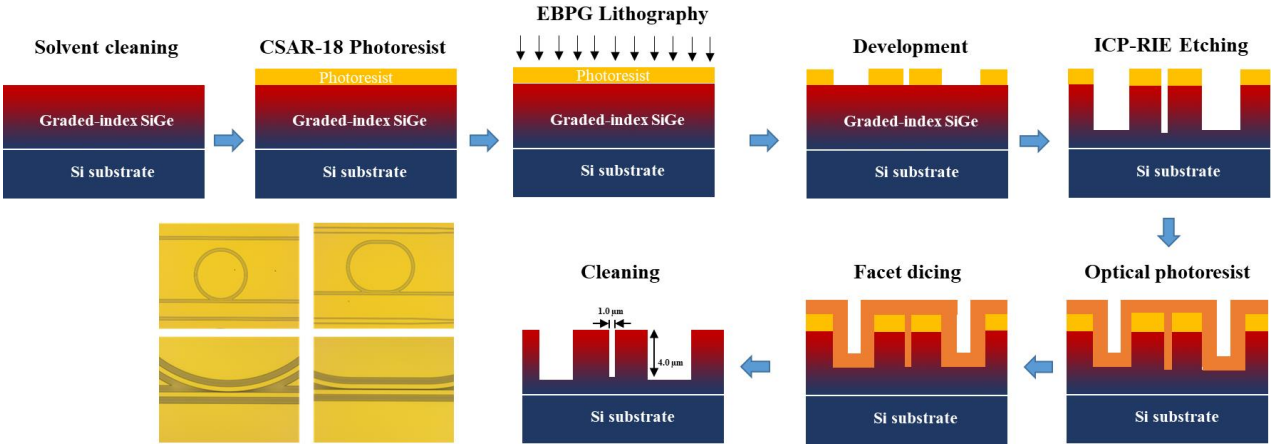

Fig.4.14. Fabrication process flow and the optical microscope image of the racetrack resonator with different coupling lengths, along with the zoom-in part in the directional coupler.

4.2.2.3 Experimental Results

This device is then characterized, first by using the pulsed-QCL, in the wavelength range from 7.8 to 8.8 μm. Wideband resonator operation is observed from both gaps, shown in Fig.4.15. When zooming in the spectra, the same limitation as described previously occurs, as partial clipping of the resonance features is observed.

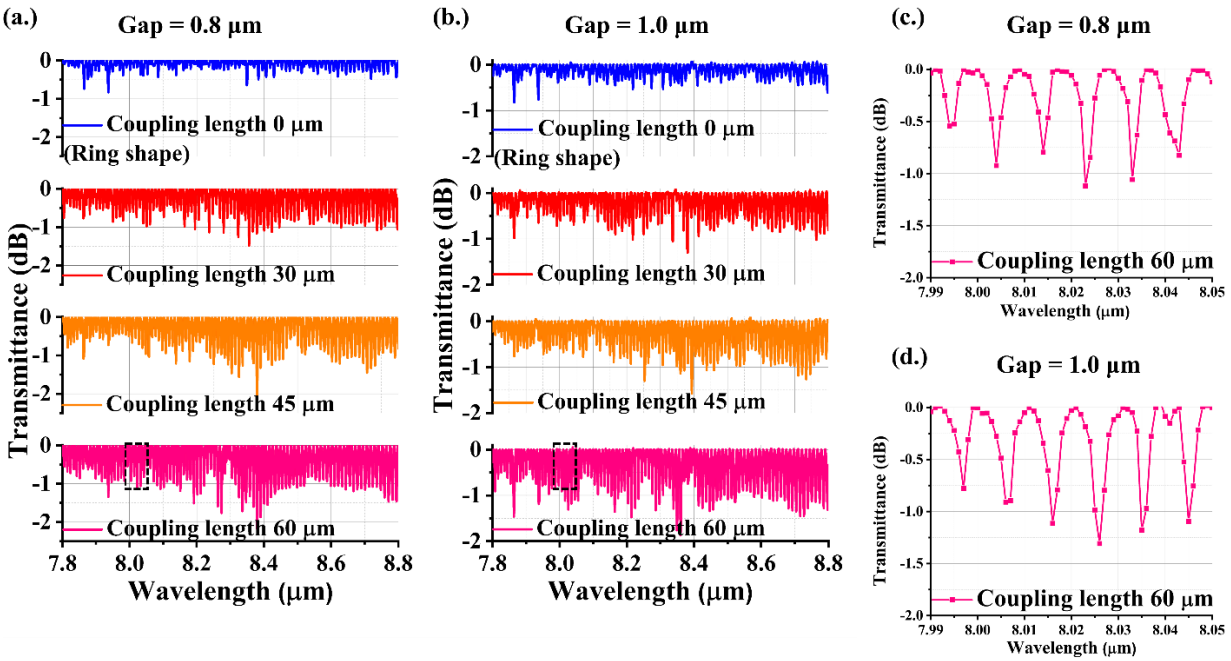

Fig.4.15. Transmission spectra of different racetracks with a radius of 250 μm in quasi-TM-polarization with (a.) gap = 0.8 μm. (b.) gap = 1.0 μm, respectively, and for different lengths

of the directional coupler (30, 45, and 60 µm). Zoom-in of the spectral around 8 µm wavelength of the results from the spectra part of the longest coupling length (60 µm) with (c.) gap = 0.8 µm. (d.) gap = 1.0 µm, respectively.

Then, the measurement using the DFB-QCL at 8.5 µm has been performed. A zoom in the transmission around resonance of a device with a radius of 250 µm, a gap of 0.8 µm, and different coupling length can be seen in Fig.4.16. Interestingly, it can be clearly seen that the FWHM increases when the coupling length increases. The coupling coefficient refers to the measure of energy transfer between the two waveguides that form the resonator. When the distance between the bus waveguide and the resonator is extended, the overlap between the two waveguides is stronger, leading to a larger portion of the energy being transferred from one waveguide to the other, which results in a higher coupling coefficient. So, when the coupling coefficient increases, the resonator operation changes towards the over-coupling regime. Regarding this behavior, the Q-factor of a resonator will generally be lower due to a higher energy dissipation out of the resonator. It can be noticed that in some graphs, the Lorentzian fitting is not so good. This is because of the lack of smoothness caused by insufficient resolution during the experiment (not enough points). However, it is still possible to make a rough estimation of the FWHM for calculating the Q-factor. Interestingly, a highest Q-factor of 2.25×10^4 has been observed from the device with the radius of 250 µm, the coupling length of 0 µm (ring shape), and a gap of 0.8 µm with FWHM of 0.377 nm at around 8.5 µm wavelength. Referring to Eq.4.14. and Eq.4.15., we have determined an intrinsic Q-factor of 2.8×10^4, leading to an estimated propagation loss of approximately 4.3 dB/cm.

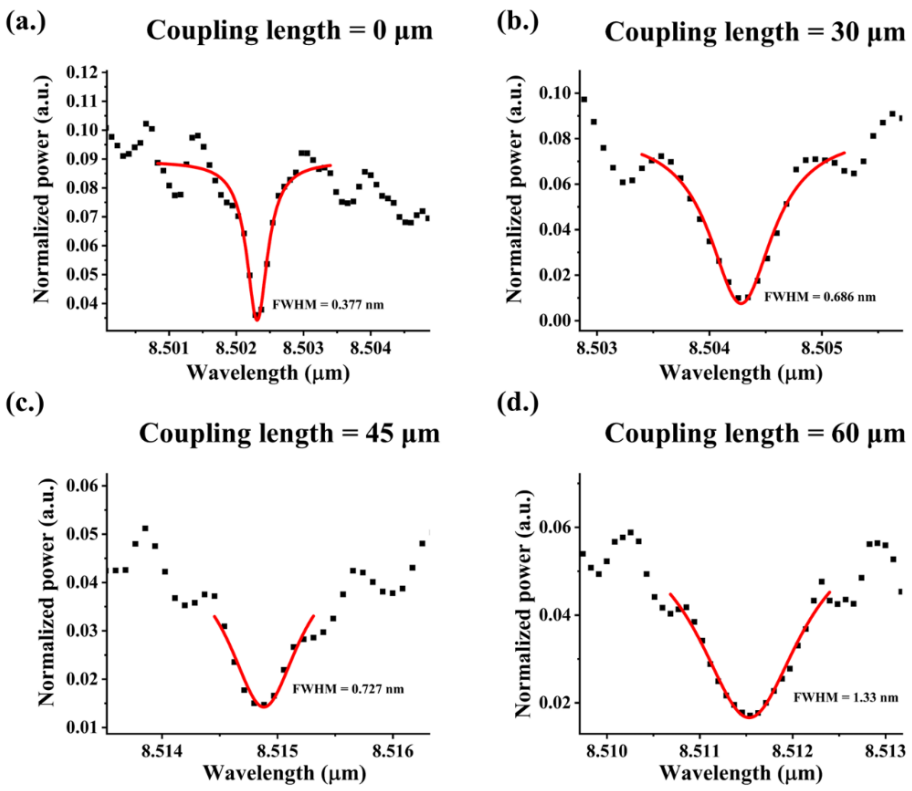

Fig.4.16. Transmission of a resonator when measured using the DFB-QCL laser with a radius of 250 µm, a gap of 0.8 µm, and different coupling lengths (a.) 0 µm, (b.) 30 µm, (c.) 45 µm and (d.) 60 µm, respectively. The highest Q-factor has been estimated with the smallest coupling length, as expected.

From this measurement the performance of the integrated resonators has been improved from run1 to run 2, thanks to several variables. The improved design has yielded a loaded Q-factor of 2.25×10^4. Notably, a significant decrease in propagation loss deduced from Eq.15 has been evident, reducing from 11 dB/cm in run1 to 4.3 dB/cm in run2 at 8.5 µm wavelength. The reduction of the propagation loss can come from the advancement during the growth material. In addition, the reduction of the coupling length leads to the obtaining of a small coupling coefficient, which also improves the Q-factor of the resonator.

Furthermore, it has been confirmed that the measurement with DFB-QCL shows a much better resolution than both external cavity QCL. However, the spectral range of the DFB-QCL is limited to a few nanometers around 8.5µm wavelength. Therefore, a new approach has been proposed to achieve high resolution measurement in a wide spectral range, as described hereafter.

4.3 THERMO-OPTICS RACETRACK RESONATOR: RUN 3

The objective of the third run of devices is to be able to measure ring resonances with high resolution (which means that the measurement should not be limited by the experimental set-up), in a wide spectral range, typically from 7.8 to 8.8µm wavelength. To cover such wavelength range with a narrow linewidth laser, the CW external cavity QCL has to be used. However, the tuning of the emitted wavelength is limited by the position of the mirror forming the external cavity. This is why it has been proposed to work at a fixed wavelength, and to measure the resonator resonance by tuning no more the input wavelength but the optical phase of the light traveling in the resonator. To do so, it has been proposed to implement a thermal heater in the resonator, to be able to control the temperature, and so the phase of light propagating in the resonator. This approach allows us to finely scan the resonance linewidths, providing high performance in terms of the resolution in the measurement.

In this section, I will present the design, fabrication, and characterization of the thermo-optics racetrack resonator in a fully integrated device operated in the LWIR.

4.3.1 Design and Fabrication

The device relies on the same material as reported in the previous section (section 4.2.2.2), which is 6 µm-thick SiGe platforms on top of the Si substrate. The schematic view of the final design is illustrated in Fig.4.17. Each parameter of the racetrack has been adapted from the second run. The bending radius of 250 µm has been chosen. The gap between the bus waveguide and the resonator has been set to 0.8 and 1 µm. The coupling length has been selected as 30, 45, and 60 µm based on the calculation from the coupled mode theory. The design of the metal pad has been inspired by Ref [119]. Metallic squares of 200×200 µm² have been used as pads for putting the DC probe to apply the electrical signal. The heater itself is made of a metal line whose width is 10 µm. The distance between the waveguide center and the metallic ribbon is 8 µm.

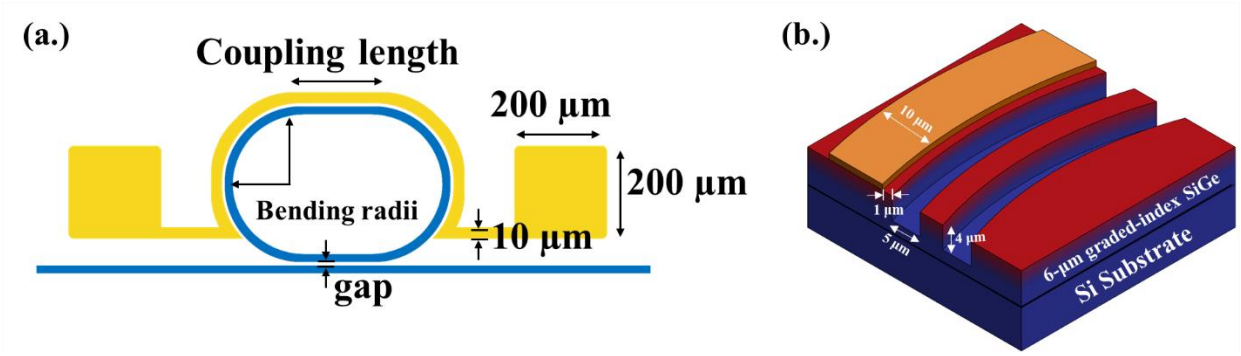

Fig.4.17. (a.) Racetrack resonator design with the implemented heater. Square metallic pads of 200 µm size are used to place the DC probes. (b.) 3D view of the resonator illustrating the placement of the metallic ribbon around the resonator.

The thermo-optic racetrack resonators are fabricated using two lithography steps for metal deposition and patterning the waveguide. The simplified process flow is given in Fig.4.18.

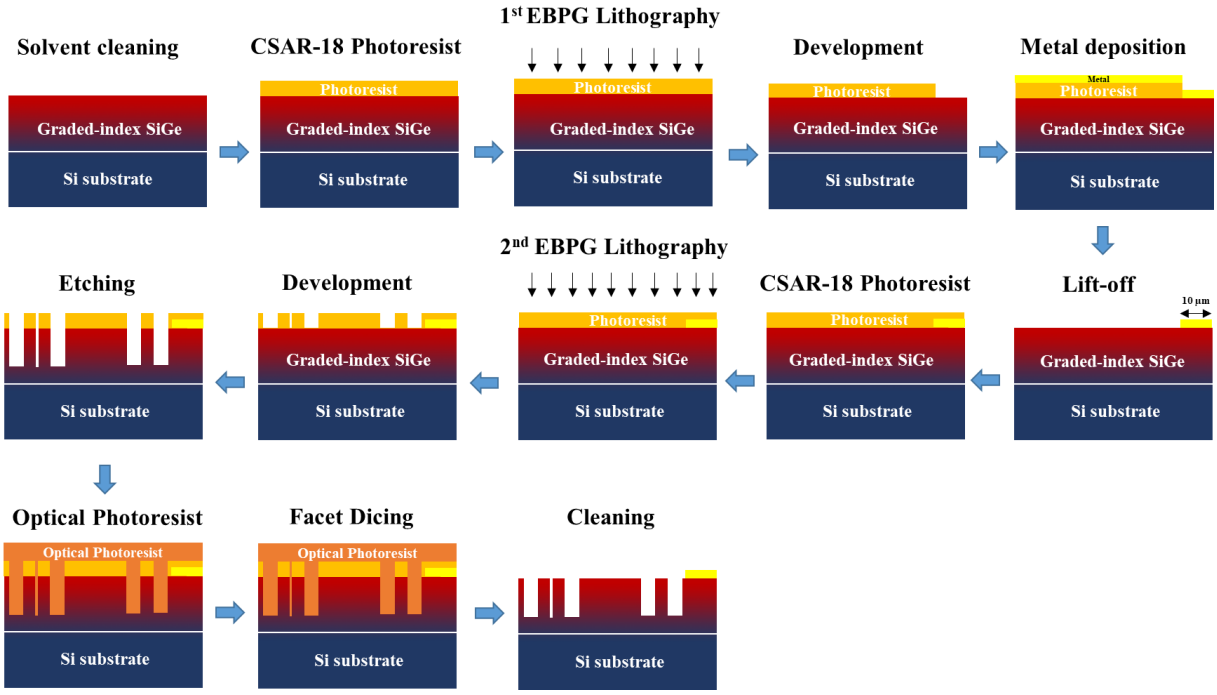

Fig.4.18. Schematic view of the fabrication process of the thermo-optics resonator

The first step consists in cleaning and photoresist deposition, using the same technique as described in the last section (section 4.2.2.2). Then, the patterns of the metal contacts are defined by the 1st step of electron beam lithography (EBPG). After the illumination, the photoresist is developed by using the developer "AR400-546", which resembles the ZED-N50

developer, for 2 mins, followed by isopropanol for 30 sec. So, the part of the photoresist which is exposed to the E-beam will become soluble in the developer. A metallic layer which is composed of 10 nm of titanium (Ti) and 300 nm of goal (Au) is deposited on the surface by E-beam evaporation technique (Plassys Modele MEB 550S) followed by a 2-butanone lift-off process. Au layer is served as a conducting layer for the on-wafer probing, and Ti layer is served to enable a good adhesive between Au and the sample surface. The CSAR.18 photoresist is then deposited on the surface of the sample to be a mask for the second level of lithography. An annealing of 130 °C for 3 min is required after spin coating. The resonators are then patterned by the 2nd level of EBPG, developed, and defined with the RIE-ICP dry etching process. It should be noted that the etching step requires a smooth sidewall roughness and a deep etch in the gap part between the resonator and the bus waveguide. Before going to the next step, the sample is cleaned by using the oxygen-plasma machine for 10 min with a power of 70% and a pressure of 1 mbarr, then put in a 2-butanone solvent. This step is employed to remove all the electronic photoresists remaining from the dry etching. Then, the fabricated structure is protected by using a thick optical photoresist "AZ-4562". To define the waveguide facets, a fine-grained diamond blade is used to perform mechanical dicing inside the access waveguide. This optimized dicing process ensures that the resulting waveguide facets are reproducible and provide similar coupling conditions for the butt-coupling of the free-space laser beam. In the end, the photoresist is removed by acetone and isopropanol. It should be noted that the standard piranha cleaning consisting of sulfuric acid and hydrogen peroxide (H_2SO_4 and H_2O_2) and the HF acid cleaning cannot be employed here as they can destroy the structure of the metal contact. SEM images of the resonator with thermal heater is shown in Fig.4.19.

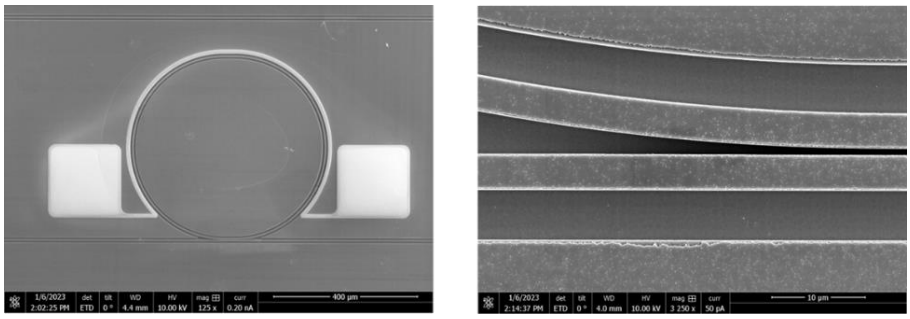

Fig.4.19. SEM images of the racetrack with the implemented metal, with zoom-in view on the directional coupler part.

4.3.2 Experimental Results

The electro-optics resonator measurement has been performed by using the same setup as discussed in section 4.2.1.1. In this measurement, the pulsed QCL is used to characterize the thermal heater efficiency and the phase shift in the resonator as a function of the current applied on the heater, as described later. Then, a CW laser will be used as a narrow linewidth laser for the measurement of the resonance. In order to provide the DC current to the heater, a source-meter unit equipment (Keithley 2400) is used and connected with DC probes. The schematic view of the setup indicated the Keithley source is depicted in Fig.4.20(a). The device under test can be seen in Fig.4.20(b.).

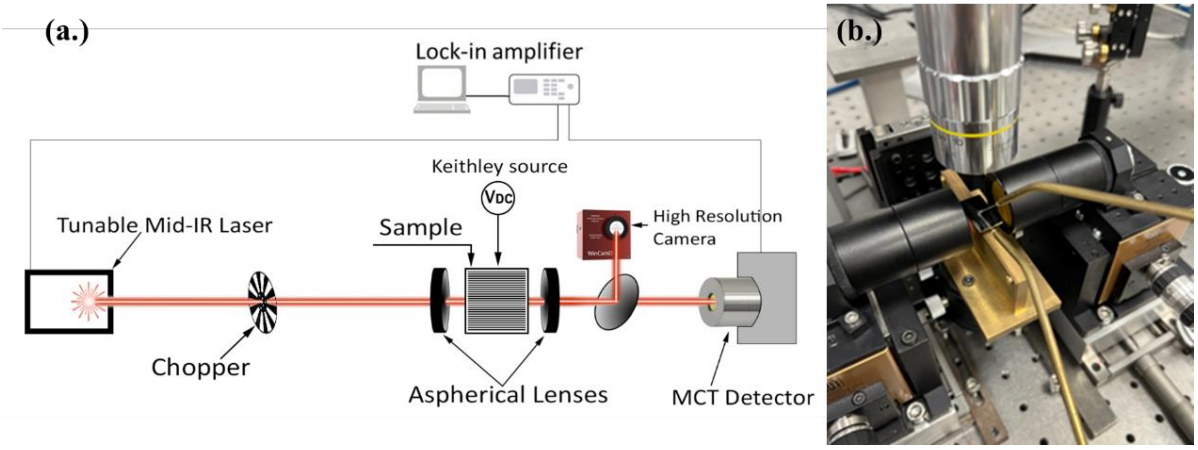

Fig.4.20. (a.) Schematic view of the MIR setup. (b.) Picture of the device under test.

The first experiment was done by using the pulsed QCL. Although we know that the laser linewidth is enlarged by the pulsed operation (equivalent to 6 nm at 8 µm wavelength), useful information can be assessed from the measurement. Indeed, this measurement is first useful to evaluate the broadband operation of the resonator, from 7.8 to 8.8 µm wavelength, as shown in Fig.4.21.

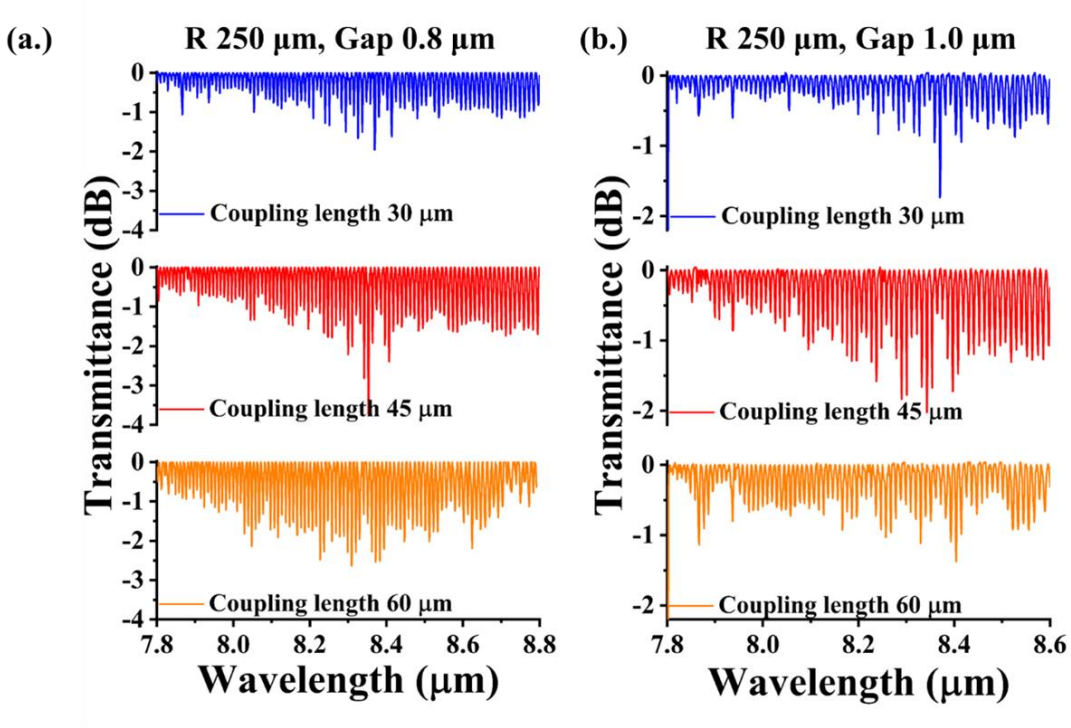

Fig.4.21. Experimental transmission spectra of the racetrack resonators operated around 8 µm wavelength with (a.) gap = 0.8 µm. (b.) gap = 1.0 µm, respectively. The dark blue, red, and orange curves correspond to the different lengths of the directional coupler of 30, 45, and 60 µm, respectively. Broadband operation of the resonator has been observed for all the coupling lengths.

Then, the CW external cavity QCL is employed. As discussed in section 4.2.1.1, the CW laser's linewidth is narrower than the pulsed one (<100 MHz, corresponding to 20 pm at 8 µm wavelength). However, the wavelength sweep is limited by the minimum tuning step size of 0.1 cm^{-1} of the laser, preventing the accuracy of measuring the spectral width of the resonances. In order to overcome all these limitations, a phase variation within the resonator has been implemented to scan the resonance while maintaining a fixed laser wavelength. To do so, a pair of tip probes have been added to the experimental characterization bench, as shown in Fig.4.20(b), to enable an electric contact. The heater efficiency needs first to be evaluated. To do so, the resonator transmitted spectra have been measured as a function of the current injected into the heater, using the pulsed QCL. In this demonstration, I have done all the measurements in the TM-polarization. The optical transmission of the racetrack (R = 250 µm, coupling length = 45 µm) with two different gaps as a function of the wavelength for different dissipated power in the heater can be found in Fig.4.22. The optical transmission of each resonator is collected

for different dissipated powers in the thermal heater, spanning from 0 to 600 mW. The phase shift of the resonator can be deduced by tracking the shift of the resonance wavelength as a function of the power injected into the heater. The electrical power is derived by multiplying the current and voltage measured by using a Keithley 2400 power source. The refractive index of the resonator has been modified thanks to the current injection through the metal path, which will generate heat due to the Joule effect. The characteristic resonance pattern is observed, with an FSR of 10.1 nm in both cases of the gap 0.8 and 1 µm, which corresponds to a group index (n_g) of 3.8 in the resonator. The resonance shifts ($\Delta\lambda$) as a function of the electrical power dissipated in the heater are reported in Fig.4.22(c,d). A resonance shift of 17.5 nm/W can be deduced from the slope of the curve (linear fit in red color). This value will be used to convert the dissipated electrical power to the wavelength shift. The variation of the effective index (Δn_{eff}) due to thermal effect can be calculated using $\Delta n_{eff} = \Delta\lambda \times n_g/\lambda$, where $\Delta\lambda$ is the shift in wavelength of the resonance, n_g is the group index inside the resonator, and λ is the operational wavelength. A value of an effective index variation (Δn_{eff}) of 8.3×10^{-3} for 1 Watt applied on the heater is obtained at the centered wavelength of 8 µm. Furthermore, an average heater efficiency of 20 K/W is obtained when considering the thermo-optic coefficient of Ge as the thermo-optic coefficient of the guided mode ($\partial n/\partial T = 4.1\times10^{-4}\ K^{-1}$). The assumption of the thermo-optic coefficient can be explained by the confinement of the light in the waveguide. In our case of the SiGe-graded platform, light is confined mostly in the waveguide core, indicating around 96% of the power in SiGe waveguide at 8 µm wavelength. The core material is made of SiGe alloy with variations of Ge concentration; based on the literature, for Ge concentration larger than 80% [135], SiGe alloy behaves like pure Ge. Thus, it is possible to consider the thermo-optic coefficient of Ge as the thermo-optic coefficient of the guided mode. Interestingly, this heater efficiency is much larger than the one reported in Ref [119] thanks to the improvement of the heater design. Notably, the distance between the optical mode center and the metallic ribbon has been reduced from 12 µm to 8 µm.

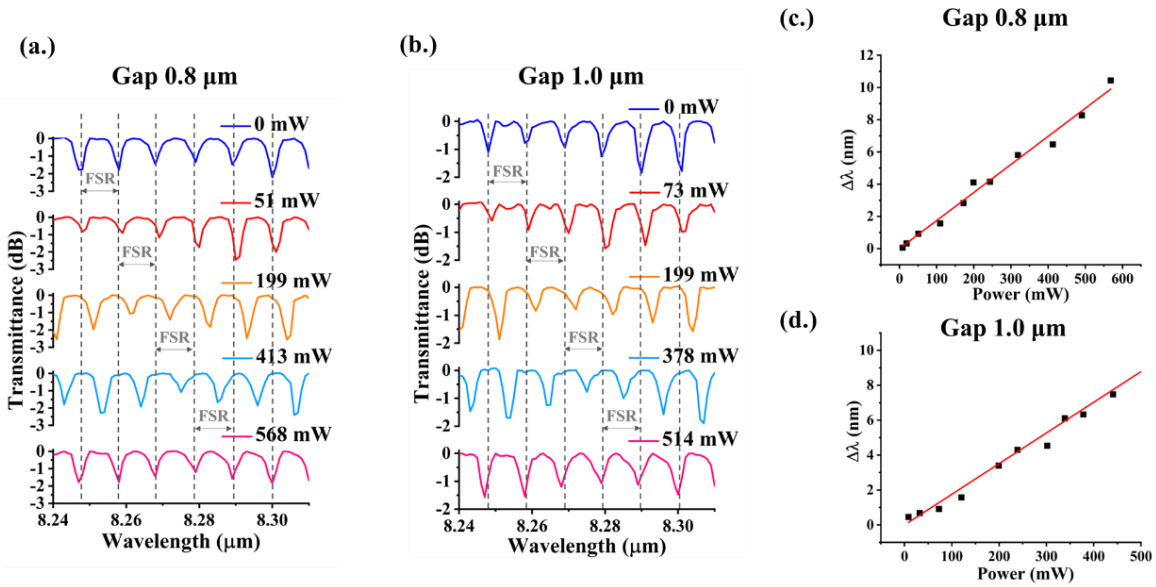

Fig.4.22. Optical transmission spectra as a function of the wavelength (centered wavelength λ = 8 µm) when different values of the current are applied on the heater, (the corresponding dissipated power in the heater is reported). The measurements are done on racetracks with a radius of 250 µm, a coupling length of 45 µm and for different gaps of (a.) 0.8 µm, and (b.) 1.0 µm; the gray lines specify the FSR of the device. Resonance shifts as a function of the power dissipated are reported in (c.) and (d.) for gaps of 0.8 µm and 1.0 µm respectively. The solid red line reports the linear fitting, which is used to estimate the thermal heater performance.

Following that, all devices have been characterized by using the high-resolution measurement using the CW laser at a fixed wavelength, and phase variation in the resonator by current injection to a heater, and the previously mentioned method to convert the dissipated electrical power to the wavelength shift. Examples of resulting measurements are reported in Fig.4.23. Thanks to the fine resolution allowed from the current injection, both Fabry-Perot fringes coming from the facet of the sample and resonances of the resonator can be seen. The resonances observed in the transmission spectra can be fitted using a Lorentzian function, Eq.9, from which the full width at half maximum (FWHM) can be determined. The FWHM increases proportionally with the wavelength. This tendency is applied in the same device with different gaps as well. Hence, we believe that the main concern of the increasing of FWHM at the longer wavelength is related to the propagation losses of the material. To confirm this hypothesis, Eq. 14 and 15 have been applied to extract the intrinsic Q-factor and propagation loss at different wavelengths. The example of the extracted loss of the racetrack with the radius of 250 µm,

coupling length of 30 µm and the gap of 1.0 µm is shown in Fig.4.23(c). The increasing of the propagation loss at the longer wavelength has been observed.

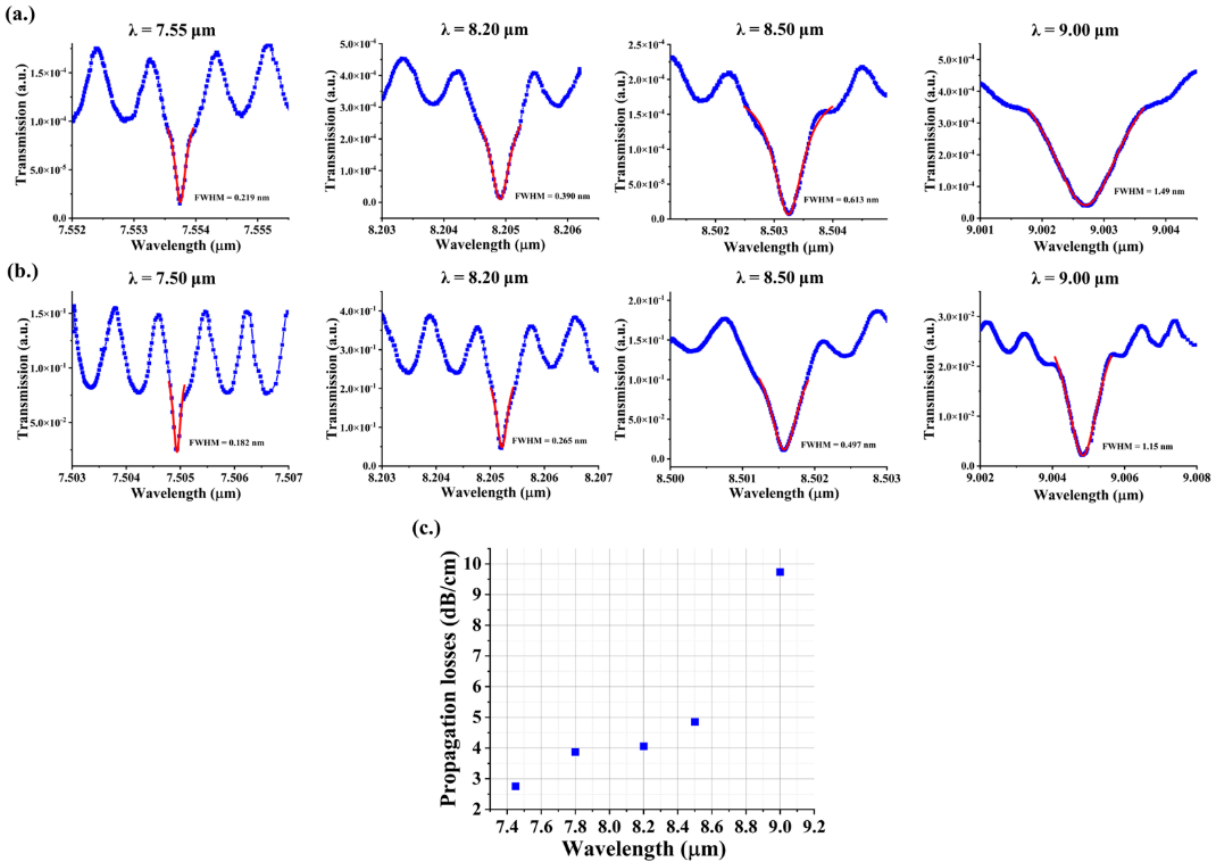

Fig.4.23. Transmission of a resonator (radius 250 µm, coupling length 30 µm) using the thermo-optic measurement to achieve high resolution measurement. Measurement has been reported for two values of the gap between the straight waveguide and the ring, (a.) gap = 0.8 µm and (b.) gap = 1.0 µm. The red line corresponds to a Lorentzian fitting curve. (c.) The calculated propagation loss deduced from Eq.15 for racetrack radius = 250 µm, coupling length = 30 µm, and gap = 1 µm.

For the purpose of confirming the correct calibration procedure, the same racetracks have also been characterized by using the DFB setup. Interestingly, it is confirmed that in the wavelength range accessible with the DFB laser, the two possible approaches to measure the resonance (tuning the wavelength or tuning the phase in the resonator) gives us almost a similar value for the FWHM with a difference of less than 10%. The comparison of different approaches is reported in Fig.4.24.

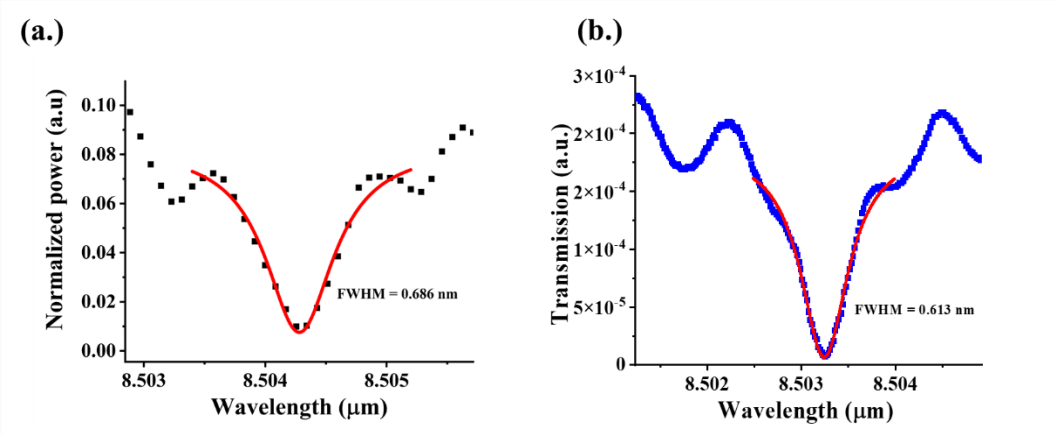

Fig.4.24. Confirmation of the calibration procedure. Transmission of a resonator with a radius of 250 μm and coupling length of 30 μm when measured (a) using the DFB-QCL laser; (b) using the CW laser and thermal variation inside the resonator.

Then, the values of the FWHM and the corresponding Q-factor of the racetrack resonator with a bending radius of 250 μm and gap 1.0 μm are reported as a function of the wavelength for different coupling lengths in Fig.4.25(a-f). The smallest FWHM of 0.172 nm is extracted from the coupling length of 30 μm at 7.45 μm wavelength, which is the smallest coupling length of this device. The loaded Q-factor of 4.3×10^4 has been obtained. By using Eq.4.14, the intrinsic Q-factor of 5.6×10^4 has been extracted, corresponding to the total propagation losses of 2.5 dB/cm. This loss is higher than the one reported in the propagation losses of this platform, which is typically around 1 dB/cm. It can be believed that the difference comes from bend losses and losses at the interface between the bend and straight waveguide.

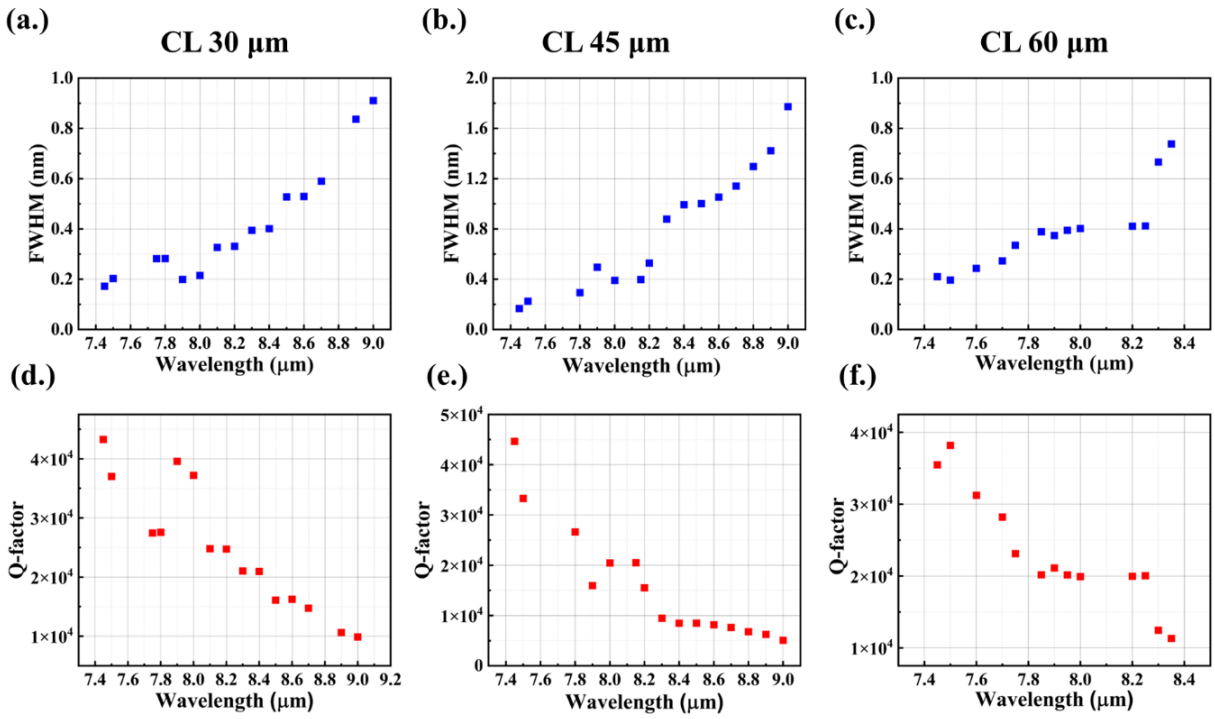

Fig.4.25. Resonance FWHM as a function of the wavelength for a resonator with the same radius of 250 µm with different coupling lengths (the gap is fixed at 1 µm): (a.) CL = 30 µm, (b.) CL = 45 µm, and (c.) CL = 60 µm, respectively. The Q-factor of the resonator, which is calculated from its FWHM: (d.) CL = 30 µm, (e.) CL = 45 µm, and (f.) CL = 60 µm, respectively.

Moreover, it can be seen that at 7.45 µm wavelength, the FWHM does not vary with the coupling length, which confirms that the loaded Q-factor is limited by the intrinsic Q-factor, and so by the losses in the resonator. We can also see that the FWHM increases with the wavelength at a rate that seems roughly independent of the coupling coefficient. This suggests that the linewidth increase does not stem from a variation of the coupling coefficient as a function of the wavelength. The FWHM is thus expected to be limited by the losses in the resonator. These losses can come from various sources, including waveguide losses, bending losses, and losses at the interface between the straight waveguide and the bend. Based on the result from the previous measurement, the largest contribution of the losses is then expected from the bending loss and loss at the interface. In order to reduce these two contributions, I have fabricated another run of devices with an increase of the bend radii and a reduction of the coupling length of the device. Racetracks with a radius of 350 µm and with coupling lengths of 10, 20, and 30 µm with a fixed gap of 1 µm have been fabricated using the same technique for two lithography steps. A narrower FWHM is obtained and presented in Fig.4.26(a-c). The smallest FWHM has been obtained from the coupling length of 10 µm, with a FWHM of 0.074 nm at 7.45 µm wavelength, illustrated in Fig.4.26(g)., which

corresponds to a loaded Q-factor of 1.01×10^5. An intrinsic Q-factor of 1.13×10^5 is deduced at 7.45 µm wavelength, corresponding to total propagation losses of 1.2 dB/cm inside the resonator. This value of loss is consistent with previous measurements on graded SiGe photonic waveguide losses, which indicated that bending loss and losses in the transition between the bend and bus waveguides is probably now negligible in comparison with waveguide propagation losses.

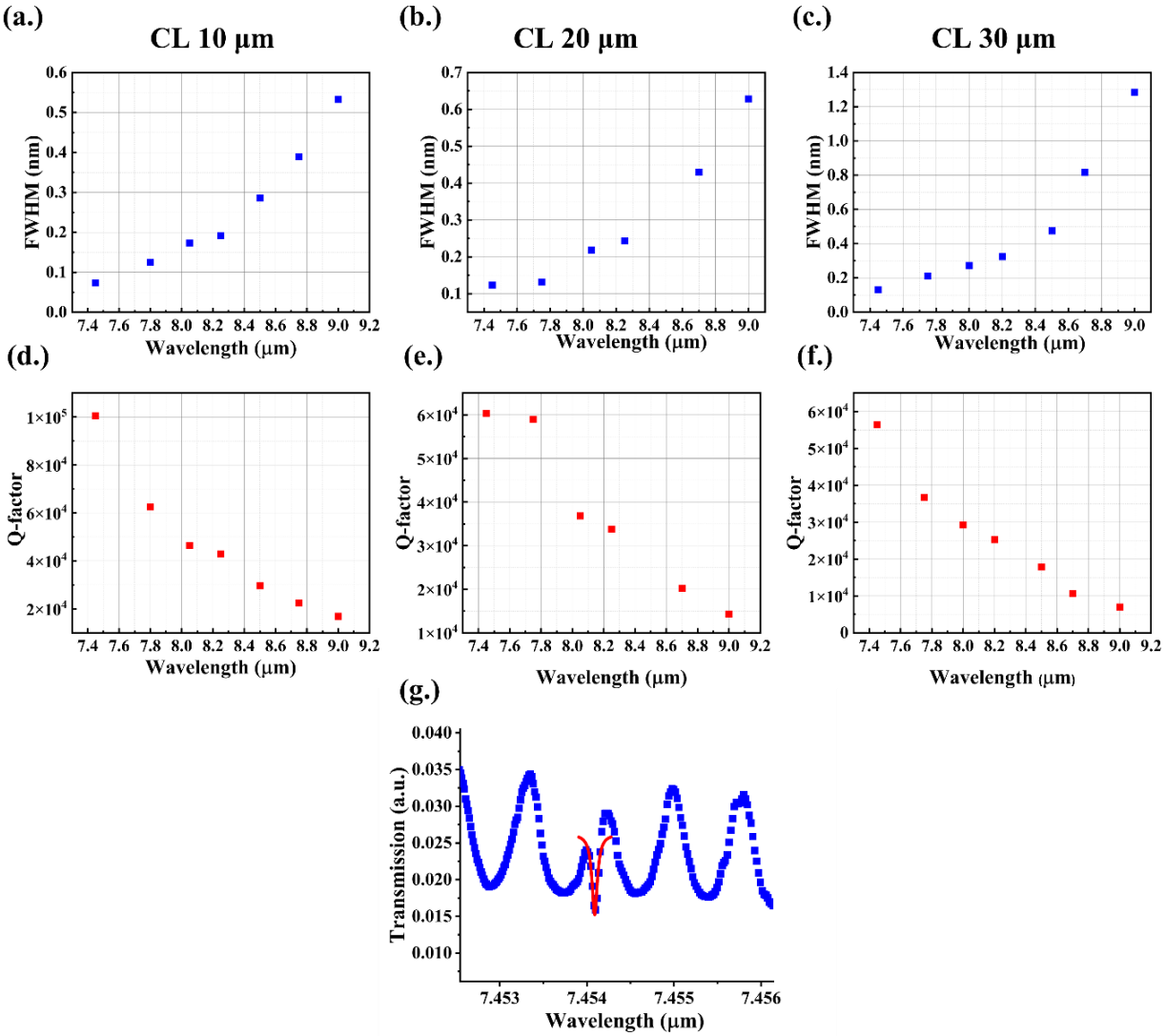

Fig.4.26. Resonance FWHM as a function of the wavelength for a resonator with a radius of 350 µm and with different coupling lengths (the gap is fixed at 1 µm): (a.) CL = 10 µm, (b.) CL = 20 µm, and (c.) CL = 30 µm, respectively. The Q-factor of the resonator, which is calculated from its FWHM for (d.) CL = 10 µm, (e.) CL = 20 µm, and (f.) CL = 30 µm, respectively. (g.) Example of resonator transmission of the racetrack with a radius of 350 µm, coupling length of 10 µm, and the fixed gap of 1 µm as a function of the wavelength at λ = 7.45 µm, showing the highest Q-factor of 1.01×10^5.

4.4 CONCLUSION

In this chapter, integrated resonators have been demonstrated in the LWIR. Wideband operation in the 7.45 – 9 µm wavelength range has been observed in all devices, that have been fabricated in the SiGe graded-index platform. Firstly, racetrack resonators inspired by the work of Joan *et al.* [58] have been fabricated and characterized. In the first two runs, the limitations of the initial experimental setup in terms of spectral resolution have been confirmed. A DFB-QCL setup was then utilized to measure the resonator performances with a high resolution, at the center wavelength of 8.5 µm. However, it should be noted that the DFB setup is not suitable for wideband operation. Therefore, a new approach has been investigated, consisting in implementing a thermal heater in the resonator. By adopting this approach, the previous limitations can be resolved. The implemented heater provides a significant advantage, allowing access to a fine resolution in the scanning measurement. Using these devices, broadband operation in the LWIR has still been observed, while the highest Q-factor of 1.01×10^5 has been found at 7.45 µm wavelength, using a racetrack with a radius of 350 µm, a coupling length of 10 µm, and a fixed gap of 1 µm. This result has experimentally demonstrated a great enhancement of the fully integrated racetrack resonator in the LWIR. The successful demonstration of such an integrated resonator marks a significant step towards implementing microresonator-based comb generators that operate in the LWIR spectral range. Furthermore, these results pave the way for the development of advanced photonics circuits, enabling diverse applications such as sensing, spectroscopy, and communications.

5 CONCLUSIONS AND PERSPECTIVES

5.1 GENERAL CONCLUSIONS

The work presented in this manuscript targeted the development of integrated photonics circuits to enable on-chip sensing applications in the mid-infrared region. To that end, I have studied the development of a monolithically integrated QCL source on top of a SiGe platform within the scope of a French national project, ANR Light UP (ANR-19 CE24-0002-01), the butt-coupling between two separate chips, along with the development of the racetrack resonator as a fundamental building block for PIC.

Regarding monolithic integration, I have demonstrated the development of various fabrication processes to create integrated waveguides based on InAs/AlSb-based Quantum Cascade Lasers (QCLs) on SiGe photonics platform. This work has been taken under the framework of the ANR Light Up in collaboration with L-NESS and IES, who took care of the growth material process. The design of the final device was done before I started my Ph.D. In this sense, I have been in charge of the fabrication process in the cleanroom facility. In order to couple the light from the QCL-based III-V material to the SiGe waveguide, contra-directional grating-assisted coupling has been proposed as a suitable solution to achieve phase matching. Therefore, the device has been designed with two optical mirrors made by corrugation to support the coupling. In this regard, two main challenge aspects have been studied for the monolithic integration: i.) the electrical contacts, and ii.) the etching of the Bragg structures.

To this end, in the first part of my thesis, the optical properties of the SiGe graded index on the n-doped Si substrate have thus been evaluated in a broadband MIR wavelength range from 5.1 to 11.2 µm. A broadband low-loss performance until around 8 µm wavelength has been obtained for both TE and TM polarization. An increase in losses at wavelengths beyond 8.5 µm has been attributed to free-carrier absorption due to the highly doped substrate, Si multiphonon absorption, and oxygen impurities during the growth process. Then, I have demonstrated the possibility to obtain electrical contact through the bottom substrate. I have reported the resistance of 3 Ω from the complete structure of graded SiGe on top of the N+ doped Si substrate, leading to the resistivity between bottom contact and Schottky barrier from 0.4 Ω·cm. These results confirm a small access resistance for future integration of QCL on top of SiGe grown on a doped-Si substrate. Interestingly, the contact on top of SiGe waveguide

has shown a Schottky behavior. This experiment thus paved the way for the integrated EOM based on a Schottky diode embedded in a graded-SiGe waveguide, which has been developed later by M. Montesinos and T. H. N. Nguyen from our group.

In terms of etching the Bragg structure, I have developed the fabrication process for an optical cavity, mainly focused on dry etching of the QCL-based III-V material. The target is to achieve deep etching of more than 10 µm. The primary challenge now is the plane revelation in one direction occurring during the etching process. However, the process of growing QCL on the SiGe faces a lot of difficulties related to the different material properties during the growth process. Therefore, the development of this process has been put on hold for that moment.

Subsequently, I have explored alternative approaches to coupling SiGe chip with QCL source in a compact way. I have then demonstrated a new setup for a butt-coupling study between two separate chips, which has been built up in the C2N facility. The QCL chips have been provided by our collaboration from IES (University of Montpelier). The initial test has been done to provide the proper functioning of the setup. I have performed a direct coupling from the QCL source to one of our SiGe waveguides with the coupling loss extracted from the measurement to be around 10 dB. Furthermore, I conducted numerical simulations to estimate the coupling loss. Interestingly, the results from both simulation and measurement are in good agreement.

Finally, I have designed and demonstrated high Q-factor racetrack resonators operating in the LWIR. As a first step, I have investigated the different experimental configurations, highlighting their limitations in terms of resolution and spectral wavelength tuning. A new design for the racetrack resonator with an implemented heater has been proposed in order to access tuning of the resonance with a thermo-optic effect. This approach offers the possibility of breaking the classical tradeoff of the standard mid-IR experimental setup. In this sense, I have fabricated and experimentally characterized the new racetrack with a heater. A loaded Q-factor of 1.01×10^5 at 7.45 µm wavelength has been reported, using a racetrack with a radius of 300 µm and a coupling length of 10 µm. This result opens a promising route for the entirely integrated racetrack resonator in the LWIR.

5.2 PERSPECTIVES AND FUTURE WORKS

This Ph.D. thesis has opened different routes for developing an on-chip integrated photonics circuit in the mid-IR. I will discuss some of them in the following.

First, the monolithic integration based on InAs/AlSb-based QCL direct growth on SiGe photonics platform has been experimentally investigated. This work has been ongoing within the framework of the ANR Light UP project. Intensive work is currently being done by the partners, to solve the challenges related to the growth of III-V on SiGe template. When this step will be solved, the development of laser monolithically integrated on SiGe platform will open a major breakthrough towards fully on-chip mid-IR sensors based on Si photonics.

Second, the first measurement of butt-coupling between a QCL chip operating at 7.4 µm wavelength and a SiGe photonics circuit has been successfully demonstrated. Still, an enhancement in the setup is yet to be developed. Moreover, it is highly interesting to take advantage of this setup in order to access the integration of the active and passive devices in a compact way.

Regarding the racetrack resonator with an implemented heater, this first experimental demonstration paves the way for multiple possibilities for a fully integrated resonator. One application of the resonator is the ability to create a frequency comb generation. Therefore, it will be interesting to evaluate the nonlinear optical properties of the resonator in order to explore the possibility of a comb generator-based microresonator. Furthermore, this device is expected to be used later in the butt-coupling scheme between the QCL laser and a SiGe resonator to manufacture a compact comb source. In addition, a deeper understanding of the links between the geometrical parameters of the racetrack resonator and the Q-factor should be developed to improve the performance. More research should be carried out to study the influence of each parameter, i.e., increasing the radius, reducing the coupling length, and modifying the gap distance on the resonator performance.

6 REFERENCES

[1] J. Byrnes, Unexploded Ordnance Detection and Mitigation, 2009.

[2] M. Akhloufi, A. Bendada, Fusion of active and passive infrared images for face recognition, 2013.

[3] D. Popa, F. Udrea, Towards Integrated Mid-Infrared Gas Sensors, Sensors 19 (2019) 2076.

[4] P.F. Bernath, Spectra of Atoms and Molecules, Oxford University Press2016.

[5] L. Tombez, E.J. Zhang, J.S. Orcutt, S. Kamlapurkar, W.M.J. Green, Methane absorption spectroscopy on a silicon photonic chip, Optica 4 (2017) 1322-1325.

[6] J.F. Dean, J.J. Middelburg, T. Röckmann, R. Aerts, L.G. Blauw, M. Egger, M.S.M. Jetten, A.E.E. de Jong, O.H. Meisel, O. Rasigraf, C.P. Slomp, M.H. in't Zandt, A.J. Dolman, Methane Feedbacks to the Global Climate System in a Warmer World, 56 (2018) 207-250.

[7] A. Schieweck, E. Uhde, T. Salthammer, L.C. Salthammer, L. Morawska, M. Mazaheri, P. Kumar, Smart homes and the control of indoor air quality, Renewable and Sustainable Energy Reviews 94 (2018) 705-718.

[8] V. Mittal, G. Devitt, M. Nedeljkovic, L.G. Carpenter, H.M.H. Chong, J.S. Wilkinson, S. Mahajan, G.Z. Mashanovich, Ge on Si waveguide mid-infrared absorption spectroscopy of proteins and their aggregates, Biomed. Opt. Express 11 (2020) 4714-4722.

[9] U. Willer, M. Saraji, A. Khorsandi, P. Geiser, W. Schade, Near- and mid-infrared laser monitoring of industrial processes, environment and security applications, Optics and Lasers in Engineering 44 (2006) 699-710.

[10] N.L. Kazanskiy, S.N. Khonina, M.A. Butt, Advancement in Silicon Integrated Photonics Technologies for Sensing Applications in Near-Infrared and Mid-Infrared Region: A Review, Photonics 9 (2022) 331.

[11] R. Kormann, R. Königstedt, U. Parchatka, J. Lelieveld, H. Fischer, QUALITAS: A mid-infrared spectrometer for sensitive trace gas measurements based on quantum cascade lasers in CW operation, Review of Scientific Instruments 76 (2005).

[12] I. Argyriou, M. Wells, A. Glasse, D. Lee, P. Royer, B. Vandenbussche, E. Malumuth, A. Glauser, P.J. Kavanagh, A. Labiano, F. Lahuis, M. Mueller, P. Patapis, The nature of point source fringes in mid-infrared spectra acquired with the James Webb Space Telescope⋆, A&A 641 (2020) A150.

[13] I.E. Gordon, L.S. Rothman, C. Hill, R.V. Kochanov, Y. Tan, P.F. Bernath, M. Birk, V. Boudon, A. Campargue, K.V. Chance, B.J. Drouin, J.M. Flaud, R.R. Gamache, J.T. Hodges, D. Jacquemart, V.I. Perevalov, A. Perrin, K.P. Shine, M.A.H. Smith, J. Tennyson, G.C. Toon, H. Tran, V.G. Tyuterev, A. Barbe, A.G. Császár, V.M. Devi, T. Furtenbacher, J.J. Harrison, J.M. Hartmann, A. Jolly, T.J. Johnson, T. Karman, I. Kleiner, A.A. Kyuberis, J. Loos, O.M. Lyulin, S.T. Massie, S.N. Mikhailenko, N. Moazzen-Ahmadi, H.S.P. Müller, O.V. Naumenko, A.V. Nikitin, O.L. Polyansky, M. Rey, M. Rotger, S.W. Sharpe, K. Sung, E. Starikova, S.A. Tashkun, J.V. Auwera, G. Wagner, J. Wilzewski, P. Wcisło, S. Yu, E.J. Zak, The

HITRAN2016 molecular spectroscopic database, Journal of Quantitative Spectroscopy and Radiative Transfer 203 (2017) 3-69.

[14] Tematys, Mid-ir photodetectors and systems: applicatinos and markets, Tech. Rep, Paris, France, 2019.

[15] M. Sieger, B. Mizaikoff, Toward On-Chip Mid-Infrared Sensors, Analytical Chemistry 88 (2016) 5562-5573.

[16] H. Lin, Z. Luo, T. Gu, L.C. Kimerling, K. Wada, A. Agarwal, J. Hu, Mid-infrared integrated photonics on silicon: a perspective, Nanophotonics 7 (2018) 393-420.

[17] W.J. Westerveld, H.P. Urbach, Silicon Photonics, IOP Publishing2017.

[18] R. Soref, Mid-infrared photonics in silicon and germanium, Nature Photonics 4 (2010) 495-497.

[19] R. Kitamura, L. Pilon, M. Jonasz, Optical constants of silica glass from extreme ultraviolet to far infrared at near room temperature, Applied Optics 46 (2007) 8118-8133.

[20] S.A. Miller, M. Yu, X. Ji, A.G. Griffith, J. Cardenas, A.L. Gaeta, M. Lipson, Low-loss silicon platform for broadband mid-infrared photonics, Optica 4 (2017) 707-712.

[21] J.S. Penadés, A. Sánchez-Postigo, M. Nedeljkovic, A. Ortega-Moñux, J.G. Wangüemert-Pérez, Y. Xu, R. Halir, Z. Qu, A.Z. Khokhar, A. Osman, W. Cao, C.G. Littlejohns, P. Cheben, I. Molina-Fernández, G.Z. Mashanovich, Suspended silicon waveguides for long-wave infrared wavelengths, Opt. Lett. 43 (2018) 795-798.

[22] S. Khan, J. Chiles, J. Ma, S. Fathpour, Silicon-on-nitride waveguides for mid- and near-infrared integrated photonics, Applied Physics Letters 102 (2013) 121104.

[23] C. Ranacher, C. Consani, A. Tortschanoff, R. Jannesari, M. Bergmeister, T. Grille, B. Jakoby, Mid-infrared absorption gas sensing using a silicon strip waveguide, Sensors and Actuators A: Physical 277 (2018) 117-123.

[24] T. Baehr-Jones, A. Spott, R. Ilic, A. Spott, B. Penkov, W. Asher, M. Hochberg, Silicon-on-sapphire integrated waveguides for the mid-infrared, Opt. Express 18 (2010) 12127-12135.

[25] F. Li, S.D. Jackson, C. Grillet, E. Magi, D. Hudson, S.J. Madden, Y. Moghe, C. O'Brien, A. Read, S.G. Duvall, P. Atanackovic, B.J. Eggleton, D.J. Moss, Low propagation loss silicon-on-sapphire waveguides for the mid-infrared, Opt. Express 19 (2011) 15212-15220.

[26] A. Spott, Y. Liu, T. Baehr-Jones, R. Ilic, M. Hochberg, Silicon waveguides and ring resonators at 5.5 μm, Applied Physics Letters 97 (2010) 213501.

[27] R. Shankar, I. Bulu, M. Lončar, Integrated high-quality factor silicon-on-sapphire ring resonators for the mid-infrared, Applied Physics Letters 102 (2013) 051108.

[28] N. Singh, D.D. Hudson, B.J. Eggleton, Silicon-on-sapphire pillar waveguides for Mid-IR supercontinuum generation, Opt. Express 23 (2015) 17345-17354.

[29] H. Lin, L. Li, Y. Zou, S. Danto, J.D. Musgraves, K. Richardson, S. Kozacik, M. Murakowski, D. Prather, P.T. Lin, V. Singh, A. Agarwal, L.C. Kimerling, J. Hu, Demonstration of high-Q mid-infrared chalcogenide glass-on-silicon resonators, Opt. Lett. 38 (2013) 1470-1472.

[30] S. Jung, D. Palaferri, K. Zhang, F. Xie, Y. Okuno, C. Pinzone, K. Lascola, M.A. Belkin, Homogeneous photonic integration of mid-infrared quantum cascade lasers with low-loss passive waveguides on an InP platform, Optica 6 (2019) 1023-1030.

[31] M. Sieger, F. Balluff, X. Wang, S.-S. Kim, L. Leidner, G. Gauglitz, B. Mizaikoff, On-Chip Integrated Mid-Infrared GaAs/AlGaAs Mach–Zehnder Interferometer, Analytical Chemistry 85 (2013) 3050-3052.

[32] N.K. Hon, R. Soref, B. Jalali, The third-order nonlinear optical coefficients of Si, Ge, and Si1−xGex in the midwave and longwave infrared, Journal of Applied Physics 110 (2011) 011301.

[33] Y.-C. Chang, V. Paeder, L. Hvozdara, J.-M. Hartmann, H.P. Herzig, Low-loss germanium strip waveguides on silicon for the mid-infrared, Opt. Lett. 37 (2012) 2883-2885.

[34] M. Nedeljkovic, J.S. Penadés, C.J. Mitchell, A.Z. Khokhar, S. Stanković, T.D. Bucio, C.G. Littlejohns, F.Y. Gardes, G.Z. Mashanovich, Surface-Grating-Coupled Low-Loss Ge-on-Si Rib Waveguides and Multimode Interferometers, IEEE Photonics Technology Letters 27 (2015) 1040-1043.

[35] M. Nedeljkovic, J.S. Penades, V. Mittal, G.S. Murugan, A.Z. Khokhar, C. Littlejohns, L.G. Carpenter, C.B.E. Gawith, J.S. Wilkinson, G.Z. Mashanovich, Germanium-on-silicon waveguides operating at mid-infrared wavelengths up to 8.5 μm, Opt. Express 25 (2017) 27431-27441.

[36] K. Gallacher, R.W. Millar, U. Griškevičiūte, L. Baldassarre, M. Sorel, M. Ortolani, D.J. Paul, Low loss Ge-on-Si waveguides operating in the 8–14 µm atmospheric transmission window, Opt. Express 26 (2018) 25667-25675.

[37] U. Griskeviciute, R.W. Millar, K. Gallacher, J. Valente, D.J. Paul, Ge-on-Si waveguides for sensing in the molecular fingerprint regime, Opt. Express 28 (2020) 5749-5757.

[38] D.A. Kozak, N.F. Tyndall, M.W. Pruessner, W.S. Rabinovich, T.H. Stievater, Germanium-on-silicon waveguides for long-wave integrated photonics: ring resonance and thermo-optics, Opt. Express 29 (2021) 15443-15451.

[39] A. Malik, S. Dwivedi, L. Van Landschoot, M. Muneeb, Y. Shimura, G. Lepage, J. Van Campenhout, W. Vanherle, T. Van Opstal, R. Loo, G. Roelkens, Ge-on-Si and Ge-on-SOI thermo-optic phase shifters for the mid-infrared, Opt. Express 22 (2014) 28479-28488.

[40] S. Radosavljevic, N.T. Beneitez, A. Katumba, M. Muneeb, M. Vanslembrouck, B. Kuyken, G. Roelkens, Mid-infrared Vernier racetrack resonator tunable filter implemented on a germanium on SOI waveguide platform [Invited], Opt. Mater. Express 8 (2018) 824-835.

[41] J. Kang, M. Takenaka, S. Takagi, Novel Ge waveguide platform on Ge-on-insulator wafer for mid-infrared photonic integrated circuits, Opt. Express 24 (2016) 11855-11864.

[42] W. Li, P. Anantha, S. Bao, K.H. Lee, X. Guo, T. Hu, L. Zhang, H. Wang, R. Soref, C.S. Tan, Germanium-on-silicon nitride waveguides for mid-infrared integrated photonics, Applied Physics Letters 109 (2016).

[43] T.-H. Xiao, Z. Zhao, W. Zhou, M. Takenaka, H.K. Tsang, Z. Cheng, K. Goda, Mid-infrared germanium photonic crystal cavity, Opt. Lett. 42 (2017) 2882-2885.

[44] T.-H. Xiao, Z. Zhao, W. Zhou, M. Takenaka, H.K. Tsang, Z. Cheng, K. Goda, High-Q germanium optical nanocavity, Photon. Res. 6 (2018) 925-928.

[45] T.-H. Xiao, Z. Zhao, W. Zhou, C.-Y. Chang, S.Y. Set, M. Takenaka, H.K. Tsang, Z. Cheng, K. Goda, Mid-infrared high-Q germanium microring resonator, Opt. Lett. 43 (2018) 2885-2888.

[46] A. Osman, M. Nedeljkovic, J. Soler Penades, Y. Wu, Z. Qu, A.Z. Khokhar, K. Debnath, G.Z. Mashanovich, Suspended low-loss germanium waveguides for the longwave infrared, Opt. Lett. 43 (2018) 5997-6000.

[47] A. Sánchez-Postigo, A. Ortega-Moñux, J. Soler Penadés, A. Osman, M. Nedeljkovic, Z. Qu, Y. Wu, Í. Molina-Fernández, P. Cheben, G.Z. Mashanovich, J.G. Wangüemert-Pérez, Suspended germanium waveguides with subwavelength-grating metamaterial cladding for the mid-infrared band, Opt. Express 29 (2021) 16867-16878.

[48] C. Grillet, P. Ma, B. Luther-Davies, D. Hudson, C. Monat, S. Madden, D.J. Moss, M. Brun, P. Labeye, S. Ortiz, S. Nicoletti, Low loss SiGe waveguides in the MID-IR, 2013 Conference on Lasers and Electro-Optics - International Quantum Electronics Conference, Optica Publishing Group, Munich, 2013, pp. CK_2_6.

[49] L. Carletti, P. Ma, Y. Yu, B. Luther-Davies, D. Hudson, C. Monat, R. Orobtchouk, S. Madden, D.J. Moss, M. Brun, S. Ortiz, P. Labeye, S. Nicoletti, C. Grillet, Nonlinear optical response of low loss silicon germanium waveguides in the mid-infrared, Opt. Express 23 (2015) 8261-8271.

[50] M. Brun, P. Labeye, G. Grand, J.-M. Hartmann, F. Boulila, M. Carras, S. Nicoletti, Low loss SiGe graded index waveguides for mid-IR applications, Opt. Express 22 (2014) 508-518.

[51] P. Barritault, M. Brun, P. Labeye, J.-M. Hartmann, F. Boulila, M. Carras, S. Nicoletti, Design, fabrication and characterization of an AWG at 4.5 μm, Opt. Express 23 (2015) 26168-26181.

[52] A. Koshkinbayeva, P. Barritault, S. Ortiz, S. Boutami, M. Brun, J.M. Hartmann, P. Brianceau, O. Lartigue, F. Boulila, R. Orobtchouk, P. Labeye, Impact of Non-Central Input in $N \times M$ Mid-IR Arrayed Waveguide Gratings Integrated on Si, IEEE Photonics Technology Letters 28 (2016) 2191-2194.

[53] R. Armand, M. Perestjuk, A. Della Torre, M. Sinobad, A. Mitchell, A. Boes, J.-M. Hartmann, J.-M. Fedeli, V. Reboud, P. Brianceau, A. De Rossi, S. Combrié, C. Monat, C. Grillet, Mid-infrared integrated silicon–germanium ring resonator with high Q-factor, APL Photonics 8 (2023).

[54] J.M. Ramirez, V. Vakarin, C. Gilles, J. Frigerio, A. Ballabio, P. Chaisakul, X.L. Roux, C. Alonso-Ramos, G. Maisons, L. Vivien, M. Carras, G. Isella, D. Marris-Morini, Low-loss Ge-rich Si0.2Ge0.8 waveguides for mid-infrared photonics, Opt. Lett. 42 (2017) 105-108.

[55] J.M. Ramirez, Q. Liu, V. Vakarin, J. Frigerio, A. Ballabio, X. Le Roux, D. Bouville, L. Vivien, G. Isella, D. Marris-Morini, Graded SiGe waveguides with broadband low-loss propagation in the mid infrared, Opt. Express 26 (2018) 870-877.

[56] V. Vakarin, J.M. Ramírez, J. Frigerio, A. Ballabio, X. Le Roux, Q. Liu, D. Bouville, L.

Vivien, G. Isella, D. Marris-Morini, Ultra-wideband Ge-rich silicon germanium integrated Mach–Zehnder interferometer for mid-infrared spectroscopy, Opt. Lett. 42 (2017) 3482-3485.

[57] Q. Liu, J.M. Ramirez, V. Vakarin, X. Le Roux, J. Frigerio, A. Ballabio, E.T. Simola, C. Alonso-Ramos, D. Benedikovic, D. Bouville, L. Vivien, G. Isella, D. Marris-Morini, On-chip Bragg grating waveguides and Fabry-Perot resonators for long-wave infrared operation up to 8.4 µm, Opt. Express 26 (2018) 34366-34372.

[58] J.M. Ramirez, Q. Liu, V. Vakarin, X. Le Roux, J. Frigerio, A. Ballabio, C. Alonso-Ramos, E.T. Simola, L. Vivien, G. Isella, D. Marris-Morini, Broadband integrated racetrack ring resonators for long-wave infrared photonics, Opt. Lett. 44 (2019) 407-410.

[59] Q. Liu, J.M. Ramirez, V. Vakarin, X. Le Roux, C. Alonso-Ramos, J. Frigerio, A. Ballabio, E. Talamas Simola, D. Bouville, L. Vivien, G. Isella, D. Marris-Morini, Integrated broadband dual-polarization Ge-rich SiGe mid-infrared Fourier-transform spectrometer, Opt. Lett. 43 (2018) 5021-5024.

[60] V. Vakarin, W.N. Ye, J.M. Ramírez, Q. Liu, J. Frigerio, A. Ballabio, G. Isella, L. Vivien, C. Alonso-Ramos, P. Cheben, D. Marris-Morini, Ultra-wideband Ge-rich silicon germanium mid-infrared polarization rotator with mode hybridization flattening, Opt. Express 27 (2019) 9838-9847.

[61] M. Montesinos-Ballester, C. Lafforgue, J. Frigerio, A. Ballabio, V. Vakarin, Q. Liu, J.M. Ramirez, X. Le Roux, D. Bouville, A. Barzaghi, C. Alonso-Ramos, L. Vivien, G. Isella, D. Marris-Morini, On-Chip Mid-Infrared Supercontinuum Generation from 3 to 13 μm Wavelength, ACS Photonics 7 (2020) 3423-3429.

[62] M. Montesinos-Ballester, L. Deniel, N. Koompai, T.H.N. Nguyen, J. Frigerio, A. Ballabio, V. Falcone, X. Le Roux, C. Alonso-Ramos, L. Vivien, A. Bousseksou, G. Isella, D. Marris-Morini, Mid-infrared Integrated Electro-optic Modulator Operating up to 225 MHz between 6.4 and 10.7 μm Wavelength, ACS Photonics 9 (2022) 249-255.

[63] Y. Han, H. Park, J. Bowers, K.M. Lau, Recent advances in light sources on silicon, Adv. Opt. Photon. 14 (2022) 404-454.

[64] M.A. Green, J. Zhao, A. Wang, P.J. Reece, M. Gal, Efficient silicon light-emitting diodes, Nature 412 (2001) 805-808.

[65] S. Wirths, R. Geiger, N. von den Driesch, G. Mussler, T. Stoica, S. Mantl, Z. Ikonic, M. Luysberg, S. Chiussi, J.M. Hartmann, H. Sigg, J. Faist, D. Buca, D. Grützmacher, Lasing in direct-bandgap GeSn alloy grown on Si, Nature Photonics 9 (2015) 88-92.

[66] K.P. Homewood, M.A. Lourenço, The rise of the GeSn laser, Nature Photonics 9 (2015) 78-79.

[67] F.T. Armand Pilon, A. Lyasota, Y.M. Niquet, V. Reboud, V. Calvo, N. Pauc, J. Widiez, C. Bonzon, J.M. Hartmann, A. Chelnokov, J. Faist, H. Sigg, Lasing in strained germanium microbridges, Nature Communications 10 (2019) 2724.

[68] S. Wirths, D. Buca, S. Mantl, Si–Ge–Sn alloys: From growth to applications, Progress in Crystal Growth and Characterization of Materials 62 (2016) 1-39.

[69] A. Elbaz, D. Buca, N. von den Driesch, K. Pantzas, G. Patriarche, N. Zerounian, E. Herth, X. Checoury, S. Sauvage, I. Sagnes, A. Foti, R. Ossikovski, J.-M. Hartmann, F. Boeuf, Z. Ikonic, P. Boucaud, D. Grützmacher, M. El Kurdi, Ultra-low-threshold continuous-wave and pulsed lasing in tensile-strained GeSn alloys, Nature Photonics 14 (2020) 375-382.

[70] InAs - Indium Arsenide.

[71] H. Amano, R. Collazo, C.D. Santi, S. Einfeldt, M. Funato, J. Glaab, S. Hagedorn, A. Hirano, H. Hirayama, R. Ishii, Y. Kashima, Y. Kawakami, R. Kirste, M. Kneissl, R. Martin, F. Mehnke, M. Meneghini, A. Ougazzaden, P.J. Parbrook, S. Rajan, P. Reddy, F. Römer, J. Ruschel, B. Sarkar, F. Scholz, L.J. Schowalter, P. Shields, Z. Sitar, L. Sulmoni, T. Wang, T. Wernicke, M. Weyers, B. Witzigmann, Y.-R. Wu, T. Wunderer, Y. Zhang, The 2020 UV emitter roadmap, Journal of Physics D: Applied Physics 53 (2020) 503001.

[72] J. Faist, F. Capasso, D.L. Sivco, C. Sirtori, A.L. Hutchinson, A.Y. Cho, Quantum Cascade Laser, Science 264 (1994) 553-556.

[73] J. Faist, Quantum Cascade Lasers, Oxford University Press2013.

[74] A.N. Baranov, M. Bahriz, R. Teissier, Room temperature continuous wave operation of InAs-based quantum cascade lasers at 15 µm, Opt. Express 24 (2016) 18799-18806.

[75] O. Cathabard, R. Teissier, J. Devenson, J.C. Moreno, A.N. Baranov, Quantum cascade lasers emitting near 2.6 μm, Applied Physics Letters 96 (2010).

[76] H. Nguyen-Van, A.N. Baranov, Z. Loghmari, L. Cerutti, J.-B. Rodriguez, J. Tournet, G. Narcy, G. Boissier, G. Patriarche, M. Bahriz, E. Tournié, R. Teissier, Quantum cascade lasers grown on silicon, Scientific Reports 8 (2018) 7206.

[77] T.E. Kazior, Beyond CMOS: heterogeneous integration of III-V devices, RF MEMS and other dissimilar materials/devices with Si CMOS to create intelligent microsystems, Philos Trans A Math Phys Eng Sci 372 (2014) 20130105.

[78] O. Moutanabbir, U. Gösele, Heterogeneous Integration of Compound Semiconductors, Annual Review of Materials Research 40 (2010) 469-500.

[79] G. Roelkens, J. Zhang, L. Bogaert, M. Billet, D. Wang, B. Pan, C.J. Kruckel, E. Soltanian, D. Maes, T. Vanackere, T. Vandekerckhove, S. Cuyvers, J.D. Witte, I.L. Lufungula, X. Guo, H. Li, S. Qin, G. Muliuk, S. Uvin, B. Haq, C.O.d. Beeck, J. Goyvaerts, G. Lepage, P. Verheyen, J.V. Campenhout, G. Morthier, B. Kuyken, D.V. Thourhout, R. Baets, Micro-Transfer Printing for Heterogeneous Si Photonic Integrated Circuits, IEEE Journal of Selected Topics in Quantum Electronics 29 (2023) 1-14.

[80] X. Luo, Y. Cao, J. Song, X. Hu, Y. Cheng, C. Li, C. Liu, T.-Y. Liow, M. Yu, H. Wang, Q.J. Wang, P.G.-Q. Lo, High-Throughput Multiple Dies-to-Wafer Bonding Technology and III/V-on-Si Hybrid Lasers for Heterogeneous Integration of Optoelectronic Integrated Circuits, Frontiers in Materials 2 (2015).

[81] B. Szelag, K. Hassan, L. Adelmini, E. Ghegin, P. Rodriguez, F. Nemouchi, P. Brianceau, E. Vermande, A. Schembri, D. Carrara, P. Cavalié, F. Franchin, M.C. Roure, L. Sanchez, C. Jany, S. Olivier, Hybrid III–V/Silicon Technology for Laser Integration on a 200-mm Fully CMOS-Compatible Silicon Photonics Platform, IEEE Journal of Selected Topics in Quantum

Electronics 25 (2019) 1-10.

[82] H. Lu, J.S. Lee, Y. Zhao, C. Scarcella, P. Cardile, A. Daly, M. Ortsiefer, L. Carroll, P. O'Brien, Flip-chip integration of tilted VCSELs onto a silicon photonic integrated circuit, Opt. Express 24 (2016) 16258-16266.

[83] A. Moscoso-Mártir, F. Merget, J. Mueller, J. Hauck, S. Romero-García, B. Shen, F. Lelarge, R. Brenot, A. Garreau, E. Mentovich, A. Sandomirsky, A. Badihi, D.E. Rasmussen, R. Setter, J. Witzens, Hybrid silicon photonics flip-chip laser integration with vertical self-alignment, 2017 Conference on Lasers and Electro-Optics Pacific Rim (CLEO-PR), 2017, pp. 1-4.

[84] E. Menard, K.J. Lee, D.-Y. Khang, R.G. Nuzzo, J.A. Rogers, A printable form of silicon for high performance thin film transistors on plastic substrates, Applied Physics Letters 84 (2004) 5398-5400.

[85] M.A. Meitl, Z.-T. Zhu, V. Kumar, K.J. Lee, X. Feng, Y.Y. Huang, I. Adesida, R.G. Nuzzo, J.A. Rogers, Transfer printing by kinetic control of adhesion to an elastomeric stamp, Nature Materials 5 (2006) 33-38.

[86] Y. Halioua, A. Bazin, P. Monnier, T.J. Karle, I. Sagnes, G. Roelkens, D. Van Thourhout, F. Raineri, R. Raj, III-V photonic crystal wire cavity laser on silicon wafer, J. Opt. Soc. Am. B 27 (2010) 2146-2150.

[87] J.E. Bowers, A.Y. Liu, A comparison of four approaches to photonic integration, 2017 Optical Fiber Communications Conference and Exhibition (OFC), 2017, pp. 1-3.

[88] M. Tang, J.-S. Park, Z. Wang, S. Chen, P. Jurczak, A. Seeds, H. Liu, Integration of III-V lasers on Si for Si photonics, Progress in Quantum Electronics 66 (2019) 1-18.

[89] S. Chen, M. Liao, M. Tang, J. Wu, M. Martin, T. Baron, A. Seeds, H. Liu, Electrically pumped continuous-wave 1.3 µm InAs/GaAs quantum dot lasers monolithically grown on on-axis Si (001) substrates, Opt. Express 25 (2017) 4632-4639.

[90] A.Y. Liu, J. Peters, X. Huang, D. Jung, J. Norman, M.L. Lee, A.C. Gossard, J.E. Bowers, Electrically pumped continuous-wave 1.3 μm quantum-dot lasers epitaxially grown on on-axis (001) GaP/Si, Opt. Lett. 42 (2017) 338-341.

[91] D. Choudhury, 3D integration technologies for emerging microsystems, 2010 IEEE MTT-S International Microwave Symposium, 2010, pp. 1-4.

[92] Y. Yao, A.J. Hoffman, C.F. Gmachl, Mid-infrared quantum cascade lasers, Nature Photonics 6 (2012) 432-439.

[93] G. Lifante, Integrated photonics: fundamentals, John Wiley & Sons2003.

[94] A. Spott, J. Peters, M.L. Davenport, E.J. Stanton, C.D. Merritt, W.W. Bewley, I. Vurgaftman, C.S. Kim, J.R. Meyer, J. Kirch, L.J. Mawst, D. Botez, J.E. Bowers, Quantum cascade laser on silicon, Optica 3 (2016) 545-551.

[95] M. Nedeljkovic, R. Soref, G.Z. Mashanovich, Predictions of Free-Carrier Electroabsorption and Electrorefraction in Germanium, IEEE Photonics Journal 7 (2015) 1-14.

[96] S.M. Sze, J.C. Irvin, Resistivity, mobility and impurity levels in GaAs, Ge, and Si at 300°K, Solid-State Electronics 11 (1968) 599-602.

[97] MIRcat™ Mid-IR Laser.

[98] F.A. Johnson, Lattice Absorption Bands in Silicon, Proceedings of the Physical Society 73 (1959) 265.

[99] M. Nedeljkovic, R. Soref, G.Z. Mashanovich, Free-Carrier Electrorefraction and Electroabsorption Modulation Predictions for Silicon Over the 1–14- $\mu\hbox{m}$ Infrared Wavelength Range, IEEE Photonics Journal 3 (2011) 1171-1180.

[100] M. Montesinos-Ballester, V. Vakarin, Q. Liu, X. Le Roux, J. Frigerio, A. Ballabio, A. Barzaghi, C. Alonso-Ramos, L. Vivien, G. Isella, D. Marris-Morini, Ge-rich graded SiGe waveguides and interferometers from 5 to 11 µm wavelength range, Opt. Express 28 (2020) 12771-12779.

[101] E. Artacho, F. Ynduráin, B. Pajot, R. Ramírez, C.P. Herrero, L.I. Khirunenko, K.M. Itoh, E.E. Haller, Interstitial oxygen in germanium and silicon, Physical Review B 56 (1997) 3820-3833.

[102] M. Lorenc, J. Humlíček, Localized Vibrational Modes of Interstitial Oxygen in Si _x Ge _1-x Alloys, Acta Physica Polonica A 94 (1998) 436-440.

[103] C.-D. Lien, F. So, M.-A. Nicolet, An improved forward IV method for nonideal Schottky diodes with high series resistance, IEEE Transactions on Electron Devices 31 (1984) 1502-1503.

[104] S.M. Sze, Y. Li, K.K. Ng, Physics of semiconductor devices, John wiley & sons2021.

[105] M. Montesinos-Ballester, L. Deniel, N. Koompai, T.H.N. Nguyen, J. Frigerio, A. Ballabio, V. Falcone, X. Le Roux, C. Alonso-Ramos, L. Vivien, Broadband mid-infrared integrated electro-optic modulator based on a Schottky diode embedded in a graded SiGe waveguide, 2021 IEEE 17th International Conference on Group IV Photonics (GFP), IEEE, 2021, pp. 1-2.

[106] M. Montesinos-Ballester, L. Deniel, N. Koompai, T.H.N. Nguyen, J. Frigerio, A. Ballabio, V. Falcone, X. Le Roux, C. Alonso-Ramos, L. Vivien, Mid-infrared Integrated Electro-optic Modulator Operating up to 225 MHz between 6.4 and 10.7 μm Wavelength, ACS photonics 9 (2022) 249-255.

[107] T.H.N. Nguyen, N. Koompai, V. Turpaud, M. Montesinos-Ballester, J. Peltier, J. Frigerio, A. Ballabio, R. Giani, J.-R. Coudevylle, C. Villebasse, 1 GHz electro-optical silicon-germanium modulator in the 5-9 μm wavelength range, Opt. Express 30 (2022) 47093-47102.

[108] T.H.N. Nguyen, N. Koompai, V. Turpaud, J. Peltier, J. Frigerio, S. Calcaterra, A. Ballabio, J.-R. Coudevylle, C. Villebasse, D. Bouville, Integrated electro-optical modulator and photodetector for the mid-infrared spectral range, 2023 Conference on Lasers and Electro-Optics (CLEO), IEEE, 2023, pp. 1-2.

[109] S. Bouchoule, G. Patriarche, S. Guilet, L. Gatilova, L. Largeau, P. Chabert, Sidewall passivation assisted by a silicon coverplate during Cl2–H2 and HBr inductively coupled plasma etching of InP for photonic devices, Journal of Vacuum Science & Technology B: Microelectronics and Nanometer Structures Processing, Measurement, and Phenomena 26 (2008) 666-674.

[110] J. Grym, Semiconductor technologies, BoD–Books on Demand2010.

[111] C. Alonso-Ramos, M. Nedeljkovic, D. Benedikovic, J.S. Penadés, C.G. Littlejohns, A.Z. Khokhar, D. Pérez-Galacho, L. Vivien, P. Cheben, G.Z. Mashanovich, Germanium-on-silicon mid-infrared grating couplers with low-reflectivity inverse taper excitation, Opt. Lett. 41 (2016) 4324-4327.

[112] S. Radosavljevic, B. Kuyken, G. Roelkens, Efficient 5.2 μm wavelength fiber-to-chip grating couplers for the Ge-on-Si and Ge-on-SOI mid-infrared waveguide platform, Opt. Express 25 (2017) 19034-19042.

[113] J. Kang, Z. Cheng, W. Zhou, T.-H. Xiao, K.-L. Gopalakrisna, M. Takenaka, H.K. Tsang, K. Goda, Focusing subwavelength grating coupler for mid-infrared suspended membrane germanium waveguides, Opt. Lett. 42 (2017) 2094-2097.

[114] D. Hu, Y. Zhang, Y.-Y. Zhao, X.-M. Duan, Efficient 4.95 μm–8.5 μm dual-band grating coupler with crosstalk suppression capability, Opt. Express 30 (2022) 2131-2142.

[115] Q. Liu, J.M. Ramirez, V. Vakarin, D. Benedikovic, C. Alonso-Ramos, J. Frigerio, A. Ballabio, G. Isella, L. Vivien, D. Marris-Morini, 7.5-μm wavelength fiber-chip grating couplers for Ge-rich SiGe photonics integrated circuits, Silicon Photonics: From Fundamental Research to Manufacturing, SPIE, 2018, pp. 31-37.

[116] A. Sánchez-Postigo, A. Ortega-Moñux, D. Pereira-Martín, Í. Molina-Fernández, R. Halir, P. Cheben, J.S. Penadés, M. Nedeljkovic, G. Mashanovich, J. Wangüemert-Pérez, Design of a suspended germanium micro-antenna for efficient fiber-chip coupling in the long-wavelength mid-infrared range, Opt. Express 27 (2019) 22302-22315.

[117] S. Boust, H. El Dirani, L. Youssef, Y. Robert, A. Larrue, C. Petit-Etienne, E. Vinet, S. Kerdiles, E. Pargon, M. Faugeron, Microcomb source based on InP DFB/Si 3 N 4 microring butt-coupling, Journal of Lightwave Technology 38 (2020) 5517-5525.

[118] G. Lihachev, J. Riemensberger, W. Weng, J. Liu, H. Tian, A. Siddharth, V. Snigirev, V. Shadymov, A. Voloshin, R.N. Wang, Low-noise frequency-agile photonic integrated lasers for coherent ranging, Nature communications 13 (2022) 3522.

[119] M. Montesinos-Ballester, Q. Liu, V. Vakarin, J.M. Ramirez, C. Alonso-Ramos, X.L. Roux, J. Frigerio, A. Ballabio, E. Talamas, L. Vivien, On-chip Fourier-transform spectrometer based on spatial heterodyning tuned by thermo-optic effect, Scientific Reports 9 (2019) 14633.

[120] P. Steglich, D.G. Rabus, C. Sada, M. Paul, M.G. Weller, C. Mai, A. Mai, Silicon photonic micro-ring resonators for chemical and biological sensing: A tutorial, IEEE sensors journal 22 (2021) 10089-10105.

[121] G. Antonacci, K. Elsayad, D. Polli, On-chip notch filter on a silicon nitride ring resonator for brillouin spectroscopy, ACS Photonics 9 (2022) 772-777.

[122] A.L. Gaeta, M. Lipson, T.J. Kippenberg, Photonic-chip-based frequency combs, nature photonics 13 (2019) 158-169.

[123] W. Bogaerts, P. De Heyn, T. Van Vaerenbergh, K. De Vos, S. Kumar Selvaraja, T. Claes, P. Dumon, P. Bienstman, D. Van Thourhout, R. Baets, Silicon microring resonators, Laser & Photonics Reviews 6 (2012) 47-73.

[124] R. Shankar, I. Bulu, M. Lončar, Integrated high-quality factor silicon-on-sapphire ring resonators for the mid-infrared, Applied Physics Letters 102 (2013).

[125] M. Perestjuk, R. Armand, A. Della Torre, M. Sinobad, A. Mitchell, A. Boes, J.-M. Hartmann, J.-M. Fedeli, V. Reboud, C. Monat, High-Q silicon-germanium ring resonator for on-chip sensing applications in the mid-infrared, Optics and Photonics for Sensing the Environment, Optica Publishing Group, 2022, pp. EM1D. 4.

[126] D. Ren, C. Dong, S.J. Addamane, D. Burghoff, High-quality microresonators in the longwave infrared based on native germanium, nature communications 13 (2022) 5727.

[127] J. Heebner, R. Grover, T. Ibrahim, Optical microresonator theory, Springer2008.

[128] D.G. Rabus, Integrated ring resonators, (2007).

[129] I. Demirtzioglou, C. Lacava, K.R. Bottrill, D.J. Thomson, G.T. Reed, D.J. Richardson, P. Petropoulos, Frequency comb generation in a silicon ring resonator modulator, Opt. Express 26 (2018) 790-796.

[130] L. Vivien, L. Pavesi, Handbook of silicon photonics, CRC press2013.

[131] K. Zhang, G. Böhm, M.A. Belkin, Mid-infrared microring resonators and optical waveguides on an InP platform, Applied Physics Letters 120 (2022).

[132] Q. Liu, SiGe photonic integrated circuits for mid-infrared sensing applications, Université Paris Saclay (COmUE), 2019.

[133] Quantum Cascade Lasers (QCLs): Distributed Feedback.

[134] Evanescent waveguide couplers.

[135] M. Ferhat, A. Zaoui, B. Khelifa, H. Aourag, Band structure calculations of GexSi1− x, Solid state communications 91 (1994) 407-411.